Superconducting and Dielectric Resonators for the Scaling of Silicon MOS Qubits

Author:
Guo, Kevin

Publication Date:
2025

DOI:
https://doi.org/10.26190/unsworks/31494

Superconducting and Dielectric Resonators for the Scaling of Silicon MOS Qubits

Kevin Shixiao Guo

A thesis in fulfilment of the requirements for the degree of

Doctor of Philosophy

UNSW
SYDNEY

School of Electrical Engineering and Telecommunications

Faculty of Engineering

The University of New South Wales

December 2024

1. Originality, Copyright And Authenticity Statements

Thesis Title and Abstract | Declarations | Inclusion of Publications Statement | Corrected Thesis and Responses

ORIGINALITY STATEMENT

☑ I hereby declare that this submission is my own work and to the best of my knowledge it contains no materials previously published or written by another person, or substantial proportions of material which have been accepted for the award of any other degree or diploma at UNSW or any other educational institution, except where due acknowledgement is made in the thesis. Any contribution made to the research by others, with whom I have worked at UNSW or elsewhere, is explicitly acknowledged in the thesis. I also declare that the intellectual content of this thesis is the product of my own work, except to the extent that assistance from others in the project's design and conception or in style, presentation and linguistic expression is acknowledged.

COPYRIGHT STATEMENT

☑ I hereby grant the University of New South Wales or its agents a non-exclusive licence to archive and to make available (including to members of the public) my thesis or dissertation in whole or part in the University libraries in all forms of media, now or here after known. I acknowledge that I retain all intellectual property rights which subsist in my thesis or dissertation, such as copyright and patent rights, subject to applicable law. I also retain the right to use all or part of my thesis or dissertation in future works (such as articles or books).

For any substantial portions of copyright material used in this thesis, written permission for use has been obtained, or the copyright material is removed from the final public version of the thesis.

AUTHENTICITY STATEMENT

☑ I certify that the Library deposit digital copy is a direct equivalent of the final officially approved version of my thesis.

2. Inclusion of Publications Statement

Thesis Title and Abstract | Declarations | Inclusion of Publications Statement | Corrected Thesis and Responses

UNSW is supportive of candidates publishing their research results during their candidature as detailed in the UNSW Thesis Examination Procedure.

Publications can be used in the candidate's thesis in lieu of a Chapter provided:

- The candidate contributed **greater than 50%** of the content in the publication and are the "primary author", i.e. they were responsible primarily for the planning, execution and preparation of the work for publication.
- The candidate has obtained approval to include the publication in their thesis in lieu of a Chapter from their Supervisor and Postgraduate Coordinator.
- The publication is not subject to any obligations or contractual agreements with a third party that would constrain its inclusion in the thesis.

☑ The candidate has declared that **some of the work described in their thesis has been published and has been documented in the relevant Chapters with acknowledgement**.

A short statement on where this work appears in the thesis and how this work is acknowledged within chapter/s:

> Chapter 3 includes work from the following manuscript which has been submitted for publication: K. S. Guo, M. Feng, J. Y. Huang, W. Gilbert, K. M. Itoh, F. E. Hudson, K. W. Chan, W. H. Lim, A. S. Dzurak, A. Saraiva. Methods for transverse and longitudinal spin-photon coupling in silicon quantum dots with intrinsic spin-orbit effect. Submitted to Phys. Rev. Applied. Preprint available: arXiv:2308.12626 [cond-mat.mes-hall]. Acknowledgement is made at the start of the chapter

Candidate's Declaration

I declare that I have complied with the Thesis Examination Procedure.

Abstract

Silicon MOS (SiMOS) spin qubits are a promising platform for fault tolerant quantum computation due to their long coherence times and compatibility with manufacturing processes ubiquitous in the semiconductor industry. However, a spin-based quantum computer capable of running practical quantum algorithms will likely require an architecture which can be scaled to millions of qubits. This thesis investigates two solutions to open problems in the scalability of SiMOS quantum computers: superconducting resonators for long range qubit coupling and dielectric resonators for global qubit control.

The field of circuit quantum electrodynamics (cQED) examines the light-matter interaction between photons in superconducting resonators and quantum systems such as spins in semiconductors. This has exciting applications for spin qubits, as it potentially enables the transfer of quantum information between distant qubits in a large scale quantum computer. Using a combination of cQED theory and experimental data, transverse and longitudinal spin-photon coupling schemes are evaluated for SiMOS spin qubits. The transverse coupling strength is found to be sufficient for strong spin-photon coupling presuming the integration of a suitable superconducting resonator. This coupling utilizes the intrinsic spin-orbit effect of electron spin qubits in SiMOS, removing the need for an on-chip micromagnet.

Another challenge relating to the scalability of large arrays of qubits is the individual control of many qubits simultaneously. Currently, the prevailing method of qubit control is to address qubits individually, an approach which is not easily scaled to millions of qubits due to qubit crosstalk. A potential solution uses an on-chip dielectric resonator to provide a uniform global field which can be used to drive all qubits on a device simultaneously. Previous studies have shown coherent control of qubits using a dielectric resonator; this thesis expands on these findings by demonstrating two-axis single qubit control of

bare qubits and qubits dressed in continuous wave and sinusoidally modulating global fields. Gate set tomography is used to benchmark the qubits, achieving bare and dressed single gate fidelities over 99%. Noise spectroscopy experiments are performed to measure qubit decoherence and posit possible physical sources of qubit noise. These results demonstrate the viability of dielectric resonators as a method of global control in quantum computers.

Acknowledgements

I would like to express my deepest gratitude to my supervisors, Andrew Dzurak and Wee Han Lim, for their help and mentorship throughout my studies. To Andrew, thank you for leading such an amazing research group and cultivating a culture of open collaboration and academic excellence. Wee Han, my PhD studies would not have been possible without your continued advocacy and guidance. I always felt like I had you in my corner and for that, I am very grateful.

I have been extremely lucky to have worked with many talented individuals over the course of my PhD. To Ensar, who taught me to measure my first qubits, thank you for your training and guidance during my experimental run on the global control project (and your continued positivity in the face of a sometimes uncooperative fridge). Thanks to Arne, Tuomo, Jonathan, Zeheng, Santiago, Paul, Cam, Andi, Nard, and Ingvild, who were always open to share advice (and code) on experiments.

Mengke, thank you for your all-round theory expertise which was instrumental in both the superconducting and dielectric resonator projects. Andre, thank you for your leadership of the theory team and excellent BBQ skills. Thanks also to Amanda, Henry, Gerardo, and everyone else on the theory team who make our lives as experimentalists much easier.

Having experienced first-hand the challenges of fabrication, I am amazed at and grateful for the work that Wee Han, Kok Wai and Fay do to provide us with world-leading qubit devices. Thanks also to all the ANFF staff for maintaining the excellent fabrication facilities at both UNSW and USYD. I'd also like to thank Wyatt, Daniel and Anders from Andrea Morello's group for their help with the design, fabrication and testing of superconducting resonators, as well as Rocky for his help with CPMG experiments.

Finally, and most of all, I would like to thank my parents, Lina and Lanbin, to whom I owe everything for their unconditional love and support. My first contribution to the scientific literature was arguably at the age of three, when my name appeared in the acknowledgements of my parents' theses. Now, over 25 years later, I'm honoured to return the favour.

Publications and Presentations

List of Publications

- **K. S. Guo**, E. Vahapoglu, A. Seedhouse, M. Feng, G. A. Paz-Silva, J. Slack-Smith, W. H. Lim, F. E. Hudson, K. Itoh, T. Tanttu, A. Laucht, C. H. Yang, A. Saraiva, J. J. Pla, A. S. Dzurak. *Tomography of silicon spin qubits dressed in a global field.* Manuscript in preparation.
- **K. S. Guo**, M. Feng, J. Y. Huang, W. Gilbert, K. M. Itoh, F. E. Hudson, K. W. Chan, W. H. Lim, A. S. Dzurak, A. Saraiva. *Methods for transverse and longitudinal spin-photon coupling in silicon quantum dots with intrinsic spin-orbit effect.* Submitted to *Phys. Rev. Applied.* Preprint available: arXiv:2308.12626 [cond-mat.mes-hall]

List of Presentations

Oral presentations:

- *Tomography of silicon spin qubits dressed in a global field.* Silicon Quantum Electronics Workshop 2024, Davos Switzerland.

Poster presentations:

- *Tomography of spin qubits dressed in a global field* LPS Quantum Computing Program Review 2024, Boston, MA, United States.

- *Spin-photon coupling in silicon quantum dots with intrinsic spin-orbit effect.* Silicon Quantum Electronics Workshop 2023, Kyoto, Japan.
- *Spin-photon coupling in silicon quantum dots with intrinsic spin-orbit effect.* Centre for Quantum Computation and Communication Technology Annual Workshop 2022, Hunter Valley, NSW, Australia.

Abbreviations

2DEG	2-Dimensional Electron Gas
AC	Alternating Current
CMOS	Complementary Metal-Oxide-Semiconductor
CNOT	Controlled-NOT
CPMG	Carr-Purcell-Meiboom-Gill Pulse sequence
CPW	Coplanar Waveguide
cQED	Cavity/Circuit Quantum Electrodynamics
CZ	Controlled-Z
DC	Direct Current
EBL	Electron Beam Lithography
EDSR	Electron Dipole Spin Resonance
ESR	Electron Spin Resonance
FM	Frequency Modulation
FOGI	First Order Gauge Invariant
FSK	Frequency Shift Keying
FWHM	Full Width Half Maximum
grAl	Granular Aluminium
GST	Gate Set Tomography

HEMT	High-Electron-Mobility Transistor
MOSFET	Metal-Oxide-Semiconductor Field-Effect Transistor
PESOS	Pulsed Electron Spin-Orbital Spectroscopy
PSB	Pauli Spin Blockade
QND	Quantum Nondemolition
RSA	Rivest–Shamir–Adleman encryption protocol
SEM	Scanning Electron Microscope
SET	Single Electron Transistor
SiMOS	Silicon Metal-Oxide-Semiconductor
SMART	Sinusoidally Modulated, Always Rotating and Tailored
SNR	Signal-to-Noise Ratio
SPAM	State Preparation and Measurement
TE	Transverse Electric
TLS	Two-Level System
UDOX	Ultra Dry Oxide
VNA	Vector Network Analyser
ZPF	Zero-Point Fluctuations

Contents

List of Figures

List of Tables

Chapter 1

Introduction

1.1 Quantum Computing

In 1981, Richard Feynman delivered a talk on the simulation of physical systems with computers [1]. The premise of his speech was simple: to efficiently simulate the quantum laws of nature, one must use a computer which harnesses quantum mechanics. In fact, there exist classes of problems that are impractical to solve for classical computers based on binary logic [2]. Feynman's proposal was the first application for a computer utilising quantum phenomena, initiating the nascent field of quantum computing.

Quantum computing research was catalysed in 1994 by Peter Shor's discovery of a quantum algorithm for the factorisation of prime numbers [3]. Shor's algorithm showed that a fault-tolerant quantum computer was capable of factoring prime numbers in polynomial time; in contrast, the fastest known classical

algorithm scales exponentially with prime number size. The intractability of prime factorisation is a core assumption of the Rivest–Shamir–Adleman (RSA) protocol which forms the backbone of encryption in the digital age [4]. Suddenly, quantum computing had geopolitical and economic consequences, and scientific interest in the field skyrocketed.

1.1.1 Fault tolerance and quantum supremacy

In order to implement a practical quantum algorithm such as Shor's algorithm, quantum computers must be robust to the decoherence mechanisms which affect quantum bits (qubits). Quantum error detection and correction protocols exist which are able to rectify these errors to a certain extent [5]; however, a minimum threshold for qubit fidelity must be met before the protocols correct more errors than they create. Above this threshold, entangling multiple physical qubits encodes a single logical qubit which is capable of fault tolerant quantum computation. In practice, a single error-corrected logical qubit may consist of thousands or millions of physical qubits [6]. The ultimate goal for a quantum computer is to demonstrate quantum supremacy: a computational advantage over classical computers. Experimental claims of quantum advantage have attracted intense attention and scrutiny; the 2019 assertion of quantum supremacy on Google's 53-qubit Sycamore processor [7] was contested by the research community and later found to be inaccurate [8]. In any case, a quantum computer is yet to solve a practical real-world problem faster than the most powerful classical computers, though applications may exist for pre-fault-tolerant quantum computers [9].

30 years after the publication of Shor's algorithm, research is being conducted on a diverse array of promising quantum computing technologies such as superconducting circuits [9–11], ion traps [12,13], neutral atoms [14], photons [15–17], and spins in the solid state [18–22]. This thesis focuses on one such platform: electron spins in silicon metal-oxide-semiconductor (SiMOS) quantum dots.

1.1.2 DiVincenzo's criteria

The DiVincenzo criteria are a widely cited set of conditions that a potential qubit platform must satisfy for fault-tolerant quantum computation [23]. They are:

1. A scalable physical system with well-characterised qubit.
2. The ability to initialise the state of the qubits to a simple fiducial state.
3. Long relevant quantum coherence times.
4. A "universal" set of quantum gates.
5. A qubit-specific measurement capability.

There is yet to be a quantum computing platform capable of fulfilling all of DiVincenzo's criteria. While several promising candidates are capable of demonstrating criteria 2-5 at a small scale, the main bottleneck for many platforms (including semiconductor spin qubits) is the scalability clause of the first criterion.

1.1.3 Silicon MOS quantum computing

Electron spin qubits in the silicon metal-oxide-semiconductor (SiMOS) platform are a leading contender in the race for fault-tolerant quantum computation. Similar to conventional MOS field-effect transistor (MOSFET) designs, quantum dot structures are defined with a metal gate stack which sits on top of an insulating oxide layer. The electrostatic potential of the quantum dot is highly tunable with the metal gates, and single electrons can be confined in the dot with spin states split by an external magnetic field [24]. The fabrication of SiMOS devices is compatible with existing CMOS processes, enabling its manufacture and integration with classical control electronics [25]. In addition, SiMOS qubits can be fabricated with isotopically enriched silicon substrates, which minimises spin decoherence from nuclear spins [26]. This has allowed for demonstrations of initialisation, universal control, and readout of SiMOS qubits with exceptionally high fidelity, fulfilling four of DiVincenzo's criteria [18]. The final criterion, scalability, remains an open problem and is the core focus of this thesis.

1.2 Scaling SiMOS qubits

The SiMOS platform has many qualities which are beneficial for scaling to the large arrays of qubits required for fault tolerant quantum computation. The footprint of a qubit is extremely small ($\sim 10^3 \text{nm}^2$), meaning that millions of qubits can fit on a single chip. Furthermore, SiMOS qubits can be operated at 1 K with high fidelity, greatly easing requirements on the cryogenic setup's cooling power [18, 27].

However, several challenges relating to scalability remain unresolved. Practical quantum algorithms require classical control circuitry; due to the difficulty of interfacing room temperature and cryogenic electronics, the control system must be hosted on the same chip as the qubits [28]. Hence, the size of the SiMOS qubit footprint is a double-edged sword: the density of the qubit array hinders its integration with control electronics. This necessitates a method of performing quantum operations between distant qubits [28]. In addition, individually addressing each qubit becomes infeasible for large qubit arrays due to qubit crosstalk and limitations on the number of microwave control lines. This could be resolved by using a control scheme capable of simultaneously addressing all qubits in an array with a single microwave field.

1.2.1 Long distance quantum gates

Current two-qubit gates are limited to the exchange interaction between nearest-neighbour qubits, which generally spans tens of nanometres [29]. As a result, there is significant interest in developing a way to perform two-qubit operations over longer distances. A potential method of achieving quantum operations between distant qubits is to use photons in a superconducting resonator. Previous implementations of strong spin-photon coupling for electrons in silicon have required an on-chip micromagnet to couple the spin and charge states of the qubit [30, 31], which introduces additional fabrication steps and is not easily scaled beyond two qubits. This thesis investigates spin-photon coupling using the intrinsic spin-orbit interaction of strongly confined electrons in SiMOS [32], similar to results for hole spins in semiconductors [33]. An intrinsic coupling would eschew the requirement of a micromagnet, enhancing prospects of a

scalable long-distance qubit gate.

1.2.2 Global control of large qubit arrays

Currently, the dominant methods of control in spin qubits use magnetic or electric microwave fields applied to individual spins. This requires a number of microwave transmission lines which rapidly increases with the size of the qubit array [34]. Therefore, existing control methods quickly become infeasible due to qubit crosstalk and heat load when scaling to the thousands of qubits required for fault tolerant quantum computation.

Alternatively, one can use a homogeneous magnetic field provided by a single microwave source capable of driving all qubits simultaneously; this approach is known as *global control*. Dielectric resonators were shown to provide a suitable global driving field for coherent qubit control [35]; however, coherence times of previous experiments were limited by the choice of metal for the gate stack [36]. This thesis presents experimental results on a device with improved fabrication methods which greatly increased coherence times, allowing for the first demonstration of qubits dressed in a dielectric resonator's global field. Tomography techniques are used to benchmark qubit performance, while results from noise spectroscopy experiments provide an insight into the main sources of noise in globally driven qubits.

1.3 Thesis Outline

This thesis researches two topics on the scaling of spin qubit quantum computing: superconducting resonators for spin-photon coupling and dielectric resonators for global control. Chapter 2 gives an overview of theory and previous results for spin qubits, spin-photon coupling and global control. In Chapter 3, the theory of spin-photon coupling is introduced, then experimental results on a SiMOS qubit device are used to consider the theoretical addition of a resonator to the quantum dot system. Chapter 4 details efforts towards the fabrication and integration of a superconducting resonator with a SiMOS quantum dot device. Chapter 5 investigates global control schemes for scalable qubit arrays, driven by a dielectric resonator. Finally, Chapter 6 summarises the advancements presented in this thesis, with an outlook for future research.

Chapter 2

Literature Review

2.1 Spin qubits in semiconductors

Two highly influential papers on quantum computing architectures for semiconductor spin qubits were both published in 1998. Loss and DiVincenzo proposed qubits composed of single electron spins confined by quantum dots in a semiconductor substrate [37] (Fig. 2.1 (a)). The other proposal, by Bruce Kane, encoded qubits in the nuclear spins of phosphorus donors implanted in a silicon substrate [38] (Fig. 2.1 (b)). Both the Loss-DiVincenzo and Kane proposals sparked considerable interest in semiconductor spin qubits as a platform for quantum computation. Early progress was originally made for electrons in gallium arsenide (GaAs) heterostructures, where the initialisation, control and readout of a spin qubit was first shown [39, 40]. However, the nuclear spin of the GaAs substrate was a significant source of qubit dephasing, limiting spin coherence times.

A breakthrough was made with the demonstration of spin qubits in silicon metal-oxide-semiconductor (SiMOS) devices: first for donor-bound electrons [41], then for electrons in gate-defined quantum dots [29, 42] (Fig. 2.2 (a)). The key advantage of silicon substrates is the absence of nuclear spin in the naturally abundant isotope of silicon: silicon-28. By isotopically purifying the silicon wafers to 800 ppm of residual silicon-29, exceptional coherence times allowed for one and two-qubit gate fidelities exceeding 99% [43]. State-of-the-art qubit devices are fabricated on 50 ppm wafers [18, 44], while further innovations in fabrication processes may make even higher purities of silicon-28 possible [45, 46].

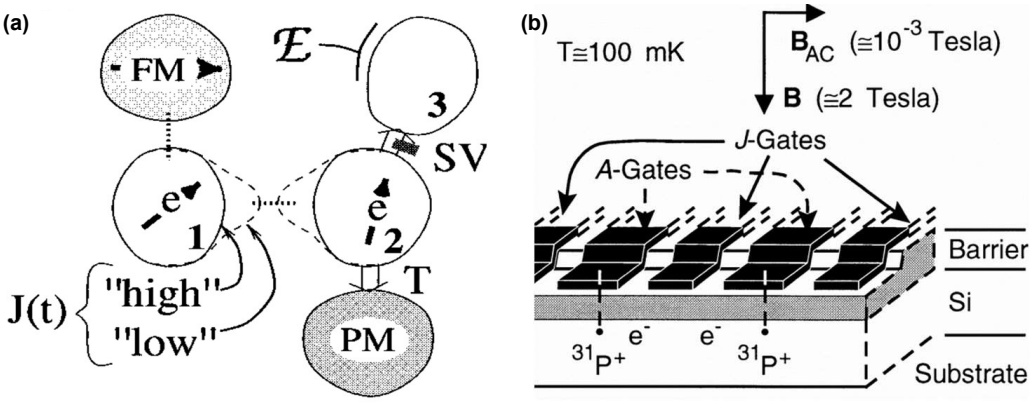

Figure 2.1: **Early semiconductor spin qubit architectures**. **(a)** The Loss-DiVincenzo proposal for electron spin qubits in gate-defined quantum dots (adapted from Ref. [37]) **(b)** The Kane quantum computer, which proposed electron and nuclear spins of phosphorus donors implanted in a silicon substrate (adapted from Ref. [38]). The qubits are driven by a globally applied magnetic field, B_{AC}.

Another benefit of the SiMOS platform is its compatibility with the CMOS fabrication processes ubiquitous in the semiconductor industry. In recent years, devices have gradually progressed away from university cleanrooms towards industrial CMOS foundry processes. Qubits measured on these devices have

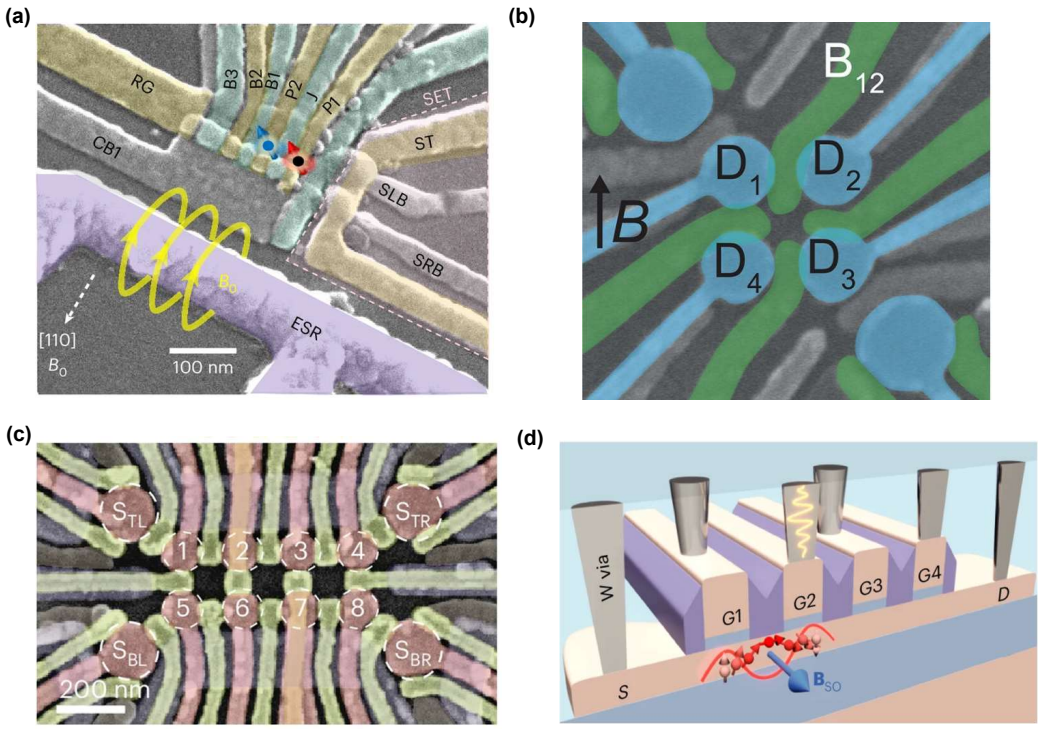

Figure 2.2: **Modern semiconductor spin devices**. Examples of modern spin qubit devices with: **(a)** electrons in SiMOS [43], **(b)** holes in germanium [22], **(c)** electrons in Si/SiGe [47], **(d)** holes in SiMOS nanowires [33].

fidelity metrics comparable to or exceeding previous experiments [48–51].

Si/SiGe heterostructures are also a prominent platform for semiconductor spin qubits which has attracted interest in the research community (Fig. 2.2 (c)). The heterostructures consist of a pure silicon quantum well layer sandwiched by layers of SiGe alloy. Compared to SiMOS substrates, the resulting electron confinement potential is smoother and further from the oxide interface resulting in increased electron mobility, lower percolation density and decreased susceptibility to charge noise [52]. On the other hand, growing the Si/SiGe heterostructures introduces additional complexity to the fabrication process.

Furthermore, the smooth interface between the Si and SiGe layers results in a smaller and more variable valley splitting which can act as an unwanted source of spin-state leakage for Si/SiGe qubits [53, 54].

Electrons are not the only implementation of semiconductor spin qubits: holes, which are unfilled valence band states, also have an effective magnetic moment which can be encoded as a qubit. Promising experimental progress has been made for holes in germanium [22, 55, 56] and silicon [57, 58] (Fig. 2.2 (b,d)). Holes have a far stronger spin-orbit interaction than electrons, making them particularly suitable for electron dipole spin resonance (EDSR) and spin-photon coupling [33,59]. On the other hand, this makes holes particularly susceptible to decoherence from charge noise, though this could be mitigated through careful selection of the qubit control point [58, 60–62].

2.1.1 Initialisation and Readout

The preparation and measurement of qubits with high fidelity is an essential component of a functional quantum computing architecture. Qubit initialisation for quantum dots was first achieved by reloading the electron from an adjacent electron reservoir into the ground state, which is determined by the Zeeman splitting of an externally applied magnetic field [63]. Single-spin relaxation is another option in theory, but relaxation times for spins in silicon are far too long ($T_1 \sim 1\,s$) for practical applications unless valley or orbital-mediated relaxation mechanisms are used [64]. Instead, the predominant method for qubit initialisation uses a double quantum dot isolated from any reservoir. By operating the double dot in a charge configuration with an even number of elec-

trons in both dots, the Pauli exclusion principle guarantees the ground state of a given dot to be the singlet state: the singlet-state relaxation time is typically orders of magnitude faster than for single spins in silicon MOS [65]. The double dot is then pulsed to separate the electron pair into each dot, preparing either a singlet or antisymmetric triplet state depending on the initialisation pulse ramp time [66].

A direct measurement of an electron spin is difficult owing to the extremely small magnitude of a single electron's magnetic moment. Therefore, qubit readout techniques rely on a form of spin-to-charge conversion, where the movement of an electron charge is engineered to be dependent on its spin state. A technique known as Elzerman readout is performed by spin-selective tunneling to an electron reservoir with an energy level in between the spin-up and spin-down states of the qubit in the presence of a magnetic field [63]. However, the density of SiMOS quantum dot arrays may not accommodate electron reservoirs adjacent to all qubits, so this approach is not easily scaled. Elzerman readout also requires a magnetic field large enough to induce a sufficient Zeeman splitting, making it incompatible with qubits at lower magnetic fields or higher temperatures. Pauli spin blockade (PSB) addresses both of these issues; as a result, it is the predominant spin-to-charge conversion method for spin qubits in SiMOS [18,67] and is proposed for use in large-scale semiconductor spin architectures [68,69]. Instead of the dot-to-reservoir tunneling detected by Elzerman readout, PSB uses the interdot transition of electrons in neighbouring quantum dots, where tunneling is only allowed if the electron pair is in the singlet state $\mathrm{S} = (|\uparrow\downarrow\rangle - |\downarrow\uparrow\rangle)/\sqrt{2}$ (this scheme is called *singlet-triplet readout*). For a double quantum dot with a significant g-factor variation caused by spin-orbit interaction, the antiparallel triplet state $\mathrm{T}_0 = (|\uparrow\downarrow\rangle + |\downarrow\uparrow\rangle)/\sqrt{2}$ relaxes quickly

to the singlet state before spin readout is completed. The resulting readout scheme is termed *parity readout* and differentiates the singlet and antiparallel triplet states from the parallel triplet states ($|T_+\rangle = |\uparrow\uparrow\rangle, |T_-\rangle = |\downarrow\downarrow\rangle$) [70].

Charge sensing is most commonly achieved with the use of a nearby single electron transistor (SET). If a quantum dot is made sufficiently small, its I-V characteristic becomes non-Ohmic due to Coulomb interactions between individual electrons: a phenomenon known as the *Coulomb blockade* [71,72]. The SET can then be tuned to a regime with periodic areas of extremely high transconductance (referred to as Coulomb peaks). Therefore, any nearby charge transitions capacitively couple to the SET and cause a detectable change in its current. This approach has been successfully used for single-shot readout in semiconductor spin qubits [73,74], with recently reported fidelities exceeding 99% [50]. Improved readout signal-to-noise ratios (SNRs) have been achieved with the addition of a resonant LC tank circuit attached to the SET, which is probed with radio-frequency reflectometry [75, 76]. This approach has also yielded readout fidelities in excess of 99% in semiconductor qubits [18, 77, 78].

In large qubit arrays, it may not be practical to have SETs adjacent to every qubit. As a result, there has been considerable research effort towards developing gate-based sensing, which use RF reflectometry techniques applied directly to the plunger gate of the quantum dot device [79–81]. High-quality on-chip superconducting resonators have also been used for gate-based dispersive readout [82]. Dispersive readout techniques do not require charge tunnelling and are quantum non-demolition (QND), meaning that they allow the repeated observation of a quantum system's state without destroying it. QND measurements are also possible with SETs if an ancilla qubit is used [83, 84].

2.1.2 Control

2.1.2.1 Single-qubit control

The Loss-DiVincenzo proposal originally offered two implementations of single-qubit control: an AC magnetic field provided by a scanning tunneling microscope tip, or an on-chip ferromagnetic dot which can be connected with spin qubits through the electrical tuning of nearby gates [37]. However, in modern devices single-qubit control is generally performed with an electromagnetic field on-resonance with the qubit frequency, resulting in Rabi oscillations (derived in Appendix A). The driving field may be magnetic or electric: magnetic fields directly drive the electron spin (electron spin resonance, ESR), while electric fields require a degree of spin-charge hybridisation to drive the qubit (electric dipole spin resonance, EDSR). ESR is typically performed with an on-chip antenna [40]: this is still the leading method of control used in SiMOS qubits today [18, 50, 85]. For EDSR, the microwave signal is sent to a gate adjacent to the qubit, directly modulating the electric potential of the qubit. Since electrons typically have a very low spin-orbit effect, an on-chip micromagnet induces a magnetic field gradient to hybridise the spin and charge states of the spin qubit [20, 86, 87]. EDSR has also been demonstrated for tightly-confined electrons in SiMOS with an intrinsic spin-orbit effect due to excited orbital states [32] and for holes in germanium [55] and silicon [57, 58, 88].

A novel approach to qubit control demonstrated recently is the use of *hopping spins* to perform single-qubit operations. First demonstrated for holes in Germanium, gates are implemented by shuttling the spin between dots with a difference in spin quantisation axis due to the hole spin's strong spin-

orbit coupling. By precisely engineering the timing of the shuttling operation, single-qubit gates with fidelities well above the fault-tolerant threshold were observed [89]. Shuttling-based control is also advantageous because it eschews the need for a microwave frequency driving field. In this way, it is somewhat analogous to the Loss-DiVincenzo proposal: the ferromagnetic dots of the original paper are substituted for the intrinsic spin-orbit coupling of holes in Ge. In principle, hopping spin gates can be performed for any system with a large spin-orbit interaction; this could include electrons with an intrinsic spin-orbit coupling [32] or an on-chip micromagnet [20].

All of the control schemes described in this section are a form of *local control*, where qubits are addressed individually and sequentially for qubit operations. This presents several challenges when scaling to large qubit arrays. Addressing many qubits individually requires the qubits to be spread out over a frequency range large enough to avoid crosstalk [90]. The addition of frequency multiplexing hardware to the microwave signal chain is a potential source of electrical noise and heat load to the cryogenic setup [20, 91]. One possible solution to these issues is the use of a global microwave field to control the entire qubit array simultaneously [38]. Previous experiments on global control schemes will be reviewed in detail in Section 2.4.

2.1.2.2 Two-qubit gates

Two-qubit gates are based on the Heisenberg exchange interaction and can be performed between nearest-neighbour qubits by tuning the interdot barrier potential such that the electron wavefunctions overlap. The most practical implementation of a two-qubit gate in spin qubits depends on the relative sizes

of the exchange interaction J and Zeeman splitting E_{Z}. When the two spins are on resonance ($E_{\mathrm{Z}} \ll J$), pulsing the exchange interaction results in a SWAP gate coupling the $|\uparrow\downarrow\rangle$ and $|\downarrow\uparrow\rangle$ spin states. On the other hand, for far-detuned qubits ($E_{\mathrm{Z}} \gg J$), the exchange interaction causes a frequency shift in one qubit dependent on the state of the other: in essence, this is a controlled-Z (CZ) gate. A controlled-NOT (CNOT) gate is performed by combining the CZ gate with either sequentially [29] or simultaneously [92] applied single qubit operations.

Two-qubit exchange oscillations were first observed in GaAs [39], followed by demonstrations of two-qubit CNOT gates in SiMOS [29] and Si/SiGe [92]. Improvements in device design, fabrication, and operation have resulted in several reports of two-qubit gate fidelities above 99% [21, 50, 93]. These two-qubit gates can only be performed between adjacent qubits; there is significant interest in researching two-qubit operations between distant qubits.

2.2 Superconducting resonators

Superconducting resonators have a wide range of applications in quantum computing including single photon detection [94], parametric amplification [95,96], and as a key component of superconducting qubits [10, 97, 98]. The phenomenon of superconductivity results in resonators with zero resistivity, making extremely high quality factors possible.

2.2.1 Coplanar waveguide resonators

The most common type of resonator used in cQED experiments is the coplanar waveguide (CPW), which consists of a single signal trace flanked by two ground planes (Fig. 2.3) [99]. The planar design of the CPW makes it especially compatible with lithography processes commonly used in semiconductor fabrication.

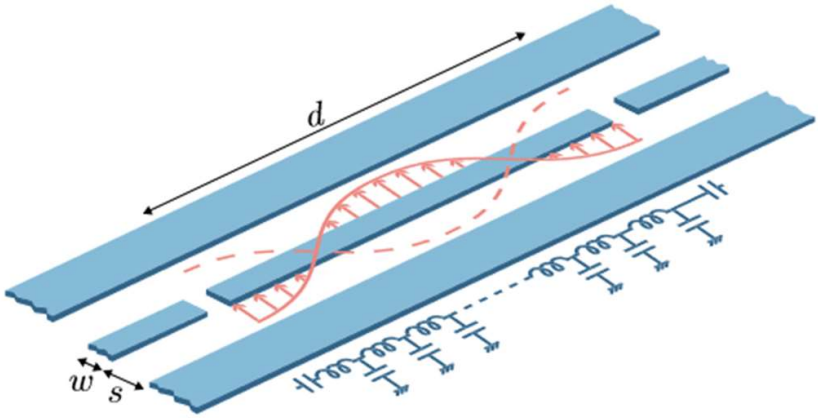

Figure 2.3: **Illustration of a superconducting resonator**. A typical CPW resonator is depicted with antinodes in the electric field (orange) at each end. The lumped-element model of the resonator is depicted in blue. Adapted from Ref. [100].

The characteristic impedance Z_0 and effective permittivity ϵ_{eff} of the coplanar waveguide can be computed from the resonator dimensions and substrate permittivity [101]:

$$Z_0 = \frac{30\pi}{\sqrt{\epsilon_{\text{eff}}}} \frac{K(k_0')}{K(k_0)}, \tag{2.1}$$

$$\epsilon_{\text{eff}} = \frac{\epsilon_{\text{s}} + 1}{2}, \tag{2.2}$$

where

$$k_0 = \frac{w}{w + 2s}, \tag{2.3}$$

$$k_0' = \sqrt{1 - k_0}, \tag{2.4}$$

$$\tag{2.5}$$

w and s are the resonator conductor width and ground plane separation respectively, ϵ_s is the electric permittivity of the substrate, and $K(k)$ is the complete elliptic integral of the first kind. This assumes that $s, w \ll t_s$ where t_s is the thickness of the substrate. This condition is satisfied for the resonators measured in this thesis, where $s = 5\,\mu\text{m}, w = 25\,\mu\text{m}$, and $t_s \approx 1\,\text{mm}$. From Eqs. 2.1 and 2.3, it is evident that the resonator impedance depends only on the CPW parameters w and s, and that reducing w relative to s increases the impedance. A simple representation of the CPW is the lumped-element model, which breaks the resonator down into an infinite chain of infinitesimally small series inductances and parallel capacitances (Fig. 2.3).

A resonator terminated by antinodes (i.e. open circuits) will act as a $\lambda/2$ resonator with maximal electric field fluctuations (minimal magnetic field fluctuations) at both ends. For a resonator of length d, the fundamental mode of the $\lambda/2$ resonator occurs at frequency $f_0 = v_{\text{eff}}/2d$, where $v_{\text{eff}} = c/\sqrt{\epsilon_{\text{eff}}}$ is the phase velocity of light in the waveguide. For applications where the resonator is desired to be in the vacuum state (e.g. spin-photon coupling), the resonator frequency should be high enough to avoid thermal photons: $hf_0 \gg k_B T = 2.08\,\text{GHz}$ for a base dilution refrigerator temperature of $T = 10\,\text{mK}$. Therefore, resonance frequencies in the range 4–8 GHz are commonly chosen due to the abundance of microwave electronics available in this frequency band.

2.2.2 Resonator quality and coupling regimes

Quality factor (Q-factor) is a quantitative measure of a resonator's ability to store energy without loss. It is defined as the ratio of the resonator frequency f_r to the resonator linewidth:

$$Q_{\text{total}} = \frac{f_r}{\Delta f}, \tag{2.6}$$

with Δf defined as the full width at half maximum (FWHM) of the resonator's magnitude response. The quality factor can be separated into components based on loss mechanism, for example:

$$\frac{1}{Q_{\text{total}}} = \frac{1}{Q_{\text{i}}} + \frac{1}{Q_{\text{c}}}, \tag{2.7}$$

where Q_{c} is the coupling quality factor representing losses from coupling to input/output ports of the resonator and Q_{i} is the internal quality factor indicative of resistive, radiative or dielectric losses. Q_{c} is easily engineered by changing the inductive/capacitive coupling at the resonator ports, while Q_{i} is an intrinsic value dependent on device fabrication, materials and design.

When $Q_{\text{c}} < Q_{\text{i}}$, the resonator is overcoupled and the majority of photon loss is through the input/output ports. This regime is ideal for readout resonators since the readout signal increases with Q_c. When $Q_{\text{c}} > Q_{\text{i}}$, the resonator is undercoupled. Q_{total} is inversely proportional to the resonator decay rate; as a result, undercoupled resonators are generally ideal for spin-photon coupling.

2.2.3 Kinetic Inductance

Kinetic inductance is a phenomenon caused by the inertia of electrons in an alternating field. In normally conducting wires, this effect is usually not signif-

icant since the collision time of electrons in a wire is far less than the frequency of the field. However, when the wire is superconducting and driven at a high frequency, kinetic inductance emerges as a phase delay in voltage due to the inertia of the electron. High kinetic inductance materials are typically *dirty superconductors*, which are superconducting materials with impurities such that the electron mean free path is much shorter than the superconducting coherence length [102]. The impurities may be physical (e.g. superconducting quantum interference devices (SQUIDs) [103]) or chemical (e.g. a superconductor interspersed with insulating materials such as NbTiN, TiN or granular aluminium).

An expression for the kinetic inductance L_{k} can be derived from Mattis-Bardeen theory [104], given by

$$L_k = \left(\frac{d}{w}\right) \frac{R_{\mathrm{sq}} h}{2\pi^2 \Delta} \coth\left(\frac{\Delta}{2k_B T}\right), \tag{2.8}$$

where d and w are the length and width of the resonator's central trace, R_{sq} is its normal-state resistance per square, and Δ is the material's superconducting gap. Therefore, the kinetic inductance of a material can be estimated by simply measuring its room temperature resistance. By combining these two approaches, it is possible to increase the characteristic impedance of a resonator by several orders of magnitude over the common $50\,\Omega$ impedance resonator [59, 105, 106]. However, there are added challenges when using high impedance resonators. Since the capacitance of the resonator is smaller, parasitic capacitances form a greater fraction of the total. As a result, unwanted microwave leakage is increased, making it more difficult to overcouple the resonator [107].

2.2.4 Superconducting resonator materials

Several criteria are important when selecting a suitable resonator material:

- **Magnetic field resilience**
  The superconductor's critical field must be high enough to withstand the typical operating magnetic fields of spin qubits ($\sim 500\,\mathrm{mT}$) [108]. Resonator quality factor also degrades with magnetic field, and is especially sensitive to fields perpendicular to the plane of the substrate [105, 109].
- **Kinetic inductance**
  To maximise the spin-photon coupling rate, high kinetic inductance materials are desirable.
- **Thermal budget**
  For SiMOS qubits, a forming gas anneal is an essential step at the end of the fabrication process. Hence, the resonator material should be resilient to temperatures of up to about 400 °C. This requirement can be avoided if the resonator is fabricated after the quantum dot structure.

2.2.4.1 Niobium Titanium Nitride (NbTiN)

Previous demonstrations of strong spin-photon coupling have used NbTiN [31, 110] due to its magnetic field stability and high kinetic inductance. Samkharadze et al. [105] found that NbTiN resonators maintained quality factors greater than 10^5 for parallel magnetic field strengths of up to 6 T. The impedance of the resonator was approximately $4\,\mathrm{k}\Omega$.

2.2.4.2 Granular Aluminium (grAl)

Granular aluminium is an novel material first proposed for use in superconducting qubits by Grunhaupt et al. [111]. By introducing oxygen gas during aluminium deposition, the aluminium forms small grains of diameter 3 nm coated with a layer of aluminium oxide. The kinetic inductance, critical field and critical temperature all depend on the oxide content, which is easily tuned by varying the oxygen pressure when depositing the film. As grAl is a dirty superconductor, it has significantly improved critical temperature and critical field when compared to pure aluminium [112]. Granular aluminium also has very high kinetic inductance, as high as 1.2 nH/sq [113], which is an order of magnitude higher than reported for NbTiN. Strong charge-photon coupling was recently achieved for granular aluminium resonators coupled to holes in germanium [59].

2.2.4.3 Molybdenum Rhenium (MoRe)

Molybdenum rhenium also exhibits high magnetic field stability and resistance to high temperatures: Q-factors approaching 10^5 were measured for annealed resonators [114]. The fabrication process of MoRe is also easier than other superconductors, as it can be sputtered without the need for nitrogen or oxygen gas in the deposition chamber [115].

2.3 Spin-photon coupling

The coupling between a spin qubit and photon belongs to the field of cavity quantum electrodynamics (cQED), which describes the interaction between any two-level system (such as a qubit) and the electric field of a cavity (such as a superconducting CPW resonator). The qubit can be described as a two-level system with ground and excited states $|g\rangle$ and $|e\rangle$ separated by an energy $\hbar\omega_q$. The qubit Hamiltonian, H_q is

$$H_q = \frac{\hbar\omega_q}{2}\hat{\sigma}_z, \tag{2.9}$$

where $\hat{\sigma}_z$ is the Pauli-Z operator. The resonator Hamiltonian, H_r is

$$H_r = \hbar\omega_r \hat{a}^\dagger \hat{a}, \tag{2.10}$$

where ω_r is the resonant frequency and $\hat{a}^\dagger$ ($\hat{a}$) is the bosonic creation (annihilation) operator. The Hamiltonian H_{int} describing the qubit-resonator interaction can be derived by way of the rotating wave approximation as [116]

$$H_{\text{int}} = \hbar g \left(\hat{\sigma}_+ \hat{a} + \hat{\sigma}_- \hat{a}^\dagger\right), \tag{2.11}$$

where $\hat{\sigma}_+ = |e\rangle\langle g|$ and $\hat{\sigma}_- = |g\rangle\langle e|$ are the qubit's raising and lowering operators respectively, and g is the vacuum Rabi coupling. The Hamiltonian of the combined qubit-resonator system is

$$H_{JC} = H_q + H_r + H_{\text{int}} \tag{2.12}$$

$$= \frac{\hbar\omega_q}{2}\hat{\sigma}_z + \hbar\omega_r \hat{a}^\dagger \hat{a} + \hbar g \left(\hat{\sigma}_+ \hat{a} + \hat{\sigma}_- \hat{a}^\dagger\right), \tag{2.13}$$

This is the Jaynes-Cummings Hamiltonian commonly used to describe light-matter interactions in cQED [117]. As detailed in Chapter 3, an electron with

spin-orbit interaction cannot be described with a simple two-level model; in this case, the Jaynes-Cummings Hamiltonian is not sufficient to derive the spin-photon coupling strength.

The strong coupling regime is achieved when the coherent spin-photon coupling strength g is greater than the decoherent processes of resonator decay κ and spin dephasing γ. In 2017, three independent demonstrations of strong spin-photon coupling were published in the space of a year for electrons in Si/SiGe [30, 31] and resonant exchange qubits in GaAs [110]. The key innovations of these devices were the additional spin-charge hybridisation provided by a micromagnet or multi-electron qubit, and the use of resonator materials and geometry which greatly increased the resonator impedance. In the work by Samkharadze et al. [105], NbTiN resonators with an impedance of 3 kΩ and Q-factors above 3000 were achieved. Subsequent studies reported coherent spin-spin interactions [118, 119], culminating in the first two-qubit logic gate mediated with a superconducting resonator, albeit with poor spin coherence ($T_2^* \approx 80$ ns, $T_1 \approx 260$ ns) [120]. Strong coupling was also reported for hole spin qubits in silicon MOS nanowires [33], with a high spin-photon coupling strength of 330 MHz attributable to the strong spin-orbit effect of holes.

2.4 Global control and dressed qubits

One of the first ideas for a spin-based quantum computer was outlined by Kane in 1998, which envisioned an array of phosphorus donors embedded in a silicon substrate [38]. Kane's proposal for a quantum computer introduced the concept of global control, using an off-resonant always-on global magnetic

field. Qubit operations were performed by electrically tuning the qubit into resonance with the global field [38, 121]. Since the global field can drive all qubits simultaneously and with a single microwave source, it mitigates the wiring, heating and frequency crowding issues associated with local control methods (Sec. 2.1.2.1). This makes global control schemes advantageous when scaling to large qubit arrays.

Recent research on global control has investigated qubits *dressed* in a driving microwave field as a way to improve the coherence times of spin qubits [122, 123]. Advanced dressing protocols which modulate the amplitude of the global field have been proposed to more effectively cancel errors in qubit Larmor and Rabi frequencies [124, 125]. An experimental demonstration of always-driven two-qubit control was recently achieved with an on-chip ESR antenna in SiMOS qubits [85]; however, ESR antennas are not scalable to large, globally controlled arrays because of their large footprint and localised magnetic field. Dielectric resonators are an alternative global field source capable of providing a homogeneous magnetic field with low microwave loss.

2.5 Dielectric Resonators

Dielectric resonators are compact, high-performance components that confine electromagnetic energy within a dielectric material to produce resonances at microwave and millimetre-wave frequencies. They are widely used in microwave circuits as filters, oscillators, and antennas due to their low loss, easy on-chip integration and good power-to-field conversion factors. Dielectric resonators are widely used in ESR spectroscopy experiments [126–128]; however, spin res-

onance for applications in quantum computing was only achieved relatively recently [35, 36]. The dielectric material used in these experiments was potassium tantalate ($KTaO_3$), which has an extremely high electric permittivitty ($\epsilon_r > 4 \times 10^3$ for $T = 4\,\mathrm{K}$) and low loss tangent $\delta \sim 10^{-3}$ at cryogenic temperatures [129]. An internal quality factor of 6×10^4 was reported for $KTaO_3$ dielectric resonators in Ref. [35].

For the purposes of spin resonance, it is desirable to drive with a purely magnetic AC field, with the electric field entirely confined within the dielectric resonator. Hence, the fundamental transverse electric (TE) mode, $TE_{11\delta}$, is used (Fig. 2.4). The resonant frequency of a dielectric resonator can be calculated from its dimensions and electric permittivity, with the use of Marcatili's approximation [130]. For a rectangular resonator with height h and cross-sectional dimensions a and b, the $TE_{11\delta}$ mode resonant frequency is [131]:

$$f_r = \frac{k_0}{\sqrt{\epsilon_0 \mu_0}}. \tag{2.14}$$

Here, k_0 is the free-space wavenumber given by

$$\varepsilon_r k_0^2 = k_x^2 + k_y^2 + k_z^2, \tag{2.15}$$

where

$$k_x = \frac{\pi}{a}; \quad k_y = \frac{\pi}{b}, \tag{2.16}$$

$$k_z \tan\left(\frac{k_z h}{2}\right) = \sqrt{(\varepsilon_r - 1)k_0^2 - k_z^2}, \tag{2.17}$$

from which a solution for k_0 can be calculated.

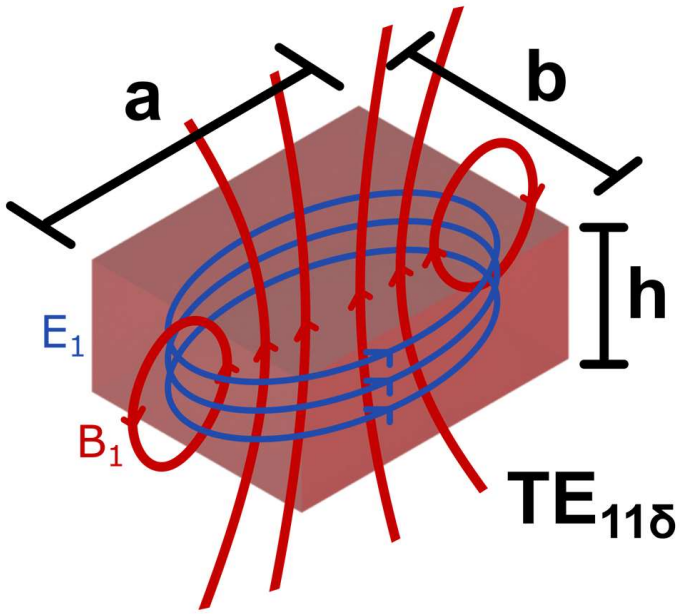

Figure 2.4: **Illustration of a dielectric resonator**. Electric (red) and magnetic (blue) field lines are depicted for the $TE_{11\delta}$ mode. Adapted from Ref. [35].

2.6 Gate Set Tomography

Gate Set Tomography (GST) is a robust and highly precise method used to characterise the behaviour of quantum gates, especially in the presence of noise and systematic errors [132]. Unlike quantum process tomography, which focuses on reconstructing a single gate, GST characterises an entire set of quantum gates along with the state preparation and measurement (SPAM) errors. GST works by preparing a variety of input states, applying sequences of gates, and then performing measurements on the output states. The advantage of GST over other error characterisation protocols (such as randomised benchmarking) lies in its ability to evaluate SPAM errors and to distinguish between Hamilto-

nian and stochastic errors. This makes GST a powerful tool for benchmarking quantum gates and identifying and correcting for sources of qubit error. While GST was first applied to trapped ion qubits [133], it has since been used for a wide variety of qubit platforms including silicon spin qubits [43, 134, 135].

Chapter 3

Theory of spin-photon coupling in silicon MOS qubits

This chapter includes work from the following manuscript which has been submitted for publication: K. S. Guo, M. Feng, J. Y. Huang, W. Gilbert, K. M. Itoh, F. E. Hudson, K. W. Chan, W. H. Lim, A. S. Dzurak, A. Saraiva. Methods for trans verse and longitudinal spin-photon coupling in silicon quantum dots with intrinsic spin-orbit effect. Submitted to Phys. Rev. Applied. Preprint available: arXiv:2308.12626 [cond-mat.mes-hall]

The experimental data presented in this chapter was collected by the author, Jonathan Huang and Will Gilbert, with theoretical analysis by the author and Mengke Feng. Wee Han Lim and Fay Hudson fabricated the device.

3.1 Intrinsic spin-orbit effect in silicon MOS qubits

Electron spin qubits in silicon typically have a very low intrinsic spin-orbit effect [136, 137]. As a result, electron dipole spin resonance (EDSR) is usually achieved with an extrinsic spin-orbit coupling engineered with an on-chip micromagnet [86, 87], an approach which is also commonly used for electrons in Si/SiGe heterostructures [138, 139]. However, electrons in SiMOS which are strongly confined within a dense gate layout can be tuned in a way such that the orbital states (which have a significantly higher spin-orbit coupling) can be accessed. Experiments exploiting these excited states have demonstrated all electric drive using EDSR with substantial increases in Rabi frequency while maintaining single qubit gate fidelities in excess of 99.9% [32].

This configuration lends itself naturally to spin-photon coupling, since the qubit's EDSR drive can be readily provided by the electric field of photons in a superconducting resonator. An advantage to the intrinsic coupling is that there is no micromagnet required, relaxing fabrication constraints and improving scalability prospects.

This chapter combines experimental data on electron spin qubits in SiMOS with cQED theory to estimate expected spin-photon coupling parameters with the integration of a suitable superconducting resonator.

3.1.1 Experimental Setup

In order to evaluate the spin-photon coupling strength, experiments were performed on an electron SiMOS device to characterise the spin-orbit coupling. The device and experimental setup are the same as those presented in Ref. [32]. A false coloured SEM image is shown in Fig. 3.1.

Electrons are accumulated under the P2 and P3 gates in the (3,1) charge configuration. The single electron under P3 is the target qubit, while the electron under P2 is used as an ancilla. A static magnetic field $B_0 = 700\,\mathrm{mT}$ is applied to the device. Readout is measured by spin-to-charge conversion via Pauli spin blockade (PSB), which is detected by an adjacent single electron transistor (SET). EDSR is performed by applying microwave pulses to the CB, J1 or J2 gates.

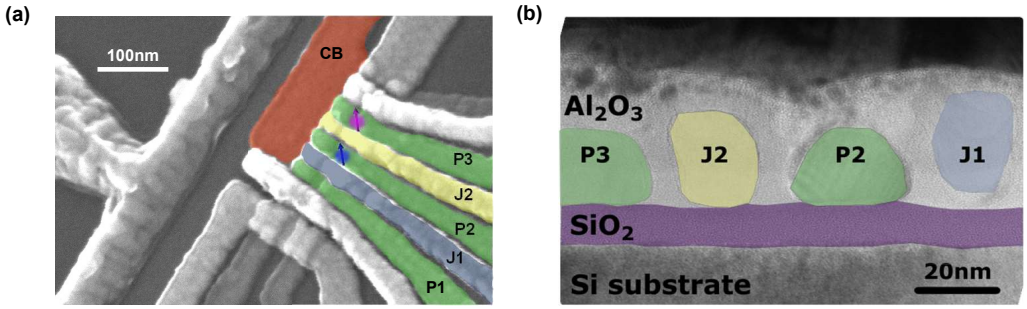

Figure 3.1: **Device layout (a)** False-coloured scanning electron microscopy (SEM) image of a device nominally identical to the measured device. EDSR is performed on the qubit under P3 (purple), while the qubit under P2 (blue) is used as an ancilla for readout. **(b)** False-coloured SEM cross-section showing substrate, silicon oxide layer (purple) and aluminium gate stack with native oxide (white).

3.1.2 Theoretical model

A four-level model is used to describe the qubit energy spectrum, consisting of the spin states $|\uparrow\rangle$ and $|\downarrow\rangle$ split by the external magnetic field and the orbital states $|A\rangle$ and $|B\rangle$. The Hamiltonian of the qubit is presented in Eq. 3.1 in the basis $\{|A\rangle, |B\rangle\} \otimes \{|\uparrow\rangle, |\downarrow\rangle\}$

$$\hat{H}_{\mathrm{qd}} = \begin{bmatrix} \frac{1}{2}E_{\mathrm{Z}}^{\mathrm{A}} + \eta_{\mathrm{A}}(V_{\mathrm{J}}) & 0 & \Delta + \Delta_{\mathrm{sd}} & \Delta_{\mathrm{sf}} \\ 0 & -\frac{1}{2}E_{\mathrm{Z}}^{\mathrm{A}} - \eta_{\mathrm{A}}(V_{\mathrm{J}}) & \Delta_{\mathrm{sf}} & \Delta - \Delta_{\mathrm{sd}} \\ \Delta + \Delta_{\mathrm{sd}} & \Delta_{\mathrm{sf}} & \frac{1}{2}E_{\mathrm{Z}}^{\mathrm{B}} + (\eta_{\mathrm{B}} + \beta_1)V_{\mathrm{J}} & 0 \\ \Delta_{\mathrm{sf}} & \Delta - \Delta_{\mathrm{sd}} & 0 & -\frac{1}{2}E_{\mathrm{Z}}^{\mathrm{B}} - (\eta_{\mathrm{B}} - \beta_1)V_{\mathrm{J}} \end{bmatrix}, \tag{3.1}$$

where $E_{\mathrm{Z}}^{\mathrm{A(B)}}$ are the Zeeman splittings for each orbital state, $\eta_{\mathrm{A(B)}}$ are their respective linear Stark shifts, β_1 is the differential lever arm between the two orbitals, V_{J} is the applied gate voltage on the J gate (either J1 or J2 depending on the regime), Δ is the inter-orbital coupling between the orbitals, Δ_{sd} is the spin-dependent component of spin-orbit coupling, and Δ_{sf} is the spin-flip component of the spin-orbit coupling [140]. The orbital terms Δ, Δ_{sd} and Δ_{sf} are dependent on the electric confinement of the qubit, giving access to a variety of different spin-orbit coupling schemes by tuning nearby gate voltages. The gates with the most influence on the orbital terms are the CB and J gates since they are in close proximity to the electron and strongly control its lateral confinement.

To model the speedup in Rabi frequency as the spin-orbit coupling changes, a

Hamiltonian $\hat{H}_{\mathrm{AC}}$ is introduced with driving amplitude Ω_{AC}:

$$\hat{H}_{\mathrm{AC}} = \Omega_{\mathrm{AC}} \cdot \begin{bmatrix} 0 & 0 & 1 & 0 \\ 0 & 0 & 0 & 1 \\ 1 & 0 & 0 & 0 \\ 0 & 1 & 0 & 0 \end{bmatrix}. \tag{3.2}$$

With this, the Rabi frequency is defined as the coupling between the ground state, $|g\rangle$, and the 1st excitation state, $|e\rangle$, of $\hat{H}_{\mathrm{AC}}$ in the eigenbasis of $\hat{H}_{\mathrm{qd}}$, and can be calculated as $f_{\mathrm{Rabi}} = \left|\langle e| \hat{H}_{\mathrm{AC}} |g\rangle\right|$.

3.1.3 PESOS maps

To probe the qubit's spin-orbit dynamics, a pulsed electron spin-orbital spectroscopy (PESOS) map is measured by sweeping the J2 gate voltage and microwave frequency while applying a microwave pulse with a fixed duration (0.5 µs in Fig. 3.2(a)). The fixed microwave duration reveals any changes in Rabi frequency as nutation patterns that appear alongside the main resonance [32]. The spin-orbit coupling is strongest when the orbital and spin states become degenerate; for the PESOS map in Fig. 3.2(a), the orbital degeneracy point occurs when $V_{\mathrm{J2}} = 1.624\,\mathrm{V}$. By fitting the qubit frequency and Rabi frequency from the PESOS map to the four-level model, all parameters of the Hamiltonian in Eq. 3.1 can be extracted. The fitted four-level model is plotted in Fig. 3.2(b), with Rabi frequency plotted in Fig. 3.2(c). The fitted Rabi frequency reaches a maximum of 32 MHz at the orbital degeneracy, a value which is confirmed by counting the number of interference fringes visible in the PESOS map (14 visible fringes corresponds to a 29-fold increase in the Rabi frequency).

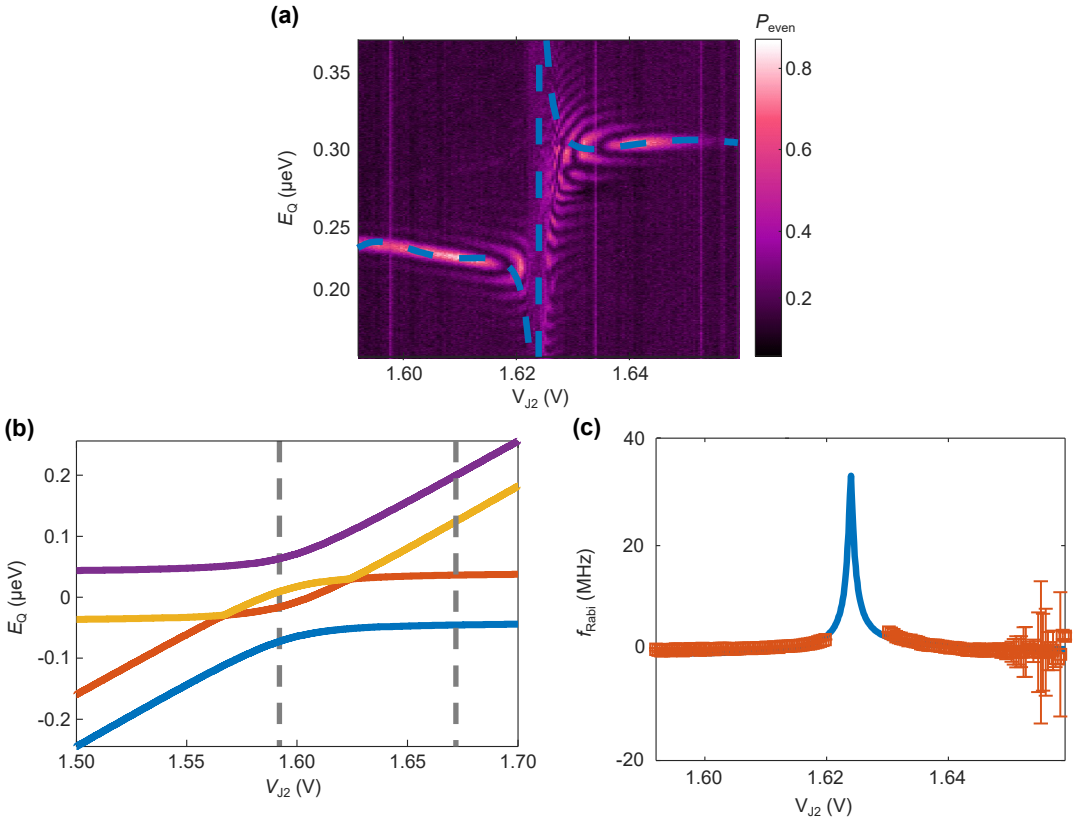

Figure 3.2: **Four-level model of electron qubit with spin-orbit coupling (a)** A PESOS map obtained at 700 mT with 15 dBm drive on the CB gate. Fitted qubit frequency plotted in blue. Colorbar indicates even state probability. **(b)** Four-level model obtained from fitting of the PESOS map. The vertical grey dashed lines correspond to the voltage range plotted in (a). **(c)** Extracted Rabi frequencies f_{Rabi} from the PESOS map (orange), with a fit (blue) based on the four-level model.

3.1.4 Resonator and Interaction Hamiltonians

The analysis so far has solely focused on the spin qubit described by its Hamiltonian $\hat{H}_{\mathrm{qd}}$. To obtain the full qubit-resonator system, the resonator and interaction Hamiltonians, $\hat{H}_{\mathrm{res}}$ and $\hat{H}_{\mathrm{int}}$, are added:

$$\hat{H}_{\mathrm{res}} = \hbar\omega_{\mathrm{res}} a^{\dagger} a, \tag{3.3}$$

where ω_{res} is the resonant frequency of the superconducting resonator and $a^{\dagger}$ and a are the creation and annihilation operators, and

$$H_{\mathrm{int}} = \hbar[g_{\perp}\sigma_x(a + a^{\dagger}) + \delta\omega\sigma_z(a^{\dagger}a + \frac{1}{2}) + g_{\parallel}\sigma_z \cos(\omega_{\mathrm{m}}t + \varphi_{\mathrm{m}})(a + a^{\dagger})] \tag{3.4}$$

The interaction Hamiltonian contains three terms: the first is proportional to $g_{\perp}$ and describes an on-resonance transverse spin-photon coupling which was previously used to demonstrate strong spin-photon coupling for electrons in Si/SiGe and holes in SiMOS [30, 31, 33]. The second term is a dispersive coupling with strength $\delta\omega$ which couples the qubit energy levels to the number of photons in the resonator. Finally, applying a sinusoidal modulation to the voltage on a nearby gate with frequency ω_{m} and phase ϕ_{m} gives rise to a dynamic longitudinal coupling with strength $g_{\parallel}$ which is proportional to the curvature of the qubit energy.

Therefore, the Hamiltonian of the total spin-resonator system is

$$\hat{H}_{\mathrm{tot}} = \hat{H}_{\mathrm{res}} + \hat{H}_{\mathrm{qd}} + \hat{H}_{\mathrm{int}}, \tag{3.5}$$

3.2 Transverse spin-photon coupling

The transverse spin-photon coupling scheme uses the electric field of photons in the resonator to directly drive Rabi oscillations in the qubit. In the eigenbasis of Hqd, a single photon in the resonator introduces an electric drive with magnitude

$$\Omega_{\mathrm{AC,ZPF}} = \frac{\alpha_{\mathrm{r}}}{2} V^0_{\mathrm{ZPF}}, \tag{3.6}$$

where α_{r} is the lever arm of the gate the resonator is connected to, and V^0_{ZPF} is the resonator's zero-point fluctuation of voltage with impedance Z_r

$$V^0_{\mathrm{ZPF}} = \omega_{\mathrm{r}} \sqrt{\frac{2Z_{\mathrm{r}}}{\pi\hbar}}. \tag{3.7}$$

The transverse spin-photon coupling strength is

$$\frac{g_\perp}{2\pi} = f_{\mathrm{Rabi,ZPF}}. \tag{3.8}$$

Therefore, to estimate $f_{\mathrm{Rabi,ZPF}}$ and calculate the expected transverse spin-photon coupling strength, Rabi oscillations were measured for varying EDSR drive amplitude, then the Rabi frequency was extrapolated down to the single-photon voltage fluctuations V^0_{ZPF} expected in a high-impedance resonator.

3.2.1 Microwave induced interdot transition broadening

The microwave drive used for EDSR is generated by a vector signal generator. However, because the attenuation of microwave signal from generator to gate is unknown, the actual voltage amplitude applied to the gate is ascertained by probing the microwave induced broadening of the $(4,0) \leftrightarrow (3,1)$ charge transition.

Fig. 3.3(a) shows the interdot charge transition induced by sweeping the CB gate voltage. As the microwave signal applied to the CB gate is increased, a clear broadening of the RFSET signal is observed, which is fitted to the Fermi-Dirac distribution

$$F(\epsilon) = \frac{A}{e^{(\epsilon-\mu)/W}+1} + B. \tag{3.9}$$

The parameter of interest is the transition width W, while A and B are constants which result from the normalisation of the RFSET signal. Linear regression is used to fit the broadening of the transition (Fig. 3.3(b)), which is used to convert the microwave power to the voltage applied at the gate. This methodology was repeated for the J2 and J1 gates, allowing for the conversion of microwave powers at the generator to actual voltages at the gate. While this technique does not account for heating effects at higher powers, any thermal broadening would be additive. Therefore, attributing all broadening to the microwave source gives an upper bound for the driving amplitude. This approach yields minimum line attenuations of 77 dB, 72 dB, and 75 dB from the microwave source to the CB, J1, and J2 gates respectively.

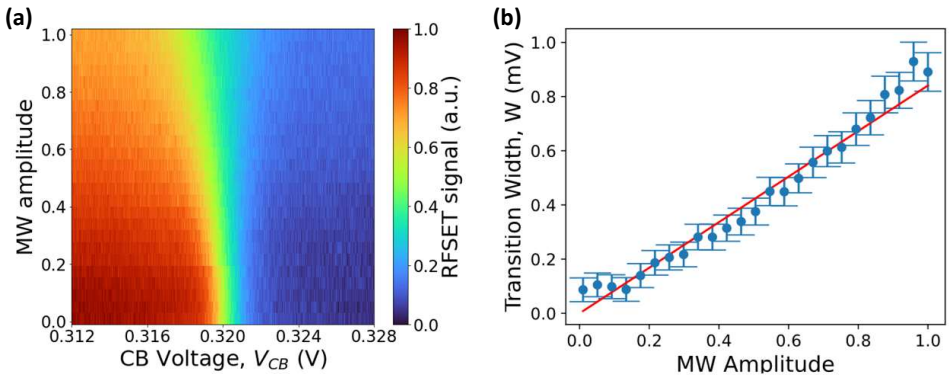

Figure 3.3: **Interdot charge transition broadening** (a) The $(4,0) \leftrightarrow (3,1)$ charge transition caused by the CB gate as a function of microwave drive amplitude. An amplitude of 1 corresponds to 15 dBm at the microwave signal generator. (b) Width of the transitions (fitted to Eq. 3.9) for varying microwave amplitudes.

3.2.2 Calculating spin-photon coupling, $g_\perp$

To estimate $f_{\text{Rabi,ZPF}}$ and calculate the expected transverse spin-photon coupling strength, Rabi oscillations were measured on the device described in 3.1.1 which is without a resonator. The Rabi frequency was extrapolated down to the single-photon voltage fluctuations V^0_{ZPF} expected in a high-impedance resonator.

Figure 3.4(a) shows the PESOS map of the device under an external magnetic field of 700 mT, operating near the orbital degeneracy point at $V_{\text{J2}} = 1.598$ V. A speedup in the Rabi frequency caused by spin-orbit coupling is evident through the interference fringes in the PESOS map.

Rabi oscillations were measured while sweeping the applied microwave power. This experiment was then repeated while applying the microwave drive to the the CB, J1 and J2 gates. The Rabi frequency f_{Rabi} increased linearly with

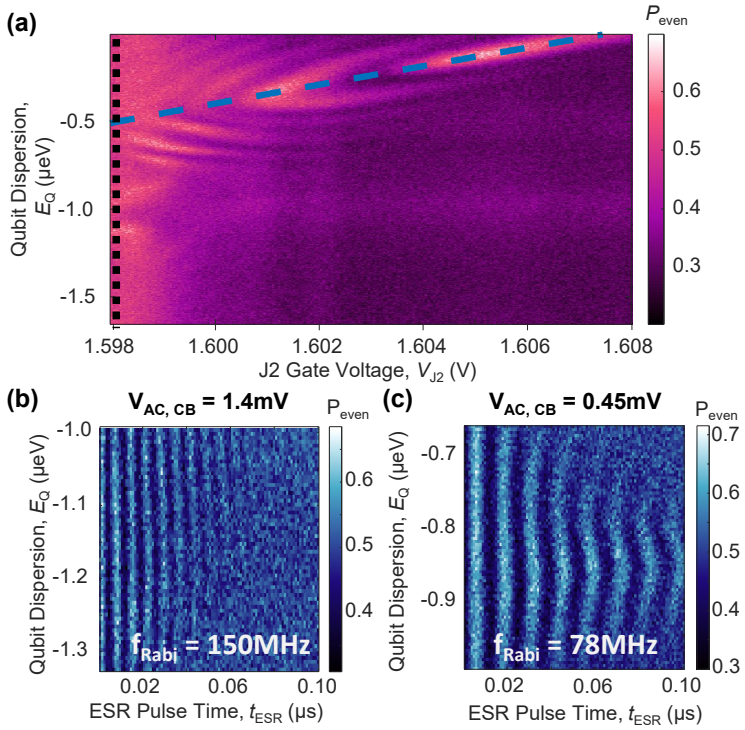

Figure 3.4: **Rabi oscillations (a)** PESOS map taken at $B_0 = 700$ mT. The blue dashed line plots the fitted qubit frequency, black dotted line indicates the voltage applied on the J2 gate where Rabi chevrons were measured. **(b)** Rabi oscillations measured when applying a EDSR pulse on the CB gate with 1.4 mV amplitude (equivalent to 20 dBm power on the microwave source). **(c)** Rabi oscillations measured when applying a EDSR pulse on the CB gate with 0.45 mV amplitude (equivalent to 10 dBm power on the microwave source).

increasing drive voltage (Fig. 3.5). At voltage amplitudes above 0.7 mV, a tapering effect was observed (grey points in Fig. 3.5), consistent with previous experiments on similar devices [32, 36]. These data points were excluded from the fit since they are not relevant at single-photon levels. The voltage amplitude at single-photon levels for a superconducting resonator is

$$V_{\mathrm{ZPF}}^{0} = \omega_{\mathrm{r}} \sqrt{\frac{2Z_{\mathrm{r}}}{\pi\hbar}}. \tag{3.10}$$

For a typical high-impedance resonator with resonant frequency $\omega_{\mathrm{r}} = 6$ GHz

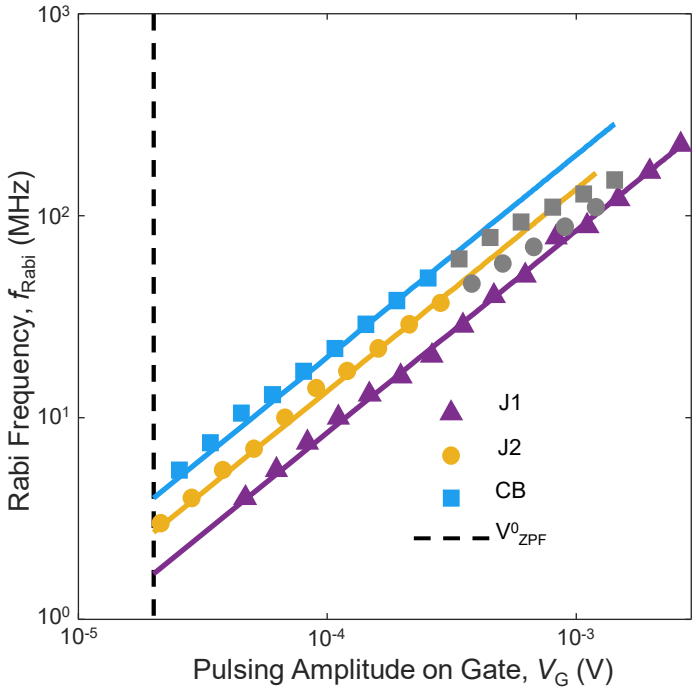

Figure 3.5: **Rabi frequency at single-photon level.** Rabi frequency as a function of microwave power applied on the CB (blue), J1 (purple), and J2 (yellow) gates. A linear fit is used to extrapolate to the single-photon level (20 μV, vertical black line). The extrapolated single-photon Rabi frequencies are shown in Table 3.1. Some data points for the CB and J2 gate fits are excluded from the fit due to a tapering effect observable at higher powers (grey).

and impedance $Z_\mathrm{r} = 2$ kΩ, this equates to 20 µV. By extrapolating the fits to this voltage for each gate, the spin-photon coupling strength $g_\perp$ calculated and listed in Table 3.1.

Driven Gate	Coupling strength, $g_\perp/2\pi$(MHz)	Resonator decay, $\kappa_\mathrm{r}/2\pi$(MHz)	Spin decoherence, $\gamma_\mathrm{s}/2\pi$(MHz)	$\frac{2g_\perp}{\gamma_\mathrm{s}+\kappa_\mathrm{r}/2}$
CB	3.98±0.15	2	1.27	3.5
J1	1.68±0.25	2	1.27	1.5
J2	2.70±0.41	2	1.27	2.4

Table 3.1: Table of spin-photon coupling parameters for each driving gate.

3.2.3 Calculating qubit decoherence, γ_s

The qubit decoherence in the system was calculated from the first and second derivatives of the qubit dispersion shown in Fig. 3.5(b), according to the following equation [141]:

$$\frac{\gamma_\mathrm{s}}{2\pi} = \frac{1}{h}\sqrt{\frac{1}{2}\left(\frac{\partial E_\mathrm{Q}}{\partial V}\right)^2 \delta V_\mathrm{noise}^2 + \frac{1}{4}\left(\frac{\partial^2 E_\mathrm{Q}}{\partial V^2}\right)^2 \delta V_\mathrm{noise}^4}\,, \tag{3.11}$$

where δV_noise is the voltage noise fluctuation of the gate due to charge noise, assumed to follow a $1/f$ distribution. This expression for spin decoherence accounts for noise up to the second order which is dominated by charge noise [142, 143]. Charge noise on the J gate is the greatest source of decoherence due to the gate's strong influence on the lateral confinement of the quantum dots [144]. δV_noise is taken to be 2 µeV at 1 Hz based on results obtained in other SiMOS devices [43]. Measurements for all three gates were taken at the same voltage relative to the degeneracy, so the decoherence is expected to be the same for all driving gates.

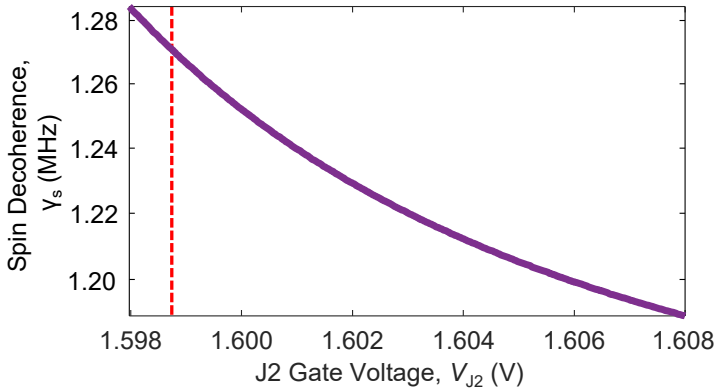

Figure 3.6: **J2 voltage dependence of spin decoherence** Spin decoherence calculated according to Eq. 3.11. Red dashed line indicates J2 gate voltage at which Rabi oscillations are measured, with $\gamma_s = 1.27$ MHz.

3.2.4 Evaluating spin-photon coupling strength

The strong spin-photon coupling regime is reached when the coupling strength $g_\perp$ between the spin qubit and the resonator exceeds both the photon decay rate κ_r and the spin decoherence rate γ_s, i.e., $g > (\kappa_\mathrm{r}, \gamma_\mathrm{s})$. In this regime, the coherent spin-photon interaction dominates the resonator decay and spin decoherence, allowing for effective information transfer between the spin and photonic modes [145].

A weaker but experimentally relevant criterion for coupling strength is the observation of vacuum Rabi splitting, when $g_\perp$ is sufficiently strong to cause an discernible splitting in the resonator's spectral response. This is fulfilled when the vacuum Rabi splitting ($2g_\perp$) exceeds the combined resonator ($\frac{\kappa_\mathrm{r}}{2}$) and spin ($\gamma_\mathrm{s}$) linewidths, namely

$$\frac{2g_{\perp}}{\gamma_{\mathrm{s}} + \kappa_{\mathrm{r}}/2} > 1. \tag{3.12}$$

Table 3.1 shows the calculated spin-photon coupling strengths and decay rates while driving on three gates. The resonator has an assumed decay rate $\kappa_{\mathrm{r}}/2\pi$ of 2 MHz, equivalent to a Q_{c} of 3000 and comparable to previous experiments with high impedance resonators on silicon substrates [118, 119, 146]. The strongest coupling is obtained with the microwave drive applied to the CB gate, due to its high lever arm caused by the gate geometry and proximity to the electron [147].

Using these criteria, the strong coupling regime is satisfied when driving on the CB and J2 gates, while the vacuum Rabi splitting should be observable driving on any of the three gates. The case for strong transverse coupling is largely contingent on the ability to fabricate a high quality resonator; given the values of $g_{\perp}$ and γ_{s} in Table 3.1, the upper bound for κ_{r} for which the vacuum Rabi splitting is observable is 13 MHz when driving on the CB gate.

3.3 Longitudinal Spin-Photon Coupling

Longitudinal spin-photon coupling describes the coupling which modulates the qubit's energy levels in proportion to the number of photons in the resonator. This section will focus on the longitudinal spin-photon coupling which arises when a qubit is operated in a "sweet-spot", a region where the Stark shift is zero ($\partial E_{\mathrm{Q}}/\partial V_{\mathrm{G}} = 0$). As a result, the qubit is first order insensitive to decoherence caused by charge noise [61, 148, 149]. In contrast to transverse coupling, the qubit and resonator are not required to be on resonance and

can be operated in the dispersive regime where $\omega_\mathrm{r} \ll \omega_\mathrm{Q}$. This reduces spin decoherence from charge noise, cavity-induced relaxation via the Purcell effect, and provides greater flexibility when tuning the qubit or the external magnetic field.

For a qubit configuration where the Zeeman splitting E_Z is comparable to the inter-orbital coupling Δ, the qubit's energy dispersion becomes non-linear between two spin-flip anticrossings. This results in a sweet-spot in the qubit dispersion E_Q, observed in the voltage range $V_\mathrm{J2} \in [1.5, 1.57]$ V in Fig. 3.7 (a). The shape of the qubit dispersion is controlled by adjusting the magnetic field strength and angle or by electrically tuning the inter-orbital tunnel coupling.

3.3.1 Dispersive and dynamic longitudinal couplings

At the sweet spot, first order longitudinal couplings such as the dispersive coupling used for gate-based readout become zero. However, since the second derivative is non-zero ($\partial^2 E_\mathrm{Q}/\partial V^2 \neq 0$), a second order dispersive coupling remains with strength [150]

$$\delta\omega = \frac{\alpha_\mathrm{r}^2}{2} \left(V_\mathrm{ZPF}^0\right)^2 \frac{\partial^2 E_\mathrm{Q}}{\partial V^2} \tag{3.13}$$

This coupling is likely too weak for strong spin-photon coupling since $\delta\omega \propto (\alpha_r V_\mathrm{ZPF}^0)^2$. However, it can be enhanced by applying a sinusoidal signal with frequency equal to ω_r to a gate, modulating the qubit energy [150]. This introduces the third term in the interaction Hamiltonian (Eq. 3.4) containing the dynamic longitudinal coupling $g_\parallel$:

$$g_{\parallel} = \frac{\alpha_{\mathrm{r}}}{2} V^{0}_{\mathrm{ZPF}} \frac{\partial^2 E_{\mathrm{Q}}}{\partial V^2} \tilde{V}_{\mathrm{m}}, \tag{3.14}$$

where $\tilde{V}_{\mathrm{m}}$ is the modulation amplitude applied to the qubit. Hence, $g_{\parallel}$ is amplified compared to the dispersive coupling $\delta\omega$ by a factor of $\tilde{V}_{\mathrm{m}}/\alpha_{\mathrm{r}} V^{0}_{\mathrm{ZPF}}$. Since the modulation frequency is on resonance with the cavity, there are other terms that are cancelled in the rotating wave approximation [146, 150] which are omitted in these calculations.

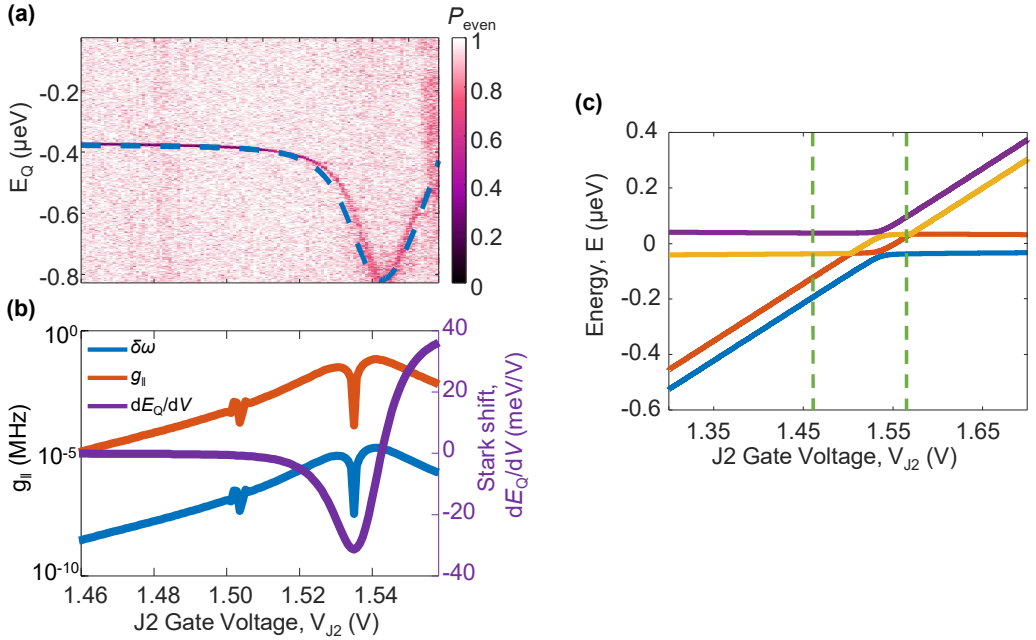

Figure 3.7: **Longitudinal coupling strengths.** **(a)** PESOS map taken at $B_0 = 620$ mT. The fitted qubit dispersion is plotted in blue. **(b)** Magnitudes of the dispersive $\delta\omega$ and dynamical longitudinal $g_{\parallel}$ for the fit in (a). The first order Stark shift is plotted in purple. **(c)** Energy diagram of the fit to the four-level model. Green dashed lines indicate the voltage region plotted in (a-b).

Figure 3.7(a) shows a PESOS map taken at a configuration which maximises the curvature of the qubit dispersion. In this setup, there is a clear sweet spot in the qubit dispersion with respect to the J2 gate voltage. There is also a

sizeable second order Stark shift which is beneficial for longitudinal coupling. The dispersive and dynamic longitudinal couplings were calculated from the fitted qubit dispersion using Eqs. 3.14 and 3.13 and are plotted in Fig. 3.7. A peak value of $g_{\parallel} = 69\,\mathrm{kHz}$ is calculated at the sweet-spot where $V_{J2} = 1.54\,\mathrm{V}$.

The tunability ratio $g_{\parallel}/2\delta\omega$ as a metric of how strong the longitudinal coupling is compared to the always-on dispersive coupling. In the voltage configuration considered in Fig. 3.7, the tunability ratio is calculated as 4000 ± 300, which is larger than previously reported for electrons in Si/SiGe [146]. This is likely due to the higher gate lever arms of the SiMOS platform and the large inter-orbital coupling of the qubit, allowing for a higher modulation amplitude. The coupling may also be turned on and off by moving the qubit in voltage space away from the ideal operation point with maximal coupling.

3.4 Discussion

This chapter has investigated the theory of spin-photon coupling and its application to electron spin qubits in SiMOS. By taking advantage of the intrinsic spin-orbit effect of SiMOS qubits, strong transverse coupling is achievable provided the fabrication and integration of a sufficiently high quality superconducting resonator comparable to those reported in previous cQED experiments. These results demonstrate that the strong coupling regime is achievable using an intrinsic spin-orbit effect for electrons on the SiMOS platform, indicating the viability of future experimental efforts in this area. However, the spin-photon coupling strength reported in Section 3.2 is lower than results for holes in SiMOS ($g_s = 330$ MHz) [33], and electrons in Si/SiGe with a micromagnet

($g_s = 21$ MHz) [120]. There are several future avenues for research which may improve the spin-photon system. The coupling strength could be improved with higher resonator impedance [59] or optimised device design for maximal gate lever arms [147]. The resonator decay rates could be improved through better filter design [107], or by utilising flip-chip bonding to separate the resonator and quantum dot chips [146]. Finally, improvements in fabrication could reduce charge noise [48], improving the spin decoherence.

It is important to note that the transverse coupling scheme is susceptible to spin relaxation due to the Purcell effect [151]. This has limited the fidelity of two qubit gates demonstrated so far [120]. This issue could be mitigated by implementing a Purcell filter [152] or by detuning the qubit from the resonator [118].

The longitudinal coupling regime examined in this chapter avoids these shortcomings since it does not require the qubit to be on resonance with the cavity. While the longitudinal coupling calculated in this chapter is not sufficient for strong coupling, there is potential to reach the strong coupling regime if resonator impedance and decay rates are improved. The curvature of the qubit dispersion could be increased through tuning of the qubit's electric confinement and magnetic field, while the modulation could also be applied to multiple gates simultaneously to increase the second order Stark shift. The dynamic longitudinal coupling also has potential applications in qubit readout [153].

Chapter 4

Fabrication and characterisation of superconducting resonators

The silicon MOS fabrication process imposes certain restrictions on the materials and methods available when integrating an on-chip superconducting resonator. This chapter details progress in fabrication and experiment towards making a hybrid qubit-resonator device. While resonator and quantum dots were individually demonstrated, an integrated device with both working components was not realised. Nonetheless, the methods and results in this chapter represent a step towards achieving spin-photon coupling for electrons in SiMOS.

4.1 High impedance resonators

As detailed in Section 3.2, the spin-photon coupling strength of a hybrid qubit-resonator is directly proportional to the zero-point voltage fluctuation of the

resonator V^0_{ZPF}, which in turn is proportional to the square root of the resonator impedance:

$$g_\perp \propto V^0_{\mathrm{ZPF}} \propto \sqrt{Z_{\mathrm{r}}}. \tag{4.1}$$

The impedance of the resonator is given by

$$Z_{\mathrm{r}} = \sqrt{\frac{L}{C}}. \tag{4.2}$$

Therefore, it is desirable to maximise the inductance and minimise the capacitance of the superconducting resonator. The simplest way to do this is to maximise the geometric impedance of the resonator by reducing the centre conductor width and increasing its separation from the ground plane. This approach was sufficient for a demonstration of strong spin-photon coupling in Si/SiGe, which used a Niobium resonator (chosen for its magnetic field resilience) [30].

However, even greater impedances are possible by choosing superconducting materials which exhibit a property known as kinetic inductance. MoRe is one such material, making it an interesting candidate for superconducting resonator fabrication.

4.1.1 Experimental Setup

The characterisation of resonators requires cryogenic setups capable of cooling to temperatures below the superconducting transition of the resonator material. Most experiments reported in this chapter were performed in a dilution refrigerator capable of cooling to a base temperature of 50 mK (Fig. 4.1). The microwave lines inside the fridge are superconducting NbTi wires. A total of

50 dB of attenuation is applied throughout the microwave line to eliminate Johnson-Nyquist noise from higher temperature stages. Two cryogenic circulators are used to isolate thermal noise on the output line. The circuit topology is changed depending on whether the reflection or transmission of the resonator is measured. At the 4 K stage, a high-electron-mobility transistor (HEMT) is used to amplify the output signal, with a nominal gain of 37 dB. The microwave signal is generated and read by a vector network analyser (VNA).

The molybdenum rhenium (MoRe) notch resonators (Sec. 4.1.4) were measured in an ICEoxford VTI cryostat capable of reaching temperatures of 300 mK. The experimental setup was the same as described in Figure 4.1, except for the removal of one circulator and the absence of a 1 K stage.

4.1.2 Notch resonator design

To characterise the resonator fabrication process and materials, a simple notch resonator layout was designed (Fig. 4.2 (a)). The device consists of six resonators of different lengths coupled to a transmission line. The resonant frequencies are separated by at least 0.5 GHz and are designed to have a coupling q-factor of 10,000, with the exception of resonator 4 (at 7 GHz), which has a coupling q-factor of 1,500. This allows for the identification of individual resonators even when the resonant frequencies deviate from simulations for high kinetic inductance materials. Flux pinning sites were added to the design to improve magnetic field resilience (Fig. 4.2 (b)). The quality factors of all resonators were extracted from their frequency and phase responses by the circle fit method described in Ref. [154].

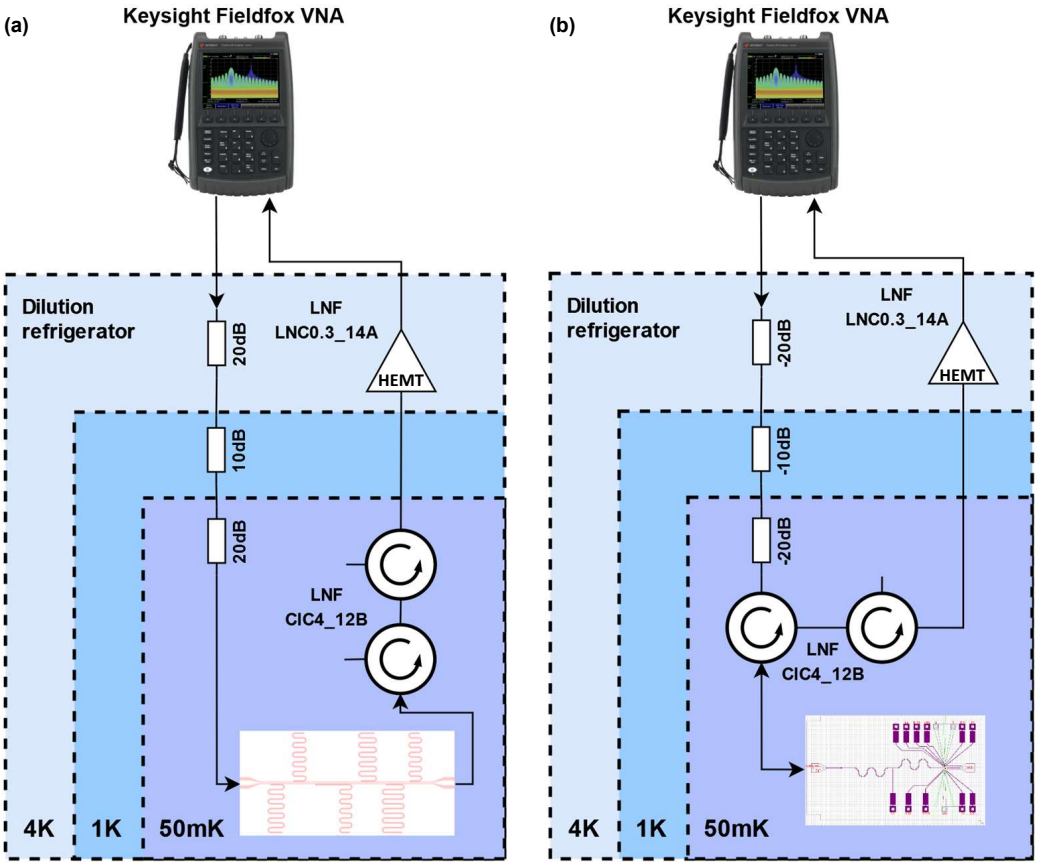

Figure 4.1: **Fridge diagram and experimental setup for resonator experiments.** **(a)** Fridge diagram of transmission-style measurements for the notch resonator device. **(b)** Fridge diagram of reflection-style measurements for the hybrid spin-photon device.

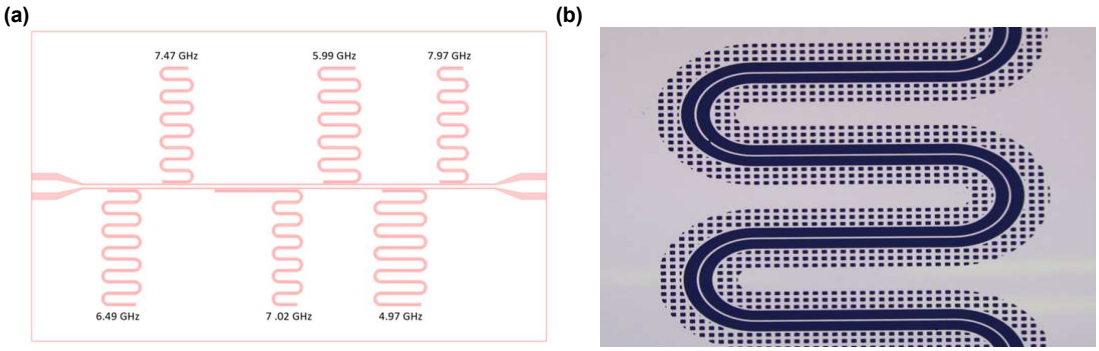

Figure 4.2: **Notch resonator design (a)** Mask design of the notch resonator device with labeled resonant frequencies as simulated in Sonnet EM. **(b)** Microscope photo of resonator showing flux pinning sites.

4.1.3 Oxide thickness and resonator quality

In silicon MOS devices, a layer of silicon oxide (SiO_2) is fabricated between gate and substrate. This oxide is grown with a process called thermal oxidation, which is typically 8 nm thick in the active region of devices studied here (Fig. 4.3 (b)). Outside of this region, the oxide thickness is increased to 100-200 nm to ensure electric isolation between metal and substrate after wire bonding. The resonator sits on this thick oxide layer, which is a potential source of two-level systems (TLS) causing photon loss in the resonator.

To test the effect of the oxide layer thickness on resonator quality factor, two aluminium notch resonator devices were fabricated on thermally grown high-quality ultra dry oxide (UDOX) layers with thicknesses of 8 nm and 110 nm. Table 4.1 shows the measured quality factors of the notch resonators, fitted from the resonator phase and magnitude responses with the circle fit technique [154]. The Q_c values are generally in good agreement with simulation, while there is no clear trend in quality factor between the two oxide thicknesses. This indicates that the thermally grown oxide layer is not a significant source of dielectric loss

in the resonator.

Oxide thickness		**Res. 1** 5 GHz	**Res. 2** 6 GHz	**Res. 3** 6.5 GHz	**Res. 4** 7 GHz	**Res. 5** 7.5 GHz	**Res. 6** 8 GHz
110 nm	$Q_c/10^3$	9.0	9.5	13.0	2.4	7.9	6.1
	$Q_i/10^3$	20.9	25.4	28.6	17.1	24.1	9.4
8 nm	$Q_c/10^3$	5.0	6.7	8.2	1.9	9.5	9.9
	$Q_i/10^3$	27.4	25.1	22.4	24.4	23.1	13.4

Table 4.1: Table of quality factors of notch resonator device for different oxide thickness.

4.1.4 Molybdenum rhenium resonators

Molybdenum rhenium (MoRe) is a promising material for superconducting resonators owing to its high superconducting transition temperature, magnetic field resilience and kinetic inductance [114]. In addition, MoRe resonators have been shown to be capable of withstanding the high temperatures of the annealing process of silicon MOS processes [115], unlike other common superconducting materials such as NbTiN. MoRe is sputtered without the presence of nitrogen or oxygen gas, making it less prone to variability between resonator batches. Because etching the metal layer is detrimental to the quantum dot fabrication quality, a lift-off process is used to pattern the resonator. Since the sputtering process results in a conformal deposition, lift-off for sputtered films can only be used if the deposited film thickness is much thinner than the photoresist thickness (typically $\sim 2\ \mu m$ for nLOF2020).

The MoRe resonators measured here are made from a 60/40 MoRe alloy, similar to previous experiments in Refs. [114, 155], and are deposited on a high-resistivity silicon substrate with a film thickness of approximately 20 nm (Ap-

pendix B). The device was measured in the VTI at a temperature of around 300 mK. Table 4.2 shows the measured quality factors of the MoRe notch resonators. Only four resonances were observed, with significant shifts in resonant frequency from simulation attributable to the presence of kinetic inductance. Therefore, the reason for the absence of resonator 1 is likely due to its resonant frequency being shifted outside the operating frequency range of the circulator and cryo-amp. Resonator 5 was observed to have a break due to a fabrication defect, so its resonance could not be measured. The quality factor results are comparable to the aluminium notch resonators and validate lift-off patterned MoRe as a suitable material for high impedance superconducting resonators.

	Res. 1	**Res. 2**	**Res. 3**	**Res. 4**	**Res. 5**	**Res. 6**
f_r(**GHz**)	-	4.67	5.03	5.48	-	6.19
$Q_\mathrm{c}/10^3$	-	6.5	6.1	2.2	-	11
$Q_\mathrm{i}/10^3$	-	28	17	35	-	21

Table 4.2: Table of quality factors for MoRe notch resonators.

4.2 Integrating resonators with quantum dot devices

4.2.1 Hybrid device fabrication

The successful integration of a resonator on the same chip as a SiMOS quantum dot presents several fabrication challenges. The two devices are on completely different size scales: the resonator is typically millimetres long while the quantum dot gates are tens of nanometres wide. As a result, electron beam lithography is too time consuming to pattern resonators, while the resolution of optical

lithography is not sufficient for quantum dots. Two separate lithography steps are therefore required for the fabricaton of a hybrid device.

This raises a dilemma of which component should be fabricated first. Fabricating the resonator first places a limitation on the resonator material, since the resonator must be able to survive a forming gas anneal without quality factor degradation. Conversely, fabricating the quantum dot first precludes the use of etching to pattern the resonator; the highly reactive chemicals used to etch the metal layer introduce impurities into the gate and oxide layers of the quantum dot device which are detrimental to qubit coherence. For the device measured in this section, the quantum dot gate layers are deposited and annealed before the resonator is fabricated.

Aluminium forms an insulating native oxide upon exposure to air which must be removed before making a connection between the optical and EBL metal layers. One method of making a galvanic connection between the optically-defined and EBL-defined regions is to use metal patches which overlap both layers at their junction (Fig. 4.3 (b)). The native oxide is removed with an ion milling process before the patch is deposited without breaking vacuum (Appendix B).

The hybrid device was developed before a high-impedance material fabrication process was finalised. As a result, the resonator is made of aluminium and is not expected to exhibit any kinetic inductance.

4.2.2 Hybrid device design

Figure 4.3 (a) shows an SEM image of the double quantum dot device. The device is similar to that measured in Section 3.2, with an SET used for readout while a nearby antenna can drive qubits with ESR. The gate oxide thickness is 8 nm in the active region (Fig. 4.3 (b), in green), which slopes up to a oxide thickness of 200 nm across the rest of the chip. The thicker oxide isolates the metal gates from the substrate, ensuring that a 2DEG is not formed outside the active region.

The CPW $\lambda/2$ resonator is designed to have a resonant frequency $f_r = 6$ GHz, with a coupling quality factor of 3,000. The resonator has a centre pin width of 5 µm and a ground plane separation of 25 µm. This corresponds to an impedance of 91 Ω in the absence of any kinetic inductance. The centre pin of the resonator is connected to the P2 gate; to bias the voltage of the P2 gate, a DC tap is connected to the voltage node of the resonator.

LC low-pass filters are fabricated on every gate electrode to filter microwave leakage from the capacitive coupling of the resonator to nearby gates [107,156]. The filters consist of a planar spiral inductor and finger capacitor and are designed with a cutoff frequency of 1 GHz.

4.2.3 Device characterisation

The hybrid device was measured in the cryogenic setup described in Section 4.1.1 with a base temperature of 50 mK. Figure 4.4 (a) shows the wideband magnitude response of the hybrid device. Two resonances are visible at 6

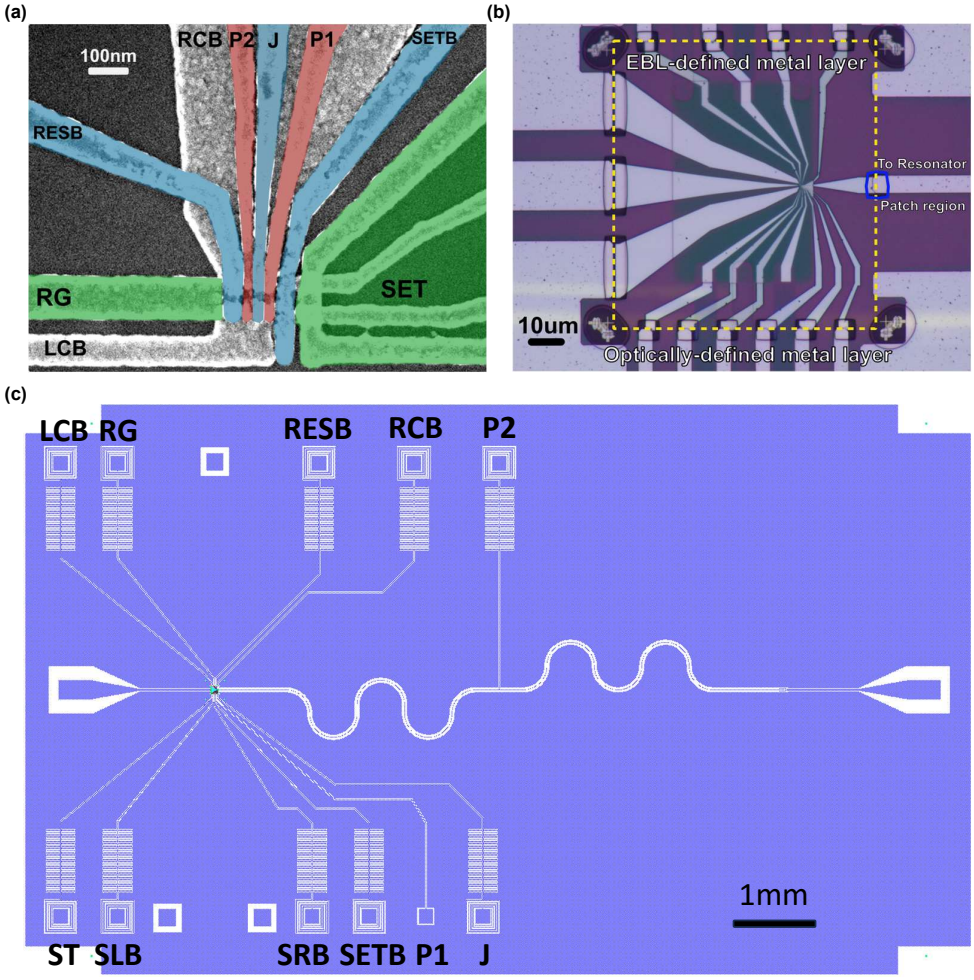

Figure 4.3: **Hybrid device design (a)** False-coloured SEM image of the quantum dot device. **(b)** Microscope photo of device showing EBL-defined and optically-defined metal layers. The yellow dotted line denotes the boundary of the two metal layers. The patch regions are indicated by the rectangular regions at each junction where the photoresist is etched away (example outlined in blue). The dark green region is the active area, where the gate oxide is 8 nm thick. **(c)** Mask design of hybrid device. In this design, the resonator is connected to the P2 gate.

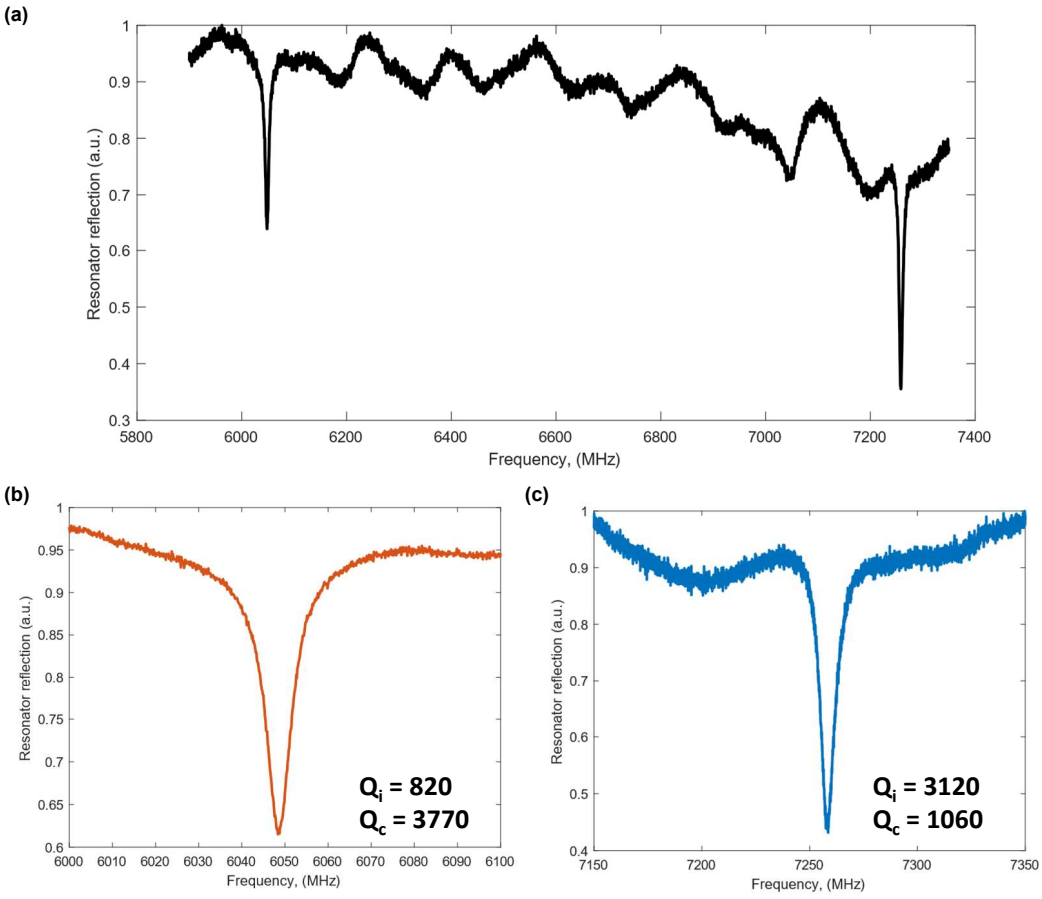

Figure 4.4: **Hybrid device frequency response (a)** Wideband reflection measurement of the hybrid resonator-dot device. **(b)** Magnitude response of the 6 GHz resonance. **(c)** Magnitude response of 7.2 GHz resonance.

GHz and 7.2 GHz respectively (Fig. 4.4 (b,c)). To verify that the resonance originates from the aluminium resonator, the magnetic field is swept until the resonance disappears (Fig. 4.5 (a)). The critical field is found to be 20 mT, in agreement with the literature [157, 158]. A rough temperature sweep is also conducted by collecting the ^{3}He–^{4}He mixture in the dilution fridge, warming it to 4 K while probing the resonator. A critical temperature between 0.9 K and 1.3 K was measured (Fig. 4.5 (c)), similar to previously reported values for aluminium thin films [159]. The 6 GHz resonance is almost certainly the $\lambda/2$ resonator, since the resonant frequency and coupling q-factor are consistent with simulation. The resonator is undercoupled, with an internal quality factor $Q_\mathrm{i} = 820$ much lower than previous experiments on notch resonators (Tab. 4.1) indicating a significant loss mechanism introduced by the integration of the quantum dot.

There are several potential causes of the drop in quality factor of the hybrid device. The resonator is galvanically connected to the P2 gate which overlaps considerably with nearby gates, especially the lateral confinement gate RCB (Fig. 4.3). This could be a considerable source of leakage which is not sufficiently filtered by the LC circuit. In a strong spin-photon coupling demonstration for hole qubits in SiMOS, Yu et al. (2022) reported a Q_i of 530 despite the use of LC filters on all DC lines [33]. The hybrid device also has several n-type ohmic regions doped with phosphorus atoms which form a conducting channel for the SET and electron reservoir. These ohmic regions could be another source of microwave leakage.

The origin of the resonance at 7.2 GHz is unknown: both resonances have the same critical field and temperature, signifying that they originate from an

aluminium superconducting resonator. Possible candidates for the additional peak include a resonance in the bond wires, a resonance in the DC tap, or slotline modes [160]. The internal quality factor of the extra resonance is notably higher than the main resonance: this is further evidence the drop in Q_i is caused by proximity to the quantum dot.

4.3 Discussion

The results presented in this chapter show the fabrication and characterisation of superconducting resonators for use in spin-photon coupling experiments. MoRe was investigated as a material for high-impedance resonators with internal quality factors exceeding 10^4. The Al resonator of a hybrid device was measured, yielding a Q_i of approximately 800. These results represent a significant step towards the integration of a superconducting resonator with SiMOS quantum dot devices. However, a demonstration of spin-photon coupling was ultimately not achieved within the duration of this thesis due to issues in fabrication process development and poor lithography yield. Future directions of research include improvements to the resonator quality factor and experiments on a device with both qubits and high-impedance resonator working concurrently.

The resonator quality factor could be improved by changing the gate design to minimise capacitive coupling between gates. For example, the RCB gate could be made smaller to reduce the overlap with the P2 gate. The resonator could also be connected to other gates with larger gate separation such as the LCB gate. The surface area of the ohmic regions could also be reduced

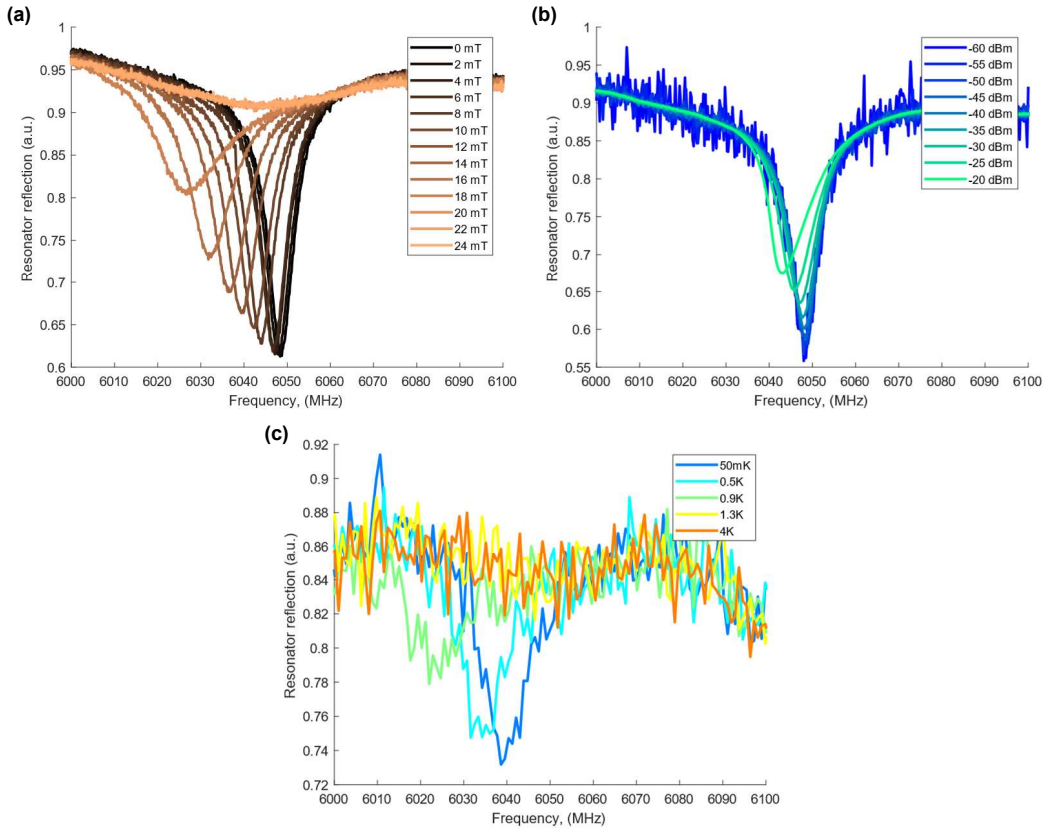

Figure 4.5: **Magnetic field, microwave power and temperature sweeps of hybrid device resonator.** **(a)** Magnitude response of the resonator for varying external magnetic field strengths. **(b)** Magnitude response of the resonator for varying input microwave power (at the source). **(c)** Magnitude response of the resonator for varying temperature at an input power of -40 dBm.

to mitigate microwave leakage. The filter design could be improved further by using second-order low-pass or band-stop filters to increase the stopband attenuation. Materials with high kinetic inductance could be used to fabricate compact nanowire inductors [107].

Many of the fabrication constraints described in Section 4.2.1 could be removed if the resonator and qubit are fabricated on different chips. Flip-chip bonding could be used to make a low-resistance galvanic connection to the resonator [161].

Recent developments in granular aluminium (grAl) films have demonstrated kinetic inductances far larger than other high-impedance materials [59, 111]. The biggest challenge when working with grAl is the variability between thin films: careful control of all deposition parameters is required. If these fabrication challenges can be overcome, the spin-photon coupling strength could be improved considerably.

Chapter 5

Control and benchmarking of qubits dressed in a global field

Individually addressing and controlling many qubits presents a challenge in scalability due to qubit crosstalk, heat load, and the hardware complexity of frequency multiplexing. One possible solution utilises a dielectric resonator to provide a uniform driving field for global qubit control. By dressing the qubits in an on-resonance global field, all qubits can be driven simultaneously with a single microwave source. This chapter demonstrates control of electron spin qubits in silicon driven by a dielectric resonator.

5.1 Experimental Setup

The device under test is a three-dot device with an adjacent single electron transistor (SET) (Fig. 5.1), similar to the device measured in Chapter 3 and

devices in Refs. [18, 32, 43]. The P and J gates shape the electric potential of the quantum dots and confine the electron spin qubits. The reservoir gate (RG) is used to induce a two-dimensional electron gas (2DEG) which acts as an electron reservoir to load electrons into the quantum dots. The SET consists of a top gate for 2DEG accumulation and two barrier gates for confinement. The reservoir barrier (RESB) and SET barrier (SETB) gates are usually kept at a high potential to isolate the qubit quantum dots from the SET and reservoir.

The distinguishing feature of this device is the addition of a potassium tantalate ($KTaO_3$) dielectric resonator used to provide the global microwave field. The resonator sits on top of a 0.2 mm sapphire spacer that prevents stray electric fields at the resonator's boundary from affecting qubit operation (Fig. 5.1(a,d)).

All measurements are performed in a wet dilution refrigerator capable of cooling to base temperatures around 50 mK (Fig.5.2). The global driving field is provided by a Keysight PSG8267D vector signal generator, which is connected to a loop coupler directly above the dielectric resonator (Fig. 5.1 (d)). The microwave source's internal mixer is used for I/Q modulation, while I/Q signals are produced with a Quantum Machines OPX. DC gate voltages are biased with a combination of SIM928 isolated voltage sources and Basel LNHR digital-to-analog converters (DAC). The OPX is used to generate high frequency pulses for the P,J and SET top gates.

The device is operated in the $(4,0) \leftrightarrow (3,1)$ charge regime under the (P2,P3) gates. Parity readout is performed using Pauli spin blockade (PSB) for spin-to-charge conversion [70], while charge transport is detected with the single electron transistor (SET). The SET source-to-drain current signal is read with the OPX after amplification with a Basel SP983c I-to-V converter.

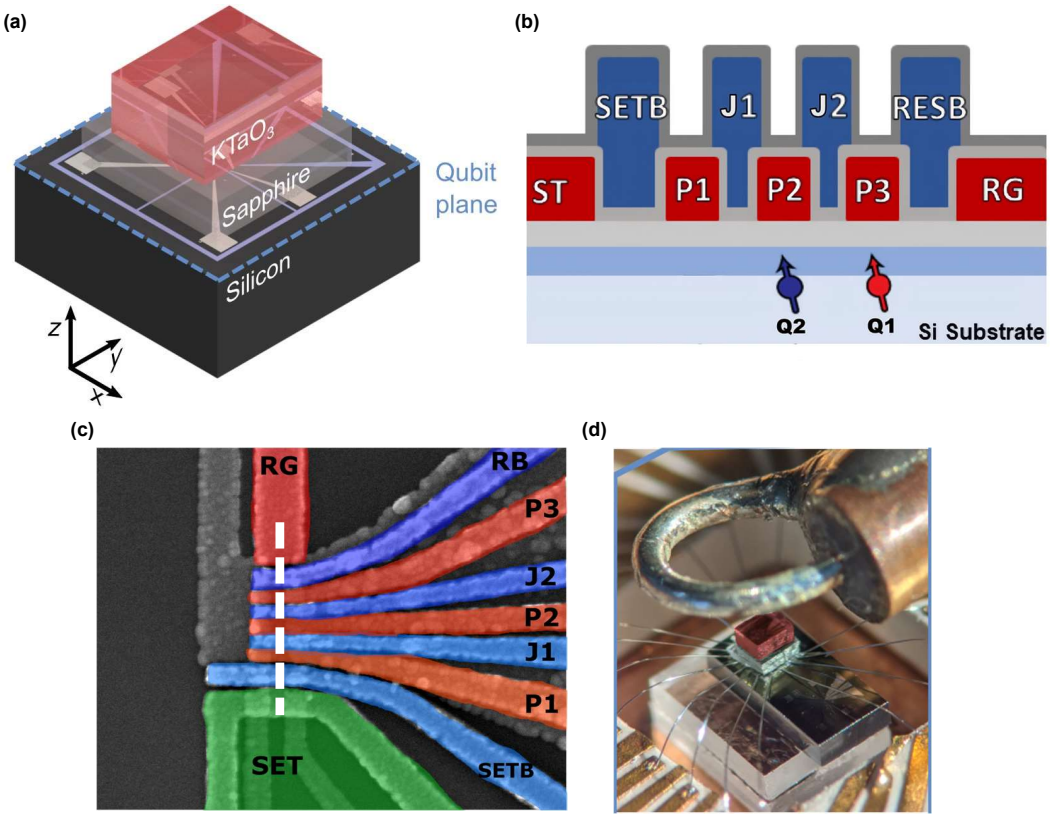

Figure 5.1: **Dielectric device design**. **(a)** 3D illustration of the silicon qubit chip with a dielectric resonator placed on top. **(b)** Cross-section diagram of the silicon device. **(c)** False-coloured SEM image. The white dashed line indicates the cross section depicted in (b). **(d)** Photo of the device showing loop coupler, dielectric resonator and silicon chip.

An external magnetic field of around 0.25 T applies a Zeeman splitting equal to the dielectric resonator's resonant frequency. The magnetic field is oriented along the (110) crystallographic axis of the silicon substrate. There is an approximate 25 MHz difference in Larmor frequency between the two qubits, attributable to g-factor variance caused by the spin-orbit interaction [32, 162].

The qubits are numbered sequentially according to their Larmor frequency: qubit 1 refers to the electron under the P3 gate, while qubit 2 is located under P2. Experiments are performed on the qubits individually, which are tuned into resonance with the dielectric resonator by changing the magnetic field strength.

5.2 Coherent control with a dielectric resonator

Previous dielectric resonator experiments demonstrated spin resonance [35] and coherent control [36] of electron spin qubits in silicon. However, the coherence times of these devices were limited by the use of palladium for the gate material, likely due its low charge mobility compared to aluminium and the atomic layer deposited (ALD) inter-gate oxide layer [163]. The results presented in this chapter are performed on a device with an aluminium gate stack. Figures 5.3 (a) and (b) show the plot distinctive to these devices: the enhancement of the qubit's Rabi frequency as it is brought into resonance with the dielectric resonator (black dashed line). The dielectric resonator has a resonant frequency of 6.713 GHz with an internal quality factor of $Q_\mathrm{i} = 900$. The resonator is almost exactly critically coupled, with a loaded quality factor of $Q_\mathrm{i} = 450$. Qubit 1 has a significantly higher Rabi frequency than qubit 2, suggesting the presence of an intrinsic spin-orbit effect which is driven electrically by the

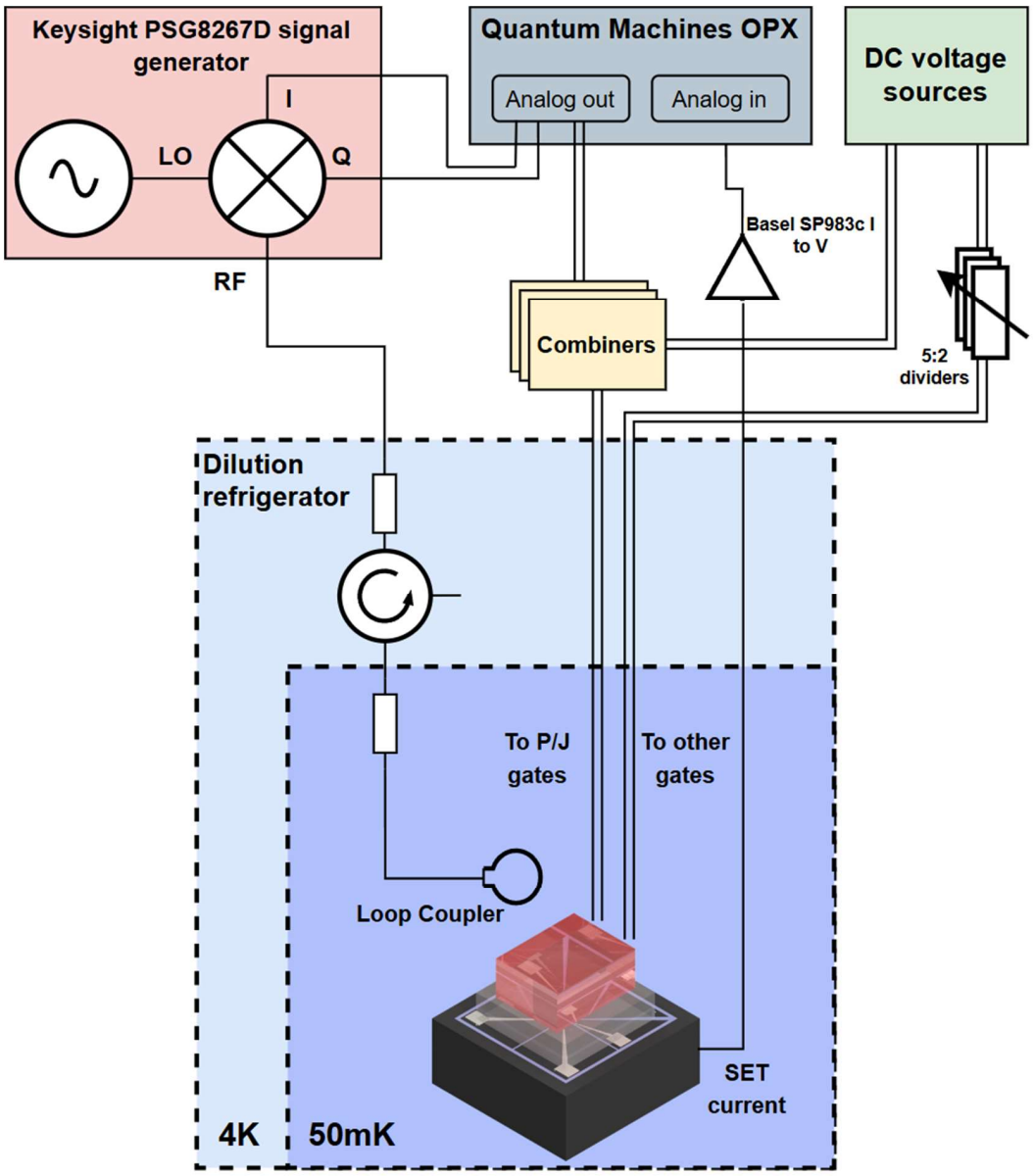

Figure 5.2: **Experimental setup.**

resonator. This is supported by the asymmetry in the Rabi enhancement plots which arises from the anisotropic spin-orbit interaction [32].

Figure 5.3 shows the Rabi, Ramsey and Hahn coherence times of both qubits. $T_{2,\mathrm{Rabi}}$ for both qubits exceeded 70 μs (Fig. 5.3 (c,d)), while T_2^* and $T_{2,\mathrm{Hahn}}$ were on the order of 10 μs and 100 μs respectively (Fig. 5.3 (e-h)). These results are comparable to experiments performed on similar Al devices on isotopically purified SiMOS [43, 164]. Therefore, the dominant source of decoherence of previous global control experiments can be attributed to the Pd-ALD gate stack and not to the dielectric resonator itself.

5.3 Two-axis control of driven qubits

The original Kane quantum computer proposal used an off-resonant always-on global magnetic field. To perform qubit operations, the qubits are electrically tuned into resonance with the global field via the Stark effect [38, 121]. Hence, in practical quantum algorithms, qubits spend the majority of the time idling out of resonance with the global field. However, from the coherence times in Fig. 5.3, it is evident that qubits suffer from much greater decoherence off resonance, namely:

$$T_2^* \ll T_{2,\mathrm{Rabi}}. \tag{5.1}$$

Therefore, for globally driven qubit arrays it is advantageous for qubits to be always on-resonance, or *dressed*, with the driving field. Dressed qubits

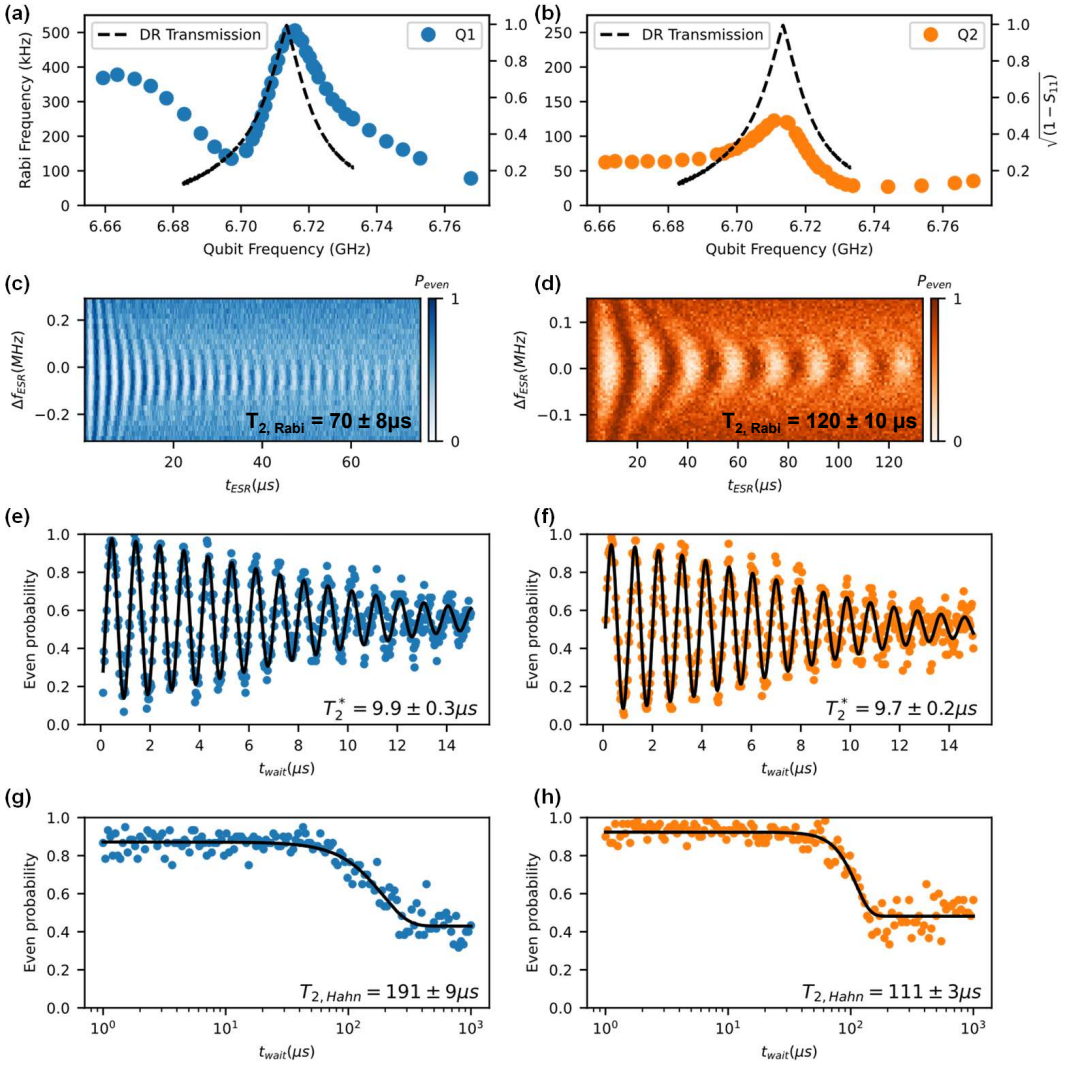

Figure 5.3: **Rabi enhancement and coherence of qubits driven with a dielectric resonator.** **(a-b)** Rabi frequency as a function of qubit frequency. Resonator frequency response is overlaid in black. **(c-d)** Rabi chevrons for qubits 1 (c) and 2 (d). **(e-f)** Ramsey oscillations. **(g-h)** Hahn echo experiment results.

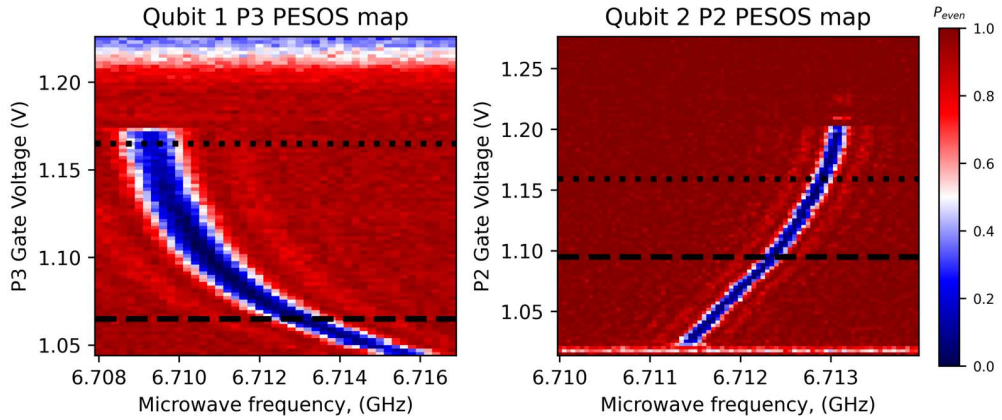

Figure 5.4: **Stark shifts for dressed qubit control.** Qubit even state probability when a microwave of fixed amplitude and duration is applied with varying frequency and plunger gate voltage. The qubit frequency changes with gate voltage due to the Stark effect. Dashed (dotted) lines indicate voltage control points for Dressed FM and SMART (Dressed FSK) qubits.

have been demonstrated on a variety of platforms including superconducting qubits [165], donor-bound electrons in silicon [121,122], and electrons in silicon quantum dots [166].

Single qubit control is achieved by pulsing gate voltages to modulate the qubit frequency via the Stark effect. Figure 5.4 shows PESOS maps (introduced in Sec. 3.1.3) of the qubits when sweeping the voltage of the plunger gates directly above the spin. Stark shifts of up to 7 MHz and 2 MHz are observed on qubits 1 and 2 respectively. Several driven qubit schemes are possible with different Stark shift and global field modulation signals [123,124].

In the dressed regime, the qubit's spin states are hybridised with the external field. Therefore it is more convenient to transform to the dressed basis $\{|X_\rho\rangle, |Y_\rho\rangle, |Z_\rho\rangle\}$, in which the qubit's logical states correspond to the new quantisation axis of the dressed qubit (Fig. 5.5). This is equivalent to a

Hadamard transformation, effectively swapping the X and Z axes on the Bloch sphere ($X \rightarrow Z_\rho, X \rightarrow X_\rho, Y \rightarrow -Y_\rho$) [123]. A more detailed derivation of the dressed basis is contained in Appendix A, and all qubit states in this section are described in the dressed basis unless otherwise specified.

5.3.1 Dressed qubits

The most straightforward method of dressed control is frequency-shift keying (FSK), in which the frequency of a qubit is "keyed" between discrete values while driving with a continuous wave (CW) global field (Fig. 5.6 (a,d)). The signal applied to the gate voltage is essentially a square pulse with amplitude large enough to induce a detuning Δ between the qubit and driving field. For the ideal case where $\Delta \gg \Omega_\mathrm{R}$, a rotation of angle α is performed by choosing the duration of the FSK pulse T_FSK according to the equation

$$\frac{\alpha}{2\pi} = \Delta T_\mathrm{FSK}. \tag{5.2}$$

However if $\Delta \sim \Omega_\mathrm{R}$, the Stark shift is not sufficient to bring the qubit completely out of resonance with the global field. The resulting oscillations have frequency

$$f = \sqrt{\Delta^2 + \Omega_\mathrm{R}^2} \tag{5.3}$$

around a rotation axis with polar angle on the Bloch sphere

$$\theta = \tan^{-1}(\frac{\Delta}{\Omega_\mathrm{R}}). \tag{5.4}$$

This is analogous to Rabi oscillations in the bare basis with non-zero detuning. As a result, large detunings relative to the Rabi frequency are desirable for dressed FSK qubits.

In experiment, the qubits were tuned to a regime optimal for dressed FSK gates. The plunger gate voltages are chosen close to the charge transition to maximise the available Δ (Fig. 5.4). The Stark shift of both qubits is non-linear; therefore, control points with lower first-order Stark shift ($\frac{\partial f_Q}{\partial V}$) are chosen to minimise the effect of charge noise coupling to the qubit through the plunger gate [144]. An experimental demonstration of dressed FSK oscillations in qubit 1 is shown in Fig. 5.6(g). These results are measured at the lowest Rabi frequency while still preserving qubit coherence. This ensures the condition $\Delta = 7$ MHz $\gg \Omega_R = 0.37$ MHz is satisfied.

Alternatively, dressed qubits can be controlled with sinusoidal modulations on the qubit frequency, an approach termed frequency modulation (FM) (Fig. 5.6(e)). In contrast to FSK, the FM control scheme does not benefit from maximal Stark shifts since for large modulation amplitudes where $\Delta > \Omega_R$, Bloch-Siegert shifts arise from the breakdown of the rotating wave approximation [167]. This makes it more suitable for a large-scale global control scheme where the Stark shift is small. It is desirable to bias to a control point with linear Stark shift to minimise distortions in the sinusoidal modulation of the qubit dispersion (Fig. 5.4).

Two-axis control is achieved in dressed control schemes by shifting the phase of the Stark shift signal relative to the qubit's precession about the dressed Z-axis at the Rabi frequency (Fig. 5.5). For dressed FSK qubits, adding a $\frac{3\pi}{2}$ ($\frac{\pi}{2}$) phase delay results in rotation around the Y (-Y) axis. Similarly, for dressed FM qubits X (Y) rotations are achieved by applying negative cosine (sine) signals to the gate.

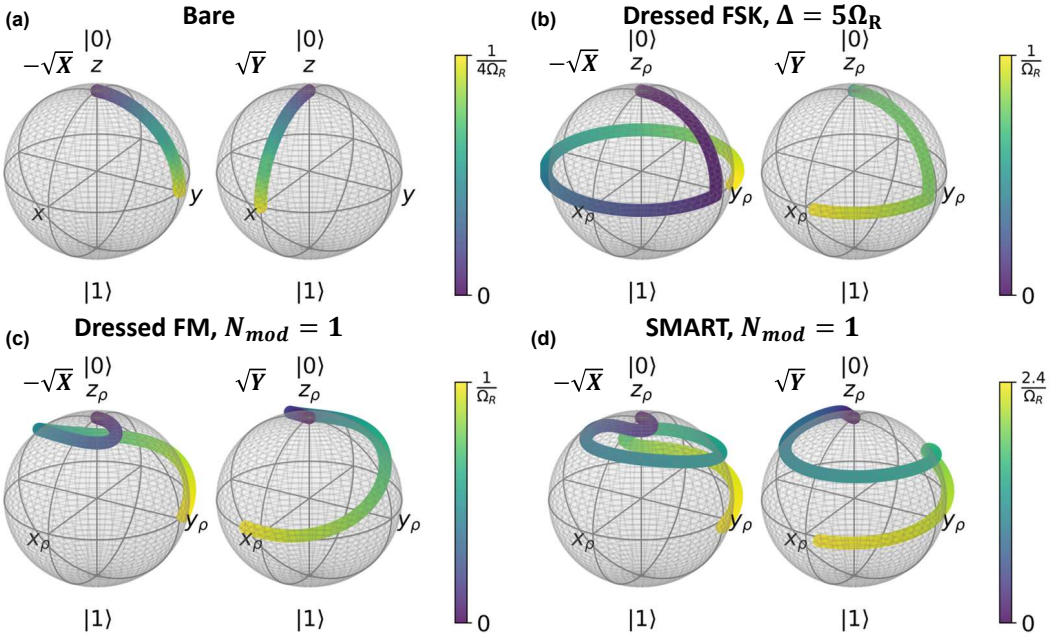

Figure 5.5: **Bloch sphere visualisations of (a) bare, (b) dressed FSK, (c) dressed FM and (d) SMART gates.** The qubit state is simulated as a function of time for a $\pi/2$ gate around the X and Y axes. The bare gates take a quarter of the Rabi period, while the dressed and SMART gates take 1 and 2.4 periods respectively. Note the change in basis between the bare and dressed qubits.

5.3.2 SMART qubits

The key benefit of dressed control is the protection it provides from environmental noise, improving qubit coherence. However, dressed qubits have limitations in their ability to suppress noise. The dynamical decoupling of the dressed qubit is only effective if the noise's time correlations are longer than the Rabi period; higher-frequency noise, especially near the Rabi frequency, still affects the qubit's coherence. Additionally, variations in the qubit's Rabi frequency are particularly detrimental to dressed qubit coherence. This is especially important in the context of large scalable qubit arrays, where fluctuations in qubit Larmor and Rabi frequencies from fabrication variations are expected.

The SMART (sinusoidally modulated, always rotating, and tailored) protocol addresses these limitations by introducing a sinusoidal modulation to the amplitude of the global field (Fig. 5.6 (c,f)). A detailed explanation of the noise decoupling properties of the SMART protocol described using the geometric formalism [168] can be found in Ref. [124]. SMART qubits have been previously demonstrated in nitrogen-vacancy centres [169] and on the SiMOS platform using an on-chip ESR antenna to provide the global drive [85, 166]. The results in this chapter are the first implementation of SMART qubits driven with the global field of a dielectric resonator.

Two-axis control of SMART qubits is more complicated than the dressed case: in addition to phase shifts, higher frequency harmonics are added to the qubit modulation. All SMART experiments in this chapter use the simplest implementation: for a modulated driving field

$$A_{\mathrm{MW}}(t) = h\frac{\Omega_{\mathrm{R}}}{\sqrt{2}}\cos(2\pi f_{\mathrm{mod}}t), \tag{5.5}$$

X and Y rotations are performed with the following signals applied to the detuning (Fig. 5.5:

$$\Delta_X(t) \propto \cos(4\pi f_{\text{mod}} t), \tag{5.6}$$

$$\Delta_Y(t) \propto \sin(2\pi f_{\text{mod}} t). \tag{5.7}$$

Here f_{mod} is chosen such that $f_{\text{mod}}/\Omega_{\text{R}} = j_1$, where $j_{0,1} \approx 2.4048$ is the 1st zero of J_0, the zeroth-order Bessel function of the first kind. This value of f_{mod} cancels quasi-static noise up to the second order [124].

5.4 Gate Set Tomography

To benchmark the fidelity of bare, dressed and SMART qubits, single qubit gate set tomography (GST) experiments were conducted. GST sequence generation and results analysis was implemented with the pyGSTi software package [170]. For bare qubit GST sequences, germ lengths up to L=256 were used, while the maximum dressed and SMART germ length was L=64. The gate set consists of the $X_{\frac{\pi}{2}}$, $Y_{\frac{\pi}{2}}$ and I gates, and a CPTP (completely positive trace preserving) gate set model is used.

5.4.1 GST infidelity sources

One of the advantages of GST analysis is its ability to decompose error generators around each axis and separate Hamiltonian and stochastic errors. However, the exact composition of these errors depends on the gauge fixing of the GST

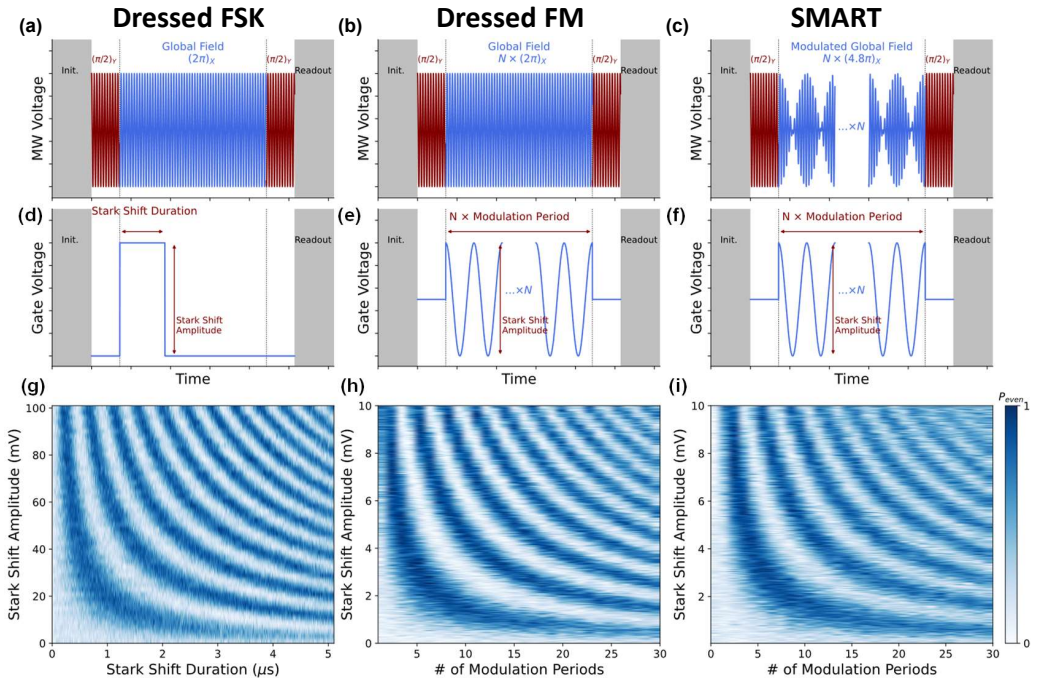

Figure 5.6: **Driven gate pulse sequences. (a-c)** Applied Microwave drive signal for each driven qubit scheme. $\pi/2$ projection pulses (red) are applied to transform into the dressed basis before and after the control sequence (blue). **(d-f)** Voltage waveforms applied to the plunger gate for each driven qubit scheme. A square pulse is used for the Dressed FSK scheme, while sinusoidal pulses are used for Dressed FM and SMART qubits. **(g-i)** Even parity readout probability as a function of applied Stark shift and modulation time. Coherent oscillations are observed for each of the three driven qubit schemes.

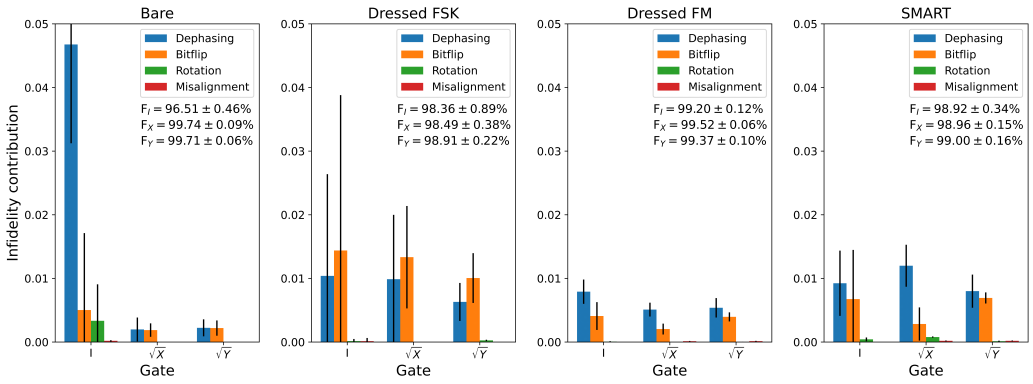

Figure 5.7: **GST fidelity and FOGI quantity comparison across bare and driven qubits.** Error bars indicate 95% confidence intervals. Rotation and misalignment errors are plotted but are too small to be visible for most gates.

analysis program, which can be independent of experiment and varies between GST runs. To this end, errors are classified into first-order gauge invariant (FOGI) quantities. As the name suggests, FOGIs are independent of gauge transformations and can be used to compare error rates between GST experiments [171]. Using FOGIs also presents the errors in a manner more intuitively relatable to physical sources of error in the qubit system. The FOGIs for single qubit GST are listed in Table 5.1.

The average gate infidelity $\bar{\epsilon}$ is calculated for single-qubit gates from the sum of Hamiltonian (H_i) and stochastic (S_i) errors:

$$\bar{\epsilon} = \frac{2}{3}(\sum_i S_i + \sum_i H_i^2) \tag{5.8}$$

for axis $i \in \{X, Y, Z\}$.

Figure 5.7 shows the gate fidelities and error composition of bare, dressed and SMART qubits driven with a dielectric resonator. Bare $\sqrt{X}$ and $\sqrt{Y}$ gate fidelities exceed 99.7%, all dressed frequency modulated gates exceed 99%

fidelity, and SMART gates are just under 99%. Surprisingly, the dressed and SMART X and Y gates have lower fidelities than bare gates. Since the dressed and SMART gates are 4 and 9.6 times longer than bare gates respectively, this suggests there is a decoherence mechanism acting on the qubits for a longer period which is not adequately decoupled by the dressed or SMART fields. Identifying the physical source of this noise is the primary motivation for the noise spectroscopy experiments detailed in Section 5.5.

Due to the detailed error breakdown provided by GST, all Hamiltonian errors can be experimentally corrected for such that their contribution to the gate infidelity is negligible. As a result, all qubit errors are attributable to stochastic processes. Notably, the bare I gate is particularly degraded by stochastic dephasing, with a gate fidelity of only 96.51%. Idle gate fidelities for dressed and SMART qubits are much higher, equivalent to their corresponding $\sqrt{X}$ and $\sqrt{Y}$ gates (within error). This confirms the noise decoupling benefits provided by the dressing microwave field.

5.4.2 Power sweep

To evaluate the effect of the driving field on the qubit fidelity, GST experiments were performed for varying microwave powers at the Keysight vector signal generator. The power was swept from -7 dBm up to 11 dBm, corresponding to qubit 1 Rabi frequencies of 0.255 MHz and 2.16 MHz respectively. The results for the SMART driving field are shifted down by 1.5 dB since the sinusoidally modulated field delivers less average power to the qubit. A few notable effects of microwave power are observable in the GST results (Fig. 5.8). For bare qubits,

Gate	Error mechanism	FOGI quantity composition
$\sqrt{X}$	Dephasing	S_X
	Bitflips	$S_Y + S_Z$
	Over/underrotation	H_X
	Axis Misalignment	$\frac{1}{2}\left(H_Y(X_{\frac{\pi}{2}}) + H_Z(X_{\frac{\pi}{2}}) + H_X(Y_{\frac{\pi}{2}}) - H_Z(Y_{\frac{\pi}{2}})\right)$
$\sqrt{Y}$	Dephasing	S_Y
	Bitflips	$S_X + S_Z$
	Over/underrotation	H_Y
	Axis Misalignment	$\frac{1}{2}\left(H_Y(X_{\frac{\pi}{2}}) + H_Z(X_{\frac{\pi}{2}}) + H_X(Y_{\frac{\pi}{2}}) - H_Z(Y_{\frac{\pi}{2}})\right)$
I	Dephasing	S_Z
	Bitflips	$S_X + S_Y$
	Over/underrotation	H_Z
	Axis Misalignment	$\sqrt{H_X^2 + H_Y^2}$

Table 5.1: **First-order gauge invariant (FOGI) quantities for single qubit GST.** H_i and S_i denote the Hamiltonian and stochastic errors around axis $i \in \{X, Y, Z\}$. Note that the dressed and SMART axes are defined in the dressed basis. Adapted from Ref. [135].

there is an increase in Hamiltonian rotation errors at higher powers (Fig. 5.8 (a)). This is possibly due to heating induced shifts of the qubit frequency [172]. The decrease in I-gate dephasing noise is explained by faster gate times from the speedup in Rabi frequency. The extremely low infidelities of the X and Y gates are comparable to the error bar magnitudes, making conclusions difficult to draw (Fig. 5.8 (d,g)).

For the dressed and SMART qubits power sweep results, there is a broad trend of increasing bitflip (off-axis stochastic) and decreasing dephasing (on-axis stochastic) errors (Fig. 5.8 (b-c,e-f,h-i). Similar to the bare case, the decrease in dephasing error could be due to the decrease in gate time. The increase in bitflip error could be caused by distortions introduced by the microwave source or two level fluctuators at higher powers. There is also a notable

increase in all stochastic errors for the SMART qubits which occurs for power greater than 7 dBm.

5.4.3 Gate Set Tomography with introduced error

There is an inherent variability in scalable SiMOS qubit arrays due to spin-orbit effects caused by the randomness of the Si/SiO_2 interface [162]. As a result, any global control scheme must be resilient to variations in Rabi and Larmor frequencies between qubits. To characterise the robustness of the driven gates to qubit variability, GST experiments are performed with the introduction of fixed offsets in the Rabi or Larmor frequency (Fig. 5.9). All experiments are performed using the same electronic configuration and microwave power: 2 dBm at the signal generator corresponding to a Rabi frequency of 736 kHz. From Figure 5.9 (e-f), it is evident that the dressed and SMART identity gates are more resilient to Larmor frequency offsets, while the SMART identity gate is more resilient to Rabi frequency offsets. These results generally agree with the simulations detailed in Ref. [124]. However, this pattern does not hold true for the X and Y gate infidelities. Therefore, a more detailed analysis of the GST results is required to explain the infidelity results.

5.4.3.1 Larmor error

Figure 5.10 shows the error mechanism decomposition of the Larmor sweep infidelities plotted in Fig. 5.9 (f,h,i). For bare qubits, the dominant source of error introduced is Hamiltonian. The Larmor offset manifests in the I gate as an over/under-rotation along the Z-axis (Fig. 5.10 (a)). For the X and Y gates

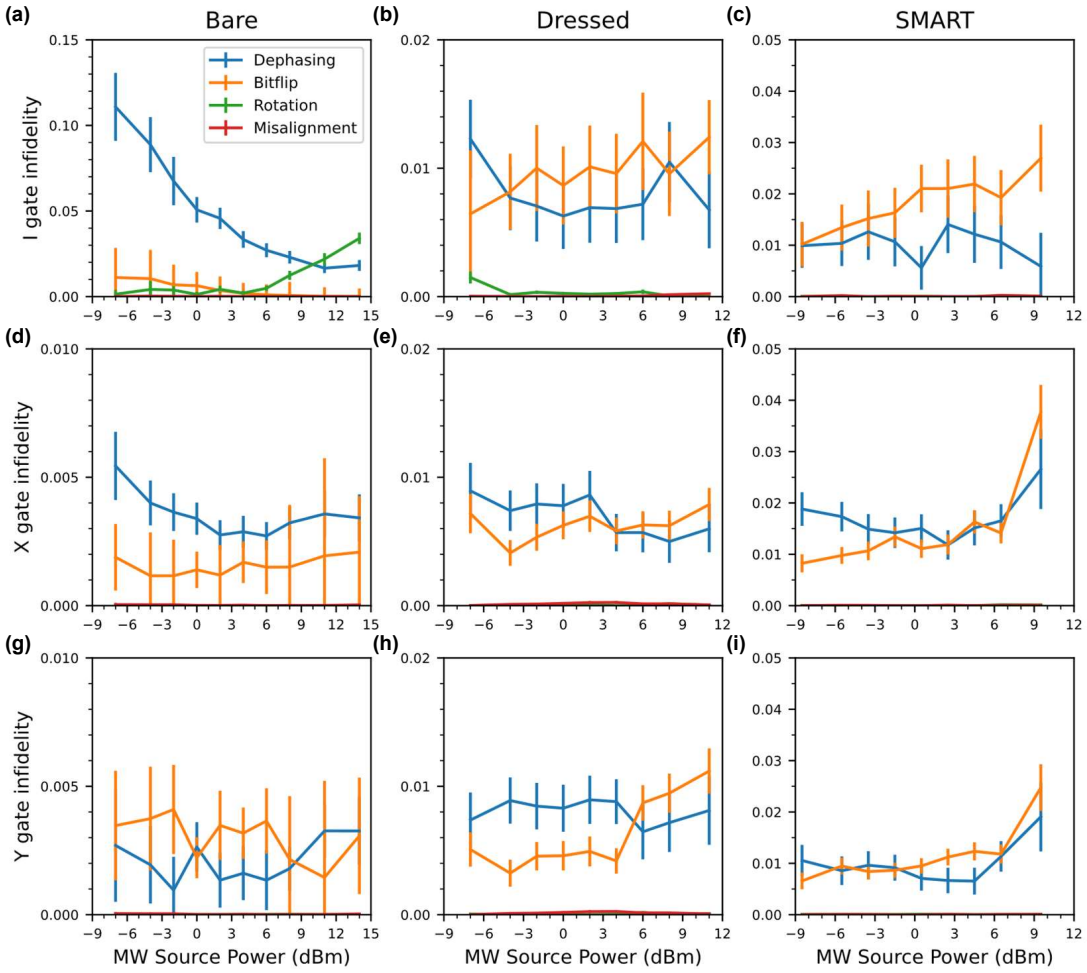

Figure 5.8: **GST gate infidelities as a function of microwave power. (a-c)** Idle gate infidelities of (a) bare, (b) dressed FM and (c) SMART gates as a function of microwave power. **(d-f)** $\sqrt{X}$ gate infidelities as a function of microwave power. **(g-i)** $\sqrt{Y}$ gate infidelities as a function of microwave power.

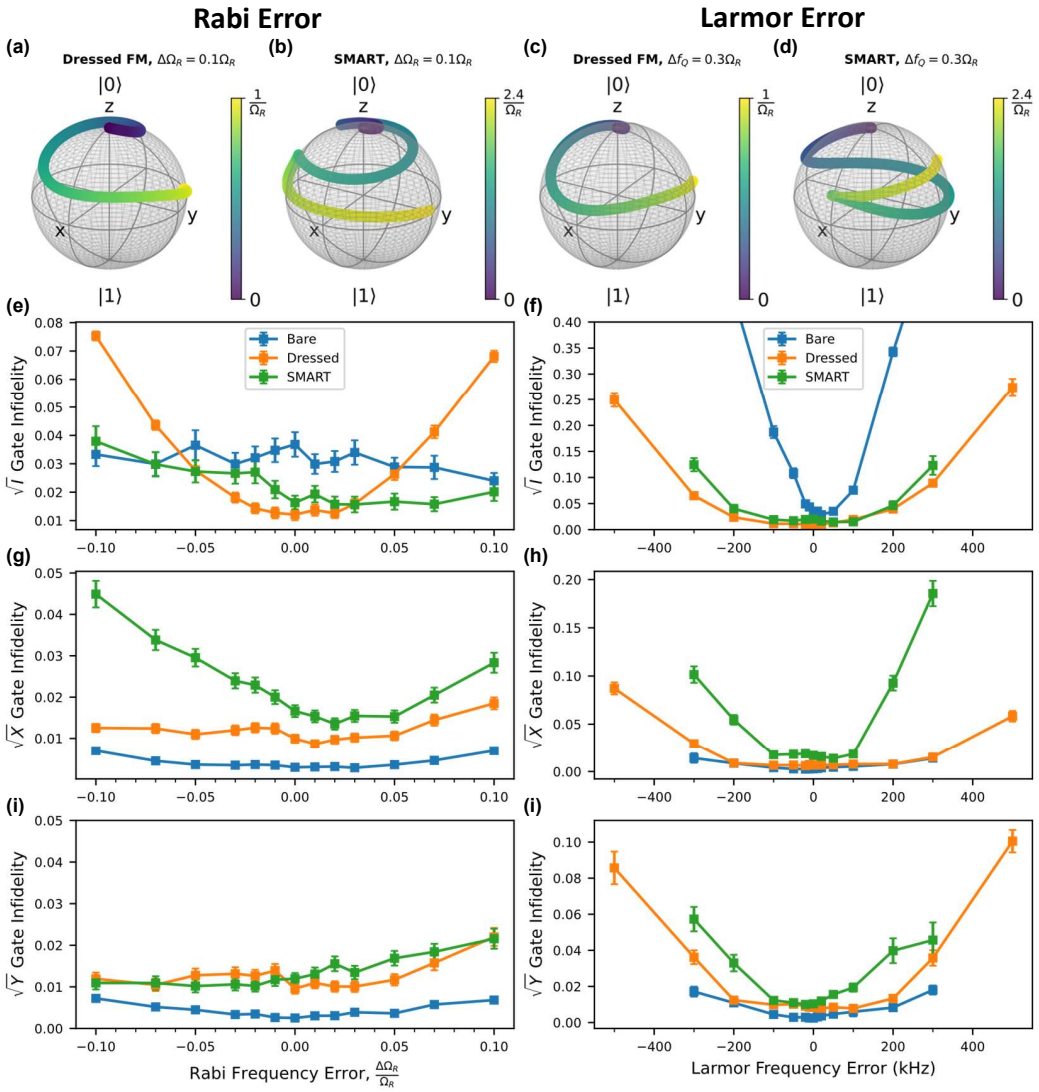

Figure 5.9: **GST fidelity results with introduced error.** **(a-b)** Bloch sphere visualisations of (a) dressed and (b) SMART $-\sqrt{X}$ gates with a 10% error in the Rabi frequency. **(c-d)** Bloch sphere visualisations of (c) dressed and (d) SMART $-\sqrt{X}$ gates with Larmor frequency error equal to 30% of the Rabi frequency. **(e-f)** Idle gate infidelities in the presence of introduced offsets in the (e) Rabi or (f) Larmor frequencies. The Rabi error is expressed as a fraction of the Rabi frequency, while the Larmor error is an absolute value. The Rabi frequency for these GST experiment is $\Omega_R = 736$kHz. Compared to bare gates, the dressed gates are more robust to Larmor errors, while the SMART gates are more robust to both Larmor and Rabi errors. **(g-h)** $-\sqrt{X}$ gate infidelities for the same Rabi and Larmor offsets as (e-f). **(i-j)** $\sqrt{Y}$ gate infidelities for the same Rabi and Larmor offsets as (e-f).

(Fig. 5.10 (d,g), both rotation and axis misalignment errors are introduced. This corresponds to an off-axis rotation, in good agreement with the theory of off-resonant Rabi oscillations. The decoupling effect of the dressed field is evident from the decrease in I-gate Hamiltonian errors for both dressed and SMART qubits.

The stochastic errors of the dressed and SMART gates increase for larger Larmor offset. This is because the noise cancelling properties of the driven schemes are not as effective: using the language of the geometric formalism [168], a Larmor error causes the space curve to become non-closed, thereby becoming vulnerable to first-order noise [124]. For SMART gates, the dephasing and bit-flip errors are asymmetric, implying that the axis of the noise is dependent on the sign of the Larmor error. This asymmetry is not observed in the dressed qubit results.

5.4.3.2 Rabi error

Figure 5.11 shows the error mechanism decomposition of the Rabi sweep infidelities plotted in Figure 5.9 (e,g,i). As expected, introducing a Rabi error causes an over/under-rotation in the bare X/Y and dressed I gates (Fig. 5.11 (b,d,g)). These Hamiltonian I-gate errors are completely eliminated by the sinusoidally modulated field of the SMART protocol (Fig. 5.11 (c)). Since there is no driving field during the Bare I gate, the infidelity is completely independent of any Rabi error (Fig. 5.11 (a)). Similar to the Larmor error results, the stochastic noise of the SMART gates increases with Rabi offset, indicating that first-order quasi-static noise processes are coupling to the qubit.

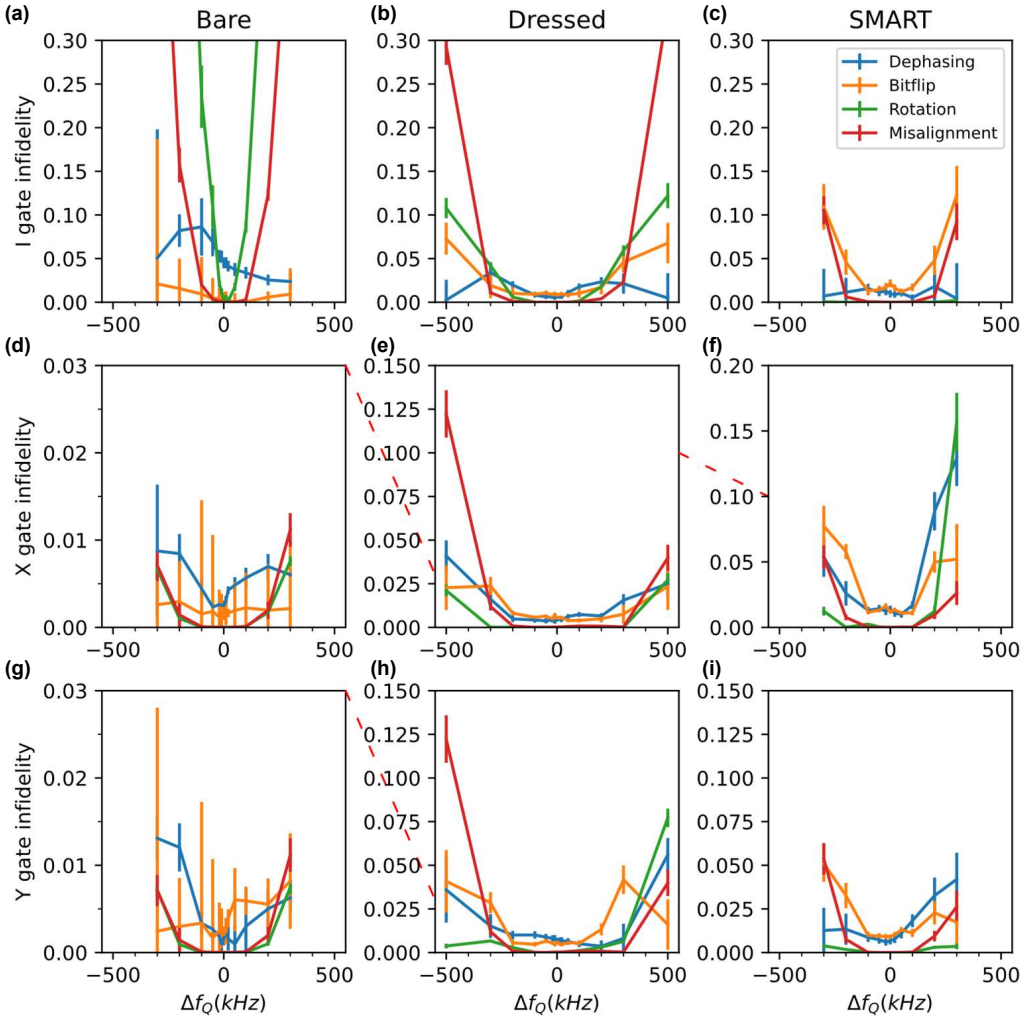

Figure 5.10: **GST infidelity contributions under Larmor error offsets. (a-c)** Bare, dressed FM and SMART I-gate infidelity contributions of FOGI quantities as a function of Larmor frequency error. The Rabi frequency for all experiments is $\Omega_R = 736$ kHz. **(d-f)** X-gate infidelity contributions. **(g-i)** Y-gate infidelity contributions. Red dashed lines indicate changes in y-axis scale.

5.5 Noise Spectroscopy

A surprising outcome of the GST results in Section 5.4 is the SMART protocol's modest fidelities relative to dressed FM, which is at odds with previous experi-

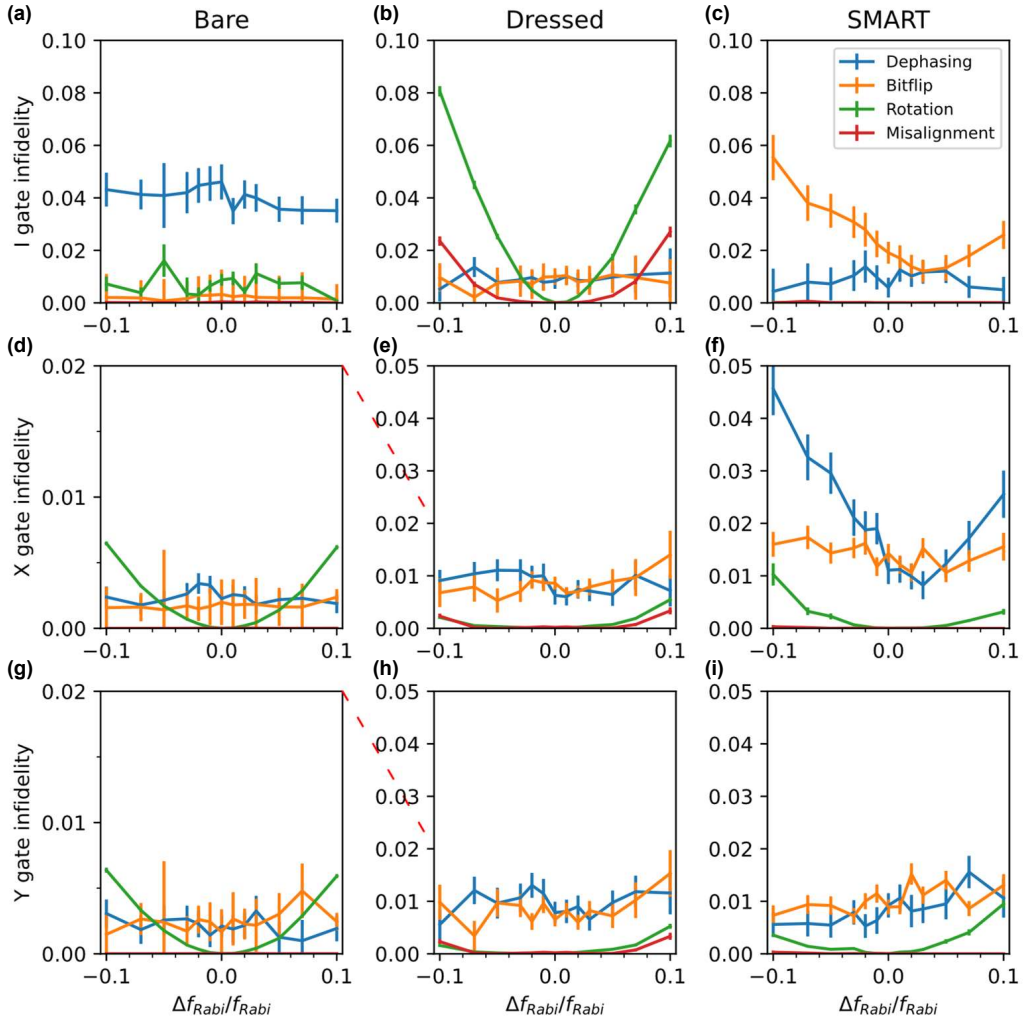

Figure 5.11: **GST infidelity contributions under Rabi error offsets. (a-c)** Bare, dressed FM and SMART I-gate infidelity contributions of FOGI quantities as a function of Rabi frequency error, expressed as a fraction of the Rabi frequency. **(d-f)** X-gate infidelity contributions. **(g-i)** Y-gate infidelity contributions. Red dashed lines indicate changes in y-axis scale.

ments [166]. This section details the noise spectroscopy experiments performed to characterise the noise sources affecting qubit coherence and posit possible explanations for this discrepancy. The noise spectroscopy techniques presented here focus on frequencies on the order of the Rabi frequency (∼MHz).

5.5.1 CPMG

Carr-Purcell-Meiboom-Gill (CPMG) noise spectroscopy is a technique commonly used to characterise noise sources that affect the coherence of qubit systems. It utilises CPMG pulse sequences [173, 174] which consist of refocusing π-pulses interleaved with wait times of period τ [175, 176]. Sweeping τ allows one to probe noise at frequencies in the kHz to MHz range (Fig. 5.12).

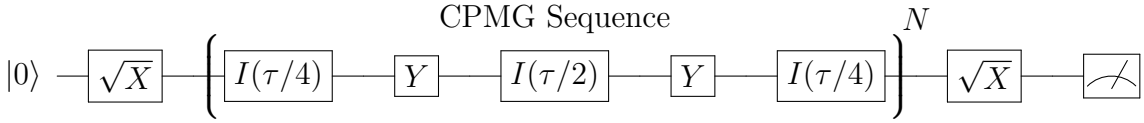

Figure 5.12: **Quantum circuit diagram for a CPMG spectroscopy sequence.**

Figure 5.13 shows the noise spectrum of qubit 1 measured with CPMG spectroscopy for microwave powers ranging from -4 dBm up to 14 dBm. The noise spectral density is observed to be strongly dependent on power. This suggests that the dominant source of decoherence at higher microwave powers occurs during the refocusing π-pulses, not the idle period τ. A 1/f-like noise spectrum is observable in the lowest power noise trace, which transitions to a white noise floor at approximately 40 kHz. A blue noise spectrum is also visible for frequencies approaching 1 MHz. This effect is not unique to devices driven with a dielectric resonator; similar results were observed in a SiMOS device driven by an on-chip broadband transmission line antenna [18]. Additional noise spectroscopy techniques are therefore required to probe higher frequencies and ascertain the physical source of blue noise.

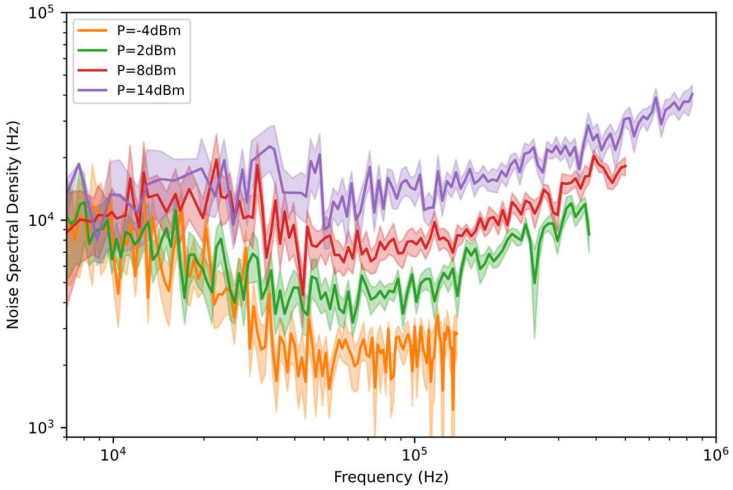

Figure 5.13: **Qubit 1 CPMG noise spectroscopy for different microwave powers**. Different noise frequencies are probed by varying the CPMG sequence wait time τ. A blue noise spectrum is observable at frequencies above 1MHz. Shaded regions indicate the 95% confidence intervals of the noise spectral density.

5.5.2 Spin Locking

Spin locking spectroscopy is a noise characterisation protocol which is capable of measuring noise at frequencies higher than that of CPMG. A microwave field is applied for a period τ to the qubit in an eigenstate of the qubit dressed by the driving field (Fig. 5.14). The spin is 'locked' to the axis of the driving field and the dominant cause of decoherence is noise at the Rabi frequency. The decay time, $T_{1\rho}$ is named due to its similarity to spin relaxation experiments when viewed in the dressed basis. By varying the applied microwave power, spin locking can be used to probe noise at frequencies in the MHz range [177, 178]. Spin locking experiments were performed on qubit 1 for Rabi frequencies in the range 0.2–2.8 MHz by varying the output power of the microwave source and the amplitude of the I/Q modulation signal (Fig. 5.15). The measured

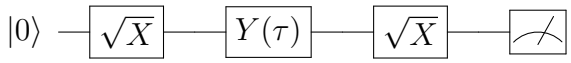

Figure 5.14: **Quantum circuit diagram for spin locking spectroscopy.**

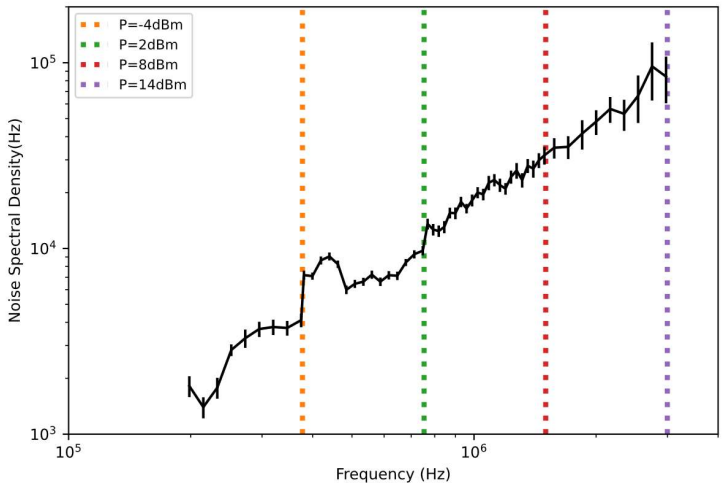

Figure 5.15: **Qubit 1 spin locking spectroscopy.** The Rabi frequency (and noise frequency) is swept by changing the power of the microwave drive signal. Vertical dashed lines indicate the corresponding Rabi frequency at the microwave powers applied in Fig. 5.13

noise spectral density increases with microwave power; similar noise spectra have been observed in spin locking results in other devices in SiMOS and Rabi spectroscopy results in GaAs [179]. The authors of Ref. [179] attributed the blue noise to heating-induced frequency noise or spin relaxation via photon-assisted tunneling.

All of the experiments detailed in this section are not able to differentiate between power-dependent noise from other mechanisms because the noise frequency cannot be changed without also varying the microwave drive power. Hence, more advanced spin locking experiments are required to distinguish the power-dependent noise.

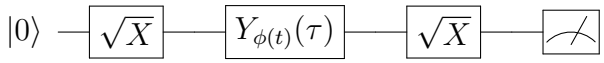

Figure 5.16: **Quantum circuit diagram for spin locking spectroscopy with phase modulation.**

5.5.3 Phase modulated spin locking

Adding a phase modulation to the spin locking drive allows one to probe different noise frequencies with a constant microwave power (Fig. 5.16). Consequently, the noise spectrum obtained is independent of the drive power. A sinusoidal phase modulation $\phi(t)$ is applied to the I/Q modulation signals generated by the OPX, expressed as

$$\phi(t) = A\sin(\omega_\phi t), \tag{5.9}$$

where A is the phase modulation amplitude and $\omega_\phi = 8\Omega_{\mathrm{R}}$ is the phase modulation frequency. The full equations for the I/Q modulation signals for I/Q amplitude A_{MW} are:

$$I = A_{\mathrm{MW}}\sin(A\sin(\omega_\phi t)) \tag{5.10}$$

$$Q = -A_{\mathrm{MW}}\cos(A\sin(\omega_\phi t)). \tag{5.11}$$

When A=0, the modulations signals simplify to the standard spin locking experiment of Section 5.5.2. The noise frequency f_{noise} probed by the spin locking experiment follows the zeroth-order Bessel function of the first kind, $J_0(x)$:

$$f_{\mathrm{noise}}(A) = |J_0(A)|\omega_{\mathrm{R}}. \tag{5.12}$$

Figure 5.17 (a) shows results of phase-modulated spin locking for a single microwave power P=14 dBm. The qubit state (averaged over 100 shots) is plotted

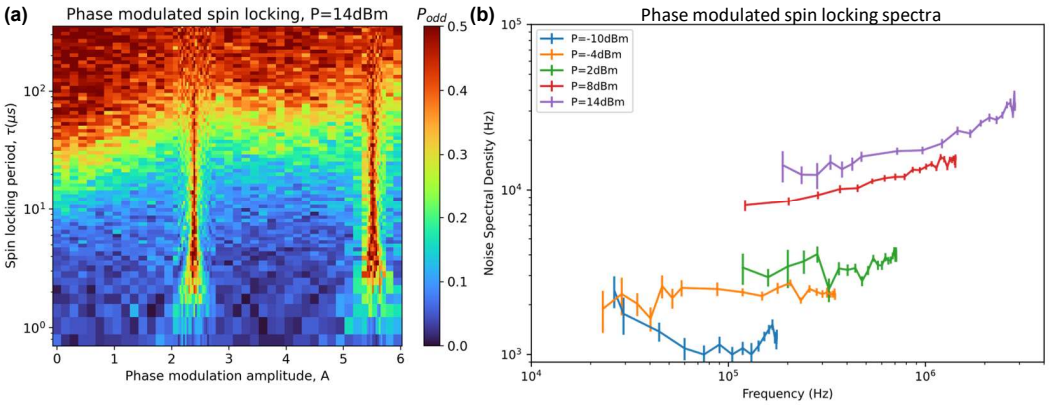

Figure 5.17: **Qubit 1 phase modulated spin locking spectroscopy. (a)** Odd parity readout probability as a function of spin locking period τ and phase modulation amplitude A. **(b)** Phase modulated spin locking spectroscopy results for several microwave powers. In contrast to Fig. 5.15, the noise frequency is changed by varying the phase modulation amplitude, allowing for a noise spectrum independent of microwave power.

as a function of spin locking period and phase modulation amplitude. There is a sudden increase in decoherence at $A = 2.4, 5.5$: this corresponds to the phase modulation amplitudes where $J_0(A) = 0$, around which the qubit is exposed to low frequency noise. For a given phase modulation, the results are fitted to an exponential decay function and repeated for several microwave powers (Fig.5.17 (b)). Since the Bessel function is not one-to-one, the noise frequency probed is repeated for amplitudes past the first zero of J_0: these data points are not plotted for clarity. Due to the very fast decoherence at low frequencies, the error bars of the exponential fit become larger than the noise density. These points are also excluded from Figure 5.17 (b).

From the noise spectrum, a strong power-dependent component of the noise is observed. Connecting the rightmost points of each curve (when the phase modulation amplitude is zero) recovers the same blue noise spectrum as in Figure

5.15. A surprising result from the phase modulated spin locking spectra is the apparent observation of blue noise, even with constant microwave drive power. This suggests the presence of a noise mechanism which cannot be explained by microwave-induced heating alone. The origin of this noise remains an open question: it could be a product of the experimental setup (e.g. introduced by the microwave signal chain) or an artifact of the spectroscopy protocol (e.g. sampling noise at the phase modulation frequency ω_ϕ).

5.5.4 Noise spectroscopy and driven gates

These noise spectroscopy results provide an important insight into possible noise mechanisms present in driven qubits. As discussed in Ref. [125], the dressed and SMART protocols filter low frequency Larmor noise in exchange for increased susceptibility to noise around the Rabi frequency. The spin locking and CPMG results reveal a blue noise spectrum which is strongly dependent on the power of the microwave drive. This explains the lower GST fidelities of SMART gates relative to dressed: since the longer SMART gate time $T_{\mathrm{SMART}} = 2.4T_{\mathrm{Dressed}}$ exposes the qubit to high frequency noise for longer without compensatory benefits from noise cancellation.

The exact physical mechanism of the microwave-induced noise is not clear. One possible candidate is the excitation of two-level fluctuators (TLFs) in the oxide, dielectric and doped regions of the device. Reducing resonator losses (thereby increasing the quality factor) through improvements to device fabrication would reduce power-dependent noise, greatly improving the performance of driven gates.

5.6 Discussion

This chapter has demonstrated two-axis control of bare, dressed and SMART qubits driven with the global field of a dielectric resonator. GST and noise spectroscopy were used to benchmark the qubits and identify possible causes of decoherence. These results represent a significant step in the implementation of global control for a scalable qubit array. Implementing initialisation and readout protocols in the presence of a global field (such as in Ref. [123] is the next step towards demonstrating the viability of global control in scalable qubit arrays.

The detailed noise spectroscopy data collected in this chapter allows for tailored improvements to be made to the SMART protocol. For example, harmonics of the global field and Stark shift signals can be added which adapt the filter function of the SMART protocol to suit the qubit's specific noise profile.

More complex noise spectroscopy protocols are also possible which can shed more light on the sources of noise in the device. By introducing a detuning offset to the spin locking experiment, the noise spectrum can be separated into Rabi and Larmor components [177]. More advanced phase modulation waveforms or a sinusoidally modulating spin locking field could also be implemented.

A notable limitation of the current experimental setup is the 1D magnetic field. The magnetic field is aligned with the [110] axis with respect to the silicon crystal lattice, an orientation which maximises the spin-orbit coupling of the qubit [162]. As a result, there is a large variability in qubit frequency between quantum dots, precluding simultaneous two-qubit control in this device. Future global control experiments could change the orientation of the magnetic field

by either physically rotating the qubit device or by using a cryogenic setup with a vector magnet. This would allow for the implementation of multi-qubit gates and quantum algorithms which use global control.

Chapter 6

Conclusion

This thesis has investigated two distinct problems relating to the scalability of semiconductor spin qubits.

First, the coupling of an electron spin to a superconducting resonator was explored with the aim of establishing quantum operations between distant qubits. The theory of spin-photon coupling was applied to the intrinsic spin-orbit interaction observed for electrons tightly confined in SiMOS quantum dots. A combination of theoretical analysis and experimental data was used to estimate spin-photon coupling strengths in the transverse and longitudinal coupling regimes. The transverse spin-photon coupling strength was extrapolated to 4 MHz in the single-photon limit, suggesting that the strong transverse coupling regime is attainable assuming the integration of a suitable high-impedance resonator. While the dynamic longitudinal coupling was found to be insufficient for strong coupling, it may become possible in future experiments with improvements in resonator fabrication and device tuning.

Superconducting resonators were successfully integrated with a quantum dot device, with a measured internal quality factor of 820. High-impedance resonators were fabricated from MoRe and tested, showing a sizeable kinetic inductance and quality factors exceeding 10^4, which is comparable to other commonly used superconducting resonator materials. The thickness of the insulating dry oxide layer did not have significant effect on resonator quality factors. While the simultaneous operation of qubits and resonator was not achieved due to poor quantum dot device yield, these results represent a step towards experimental demonstrations of spin-photon coupling in SiMOS devices.

Finally, experiments were conducted on a two-qubit device with a global driving field supplied by a dielectric resonator. Qubit coherence times were found to be comparable to other SiMOS devices. Two-axis control of bare, dressed and SMART qubits was implemented and GST was used to benchmark and compare the error sources of each control scheme. Fidelities above 99% were reported for the dressed FM qubits, with greatly improved identity gate fidelities over bare qubits. Qubit spectroscopy experiments were performed to identify physical sources of noise; the noise was found to scale significantly with microwave power, suggesting a decoherence mechanism related to the microwave drive. These results are the first fidelity results obtained with a dielectric resonator, and prove the viability of both dielectric resonators and dressed control schemes in the large globally-driven qubit arrays of the future.

6.1 Future directions

The theory suggests that strong spin-photon coupling is possible with improvements in the fabrication and integration of superconducting resonators with SiMOS qubit devices. However, there is still significant work to be done to make this a reality. The first step is to determine the cause of the drop-off in internal Q-factor for the integrated resonator. The resonator quality factor could be improved with better gate filtering [107], moving the resonator off-chip [146], and optimal gate design to reduce cross-capacitance. The spin decoherence rate can be reduced with advancements in isotopically purified substrates [45] and improved fabrication processes for the mitigation of charge noise [48]. The spin-photon coupling strength could be improved by using granular aluminium for the resonator [59] and increasing the gate lever arm with better gate design [147]. Hole spin qubits in silicon are also a promising research avenue for spin-photon coupling. A strong spin-orbit interaction has been observed for planar hole devices in SiMOS [180], which is readily applied to cQED experiments. The coupling strength reported for holes in silicon nanowires is the highest of any spin-photon system to date [33]. However, working with holes also comes with additional challenges such as anisotropy of the hole spin's g-factor [60], susceptibility to charge noise [181, 182], and reduced readout fidelity [180]. Strong spin-photon coupling does not automatically enable a high fidelity two-qubit gate. Spin relaxation induced by the Purcell effect [151] has been shown to be greatly detrimental to two-qubit gate performance [120]. This could be reduced with the integration of Purcell filters [152] or by detuning the resonator from the qubit [153, 183]. Overcoming these challenges, along with improvements in the spin-photon coupling strength, may

allow for the implementation of a high fidelity two-qubit gate mediated by a resonator.

The results presented in this thesis on dielectric resonators show great promise for their use in the control of scalable qubit arrays. The logical progression from the single-qubit results of Chapter 5 is the demonstration of two-qubit control with a dielectric resonator, which could be achieved with a vector magnet. The initialisation and measurement of qubits under a global field is another avenue for further research [123].

Improvements to gate fidelities could be achieved by reducing losses in the dielectric resonator, thereby increasing the quality factor. The power-to-field conversion factor $C = B_1/\sqrt{P}$ is a metric that quantifies the magnetic field applied by the dielectric resonator for a given power. The conversion factor $C \propto \sqrt{Q}$, hence increasing the quality factor allows one to drive equivalent magnetic fields at reduced microwave power. This could lessen the effect of the power-dependent noise seen in noise spectroscopy experiments in Section 5.5. By reducing the area of doped ohmic regions, harnessing foundry fabrication processes, and optimising device design, the most recent generation of devices have already increased Q_i by an order of magnitude over the device reported in this chapter. Further Q-factor improvements could be achieved by depositing a superconducting film on the dielectric resonator (with an aperture) to shield the device from stray fields. The resonator could also be placed on the back of the chip, reducing eddy currents induced in the bond wires and gate stack.

The ohmic regions which form the SET channel and electron reservoir for electron qubits in SiMOS are a significant source of dissipative loss for the dielectric resonator [35]. Therefore, the SETs currently used for readout are detrimen-

tal to the dielectric resonator quality factor, especially for scalable arrays with SETs adjacent to all qubits. Hence, there is a strong case for gate-based dispersive readout [79, 80], which does not require ohmic regions or additional metal gates.

Recent progress on foundry-made devices is promising [51,184,185] and devices with hundreds of qubits may only be a few years away. Ultimately, the true test of a global control scheme will be its experimental implementation in a large-scale qubit array.

Appendix A

Dressed Basis

This section derives the bare and dressed bases used in Chapter 5 and largely follows the analysis contained in Ref. [123].

The Hamiltonian of a spin in an external magnetic field can be expressed as

$$\mathcal{H}_{\mathrm{q}} = \hbar\omega_{\mathrm{q}}\sigma_z, \tag{A.1}$$

where $\omega_{\mathrm{q}} = 2\pi f_{\mathrm{q}}$ is the angular frequency of the qubit. This analysis can be applied to any two-level system; for an electron in a magnetic field B_0, the qubit's energy levels are separated by a Zeeman splitting with energy

$$\hbar\omega_{\mathrm{q}} = g\mu_{\mathrm{B}}B_0 \tag{A.2}$$

where g is the g-factor of the electron and μ_{B} is the Bohr magneton. To perform qubit operations, a microwave drive with frequency f_{MW} and amplitude A_{MW} induces a transverse AC magnetic field (defined here along the x-axis). The total Hamiltonian becomes:

$$\mathcal{H}_{\mathrm{tot}} = \frac{\hbar\omega_{\mathrm{q}}}{2}\sigma_z + A_{\mathrm{MW}}\cos(2\pi f_{\mathrm{MW}}t)\sigma_x \tag{A.3}$$

This Hamiltonian describes the qubit in what is commonly termed the *laboratory frame*. To simplify analysis, the Hamiltonian is transformed into a frame rotating at the angular frequency of the qubit ω_{q}. Using the standard rotating wave approximation, the Hamiltonian becomes

$$\mathcal{H}_{\mathrm{bare}} = \frac{h}{2}(\Delta\sigma_z + \Omega_{\mathrm{R}}\sigma_x), \tag{A.4}$$

where $\Delta = |f_{\mathrm{q}} - f_{\mathrm{MW}}|$ is the detuning between the qubit and field, and Ω_{R} is the Rabi frequency. This is commonly known as the rotating frame. In this thesis, it is also called the *bare basis* and all bare qubits and gates (such as in Fig. 5.5 (a)) are defined in this basis.

For qubits in an always-driven microwave field, it becomes more convenient to define the qubits in the eigenbasis of the driving field. Therefore, a Hadamard transformation is applied to determine the dressed Hamiltonian

$$\mathcal{H}_{\mathrm{dressed}} = H\mathcal{H}_{\mathrm{bare}}H^{\dagger}, \tag{A.5}$$

where H is the unitary representation of the Hadamard gate:

$$H = \frac{1}{\sqrt{2}}\begin{pmatrix} 1 & 1 \\ 1 & -1 \end{pmatrix}. \tag{A.6}$$

This equates to a swapping of the X and Z axes on the Bloch sphere. In experiment, the qubit is initialised in the bare basis before a $Y_{\pi/2}$ projection pulse is applied to initialise the $+|z_\rho\rangle$ state. The inverse is applied before performing qubit readout.

Appendix B

Fabrication recipes

This appendix lists recipes used for fabrication of superconducting resonators and hybrid resonator-qubit devices. Fabrication processes not carried out by the author (such as oxide growth and electron beam lithography) are not included.

B.1 MoRe sputtering

1. Preclean MoRe target for 5 minutes, 300W, 450V, 20mTorr Argon gas.
2. Deposit MoRe, 300W, 450V, 3mTorr Argon gas. Deposition rate $\sim$ 18nm/min
3. Lift-off with acetone. Sonication may be required

B.2 Ion milling and Al deposition

1. Ion mill 4 minutes, 5nm milled
    - Discharge voltage: 40V
    - Beam voltage: 600V
    - Beam current 36mA
    - 2mTorr Argon gas.
2. Deposit Al, 80nm@1Å/s

B.3 Direct writer UV lithography

1. Spin nLOF2020 @ 5000rpm, 30s
2. Pre-bake @ 110°C for 1 min
3. Expose with DMO MicroWriter ML3
    - Exposure quality: High
    - Dose: 65-68
4. Post-bake @ 110°C for 1 min
5. Develop with AZ826MIF, 1 min
6. 30 sec DI rinse + N2 dry
7. O_2 Plasma ash – 5min, 50W

References

[1] R. P. Feynman, "Simulating physics with computers," *International journal of theoretical physics*, vol. 21, no. 6/7, pp. 467–488, 1982.

[2] S. Lloyd, "Universal quantum simulators," *Science*, vol. 273, no. 5278, pp. 1073–1078, 1996.

[3] P. W. Shor, "Polynomial-time algorithms for prime factorization and discrete logarithms on a quantum computer," *SIAM Journal on Computing*, vol. 26, no. 5, pp. 1484–1509, 1997.

[4] R. L. Rivest, A. Shamir, and L. Adleman, "A method for obtaining digital signatures and public-key cryptosystems," *Communications of the ACM*, vol. 21, no. 2, pp. 120–126, 1978.

[5] A. G. Fowler, M. Mariantoni, J. M. Martinis, and A. N. Cleland, "Surface codes: Towards practical large-scale quantum computation," *Physical Review A*, vol. 86, no. 3, p. 032324, 2012.

[6] E. T. Campbell, B. M. Terhal, and C. Vuillot, "Roads towards fault-tolerant universal quantum computation," *Nature*, vol. 549, no. 7671, pp. 172–179, 2017.

[7] F. Arute, K. Arya, R. Babbush, D. Bacon, J. C. Bardin, R. Barends, R. Biswas, S. Boixo, F. G. Brandao, D. A. Buell *et al.*, "Quantum supremacy using a programmable superconducting processor," *Nature*, vol. 574, no. 7779, pp. 505–510, 2019.

[8] F. Pan, K. Chen, and P. Zhang, "Solving the sampling problem of the sycamore quantum circuits," *Phys. Rev. Lett.*, vol. 129, p. 090502, Aug 2022. [Online]. Available: https://link.aps.org/doi/10.1103/PhysRevLett.129.090502

[9] Y. Kim, A. Eddins, S. Anand, K. X. Wei, E. Van Den Berg, S. Rosenblatt, H. Nayfeh, Y. Wu, M. Zaletel, K. Temme *et al.*, "Evidence for the utility of quantum computing before fault tolerance," *Nature*, vol. 618, no. 7965, pp. 500–505, 2023.

[10] A. Wallraff, D. Schuster, A. Blais, L. Frunzio, R.-S. Huang, J. Majer, S. Kumar, S. Girvin, and R. Schoelkopf, "Strong coupling of a single photon to a superconducting qubit using circuit quantum electrodynamics," *Nature*, vol. 431, no. 7005, pp. 162–167, 2004.

[11] Google Quantum AI and Collaborators, "Quantum error correction below the surface code threshold," 2024. [Online]. Available: https://arxiv.org/abs/2408.13687

[12] R. Blatt and D. Wineland, "Entangled states of trapped atomic ions," *Nature*, vol. 453, no. 7198, pp. 1008–1015, 2008.

[13] C. D. Bruzewicz, J. Chiaverini, R. McConnell, and J. M. Sage, "Trapped-ion quantum computing: Progress and challenges," *Applied Physics Reviews*, vol. 6, no. 2, 2019.

[14] S. J. Evered, D. Bluvstein, M. Kalinowski, S. Ebadi, T. Manovitz, H. Zhou, S. H. Li, A. A. Geim, T. T. Wang, N. Maskara *et al.*, "High-fidelity parallel entangling gates on a neutral-atom quantum computer," *Nature*, vol. 622, no. 7982, pp. 268–272, 2023.

[15] P. Kok, W. J. Munro, K. Nemoto, T. C. Ralph, J. P. Dowling, and G. J. Milburn, "Linear optical quantum computing with photonic qubits," *Reviews of modern physics*, vol. 79, no. 1, pp. 135–174, 2007.

[16] K. Alexander, A. Bahgat, A. Benyamini, D. Black, D. Bonneau, S. Burgos, B. Burridge, G. Campbell, G. Catalano, A. Ceballos *et al.*, "A manufacturable platform for photonic quantum computing," *arXiv preprint arXiv:2404.17570*, 2024.

[17] N. Maring, A. Fyrillas, M. Pont, E. Ivanov, P. Stepanov, N. Margaria, W. Hease, A. Pishchagin, A. Lemaître, I. Sagnes *et al.*, "A versatile single-photon-based quantum computing platform," *Nature Photonics*, vol. 18, no. 6, pp. 603–609, 2024.

[18] J. Y. Huang, R. Y. Su, W. H. Lim, M. Feng, B. van Straaten, B. Severin, W. Gilbert, N. D. Stuyck, T. Tanttu, S. Serrano, J. D. Cifuentes, I. Hansen, A. E. Seedhouse, E. Vahapoglu, R. C. C. Leon, N. V. Abrosimov, H.-J. Pohl, M. L. W. Thewalt, F. E. Hudson, C. C. Escott, N. Ares, S. D. Bartlett, A. Morello, A. Saraiva, A. Laucht, A. S. Dzurak, and C. H. Yang, "High-fidelity spin qubit operation and algorithmic initialization above 1 k," *Nature*, vol. 627, pp. 772–777, 2024. [Online]. Available: https://doi.org/10.1038/s41586-024-07160-2

[19] I. Thorvaldson, D. Poulos, C. M. Moehle, S. H. Misha, H. Edlbauer, J. Reiner, H. Geng, B. Voisin, M. T. Jones, M. B. Donnelly *et al.*,

"Grover's algorithm in a four-qubit silicon processor above the fault-tolerant threshold," *arXiv preprint arXiv:2404.08741*, 2024.

[20] S. G. Philips, M. T. Mądzik, S. V. Amitonov, S. L. de Snoo, M. Russ, N. Kalhor, C. Volk, W. I. Lawrie, D. Brousse, L. Tryputen *et al.*, "Universal control of a six-qubit quantum processor in silicon," *Nature*, vol. 609, no. 7929, pp. 919–924, 2022.

[21] A. R. Mills, C. R. Guinn, M. J. Gullans, A. J. Sigillito, M. M. Feldman, E. Nielsen, and J. R. Petta, "Two-qubit silicon quantum processor with operation fidelity exceeding 99%," *Science Advances*, vol. 8, p. eabn5130, Sep 2023, doi: 10.1126/sciadv.abn5130. [Online]. Available: https://doi.org/10.1126/sciadv.abn5130

[22] N. W. Hendrickx, W. I. L. Lawrie, M. Russ, F. van Riggelen, S. L. de Snoo, R. N. Schouten, A. Sammak, G. Scappucci, and M. Veldhorst, "A four-qubit germanium quantum processor," *Nature*, vol. 591, pp. 580–585, 2021. [Online]. Available: https://doi.org/10.1038/s41586-021-03332-6

[23] D. P. DiVincenzo, "The physical implementation of quantum computation," *Fortschritte der Physik: Progress of Physics*, vol. 48, no. 9-11, pp. 771–783, 2000.

[24] G. Burkard, T. D. Ladd, A. Pan, J. M. Nichol, and J. R. Petta, "Semiconductor spin qubits," *Reviews of Modern Physics*, vol. 95, no. 2, p. 025003, 2023.

[25] N. D. Stuyck, A. Saraiva, W. Gilbert, J. C. Pardo, R. Li, C. C. Escott, K. De Greve, S. Voinigescu, D. J. Reilly, and A. S. Dzu-

rak, “Cmos compatibility of semiconductor spin qubits,” *arXiv preprint arXiv:2409.03993*, 2024.

[26] K. M. Itoh and H. Watanabe, “Isotope engineering of silicon and diamond for quantum computing and sensing applications,” *MRS communications*, vol. 4, no. 4, pp. 143–157, 2014.

[27] C. Yang, R. Leon, J. Hwang, A. Saraiva, T. Tanttu, W. Huang, J. Camirand Lemyre, K. Chan, K. Tan, F. Hudson *et al.*, “Operation of a silicon quantum processor unit cell above one kelvin,” *Nature*, vol. 580, no. 7803, pp. 350–354, 2020.

[28] L. Vandersypen, H. Bluhm, J. Clarke, A. Dzurak, R. Ishihara, A. Morello, D. Reilly, L. Schreiber, and M. Veldhorst, “Interfacing spin qubits in quantum dots and donors—hot, dense, and coherent,” *npj Quantum Information*, vol. 3, no. 1, pp. 1–10, 2017.

[29] M. Veldhorst, C. H. Yang, J. C. C. Hwang, W. Huang, J. P. Dehollain, J. T. Muhonen, S. Simmons, A. Laucht, F. E. Hudson, K. M. Itoh, A. Morello, and A. S. Dzurak, “A two-qubit logic gate in silicon,” *Nature*, vol. 526, pp. 410–414, 2015. [Online]. Available: https://doi.org/10.1038/nature15263

[30] X. Mi, J. V. Cady, D. M. Zajac, P. W. Deelman, and J. R. Petta, “Strong coupling of a single electron in silicon to a microwave photon,” *Science*, vol. 355, no. 6321, p. 156, Jan 2017. [Online]. Available: http://science.sciencemag.org/content/355/6321/156.abstract

[31] N. Samkharadze, G. Zheng, N. Kalhor, D. Brousse, A. Sammak, U. Mendes, A. Blais, G. Scappucci, and L. Vandersypen, “Strong spin-

photon coupling in silicon," *Science*, vol. 359, no. 6380, pp. 1123–1127, 2018.

[32] W. Gilbert, T. Tanttu, W. H. Lim, M. Feng, J. Y. Huang, J. D. Cifuentes, S. Serrano, P. Y. Mai, R. C. Leon, C. C. Escott *et al.*, "On-demand electrical control of spin qubits," *Nature Nanotechnology*, pp. 1–6, 2023.

[33] C. X. Yu, S. Zihlmann, J. C. Abadillo-Uriel, V. P. Michal, N. Rambal, H. Niebojewski, T. Bedecarrats, M. Vinet, Étienne Dumur, M. Filippone, B. Bertrand, S. D. Franceschi, Y.-M. Niquet, and R. Maurand, "Strong coupling between a photon and a hole spin in silicon," *Nature Nanotechnology*, 2023. [Online]. Available: https://doi.org/10.1038/s41565-023-01332-3

[34] R. Li, L. Petit, D. P. Franke, J. P. Dehollain, J. Helsen, M. Steudtner, N. K. Thomas, Z. R. Yoscovits, K. J. Singh, S. Wehner *et al.*, "A crossbar network for silicon quantum dot qubits," *Science advances*, vol. 4, no. 7, p. eaar3960, 2018.

[35] E. Vahapoglu, J. P. Slack-Smith, R. C. C. Leon, W. H. Lim, F. E. Hudson, T. Day, T. Tanttu, C. H. Yang, A. Laucht, A. S. Dzurak, and J. J. Pla, "Single-electron spin resonance in a nanoelectronic device using a global field," *Science Advances*, vol. 7, no. 33, p. eabg9158, 2021. [Online]. Available: https://www.science.org/doi/abs/10.1126/sciadv.abg9158

[36] E. Vahapoglu, J. P. Slack-Smith, R. C. C. Leon, W. H. Lim, F. E. Hudson, T. Day, J. D. Cifuentes, T. Tanttu, C. H. Yang, A. Saraiva, N. V. Abrosimov, H.-J. Pohl, M. L. W. Thewalt, A. Laucht, A. S. Dzurak, and J. J. Pla, "Coherent control of electron spin qubits in

silicon using a global field," *npj Quantum Information*, vol. 8, p. 126, 2022. [Online]. Available: https://doi.org/10.1038/s41534-022-00645-w

[37] D. Loss and D. P. DiVincenzo, "Quantum computation with quantum dots," *Physical Review A*, vol. 57, no. 1, p. 120, 1998.

[38] B. E. Kane, "A silicon-based nuclear spin quantum computer," *Nature*, vol. 393, pp. 133–137, 1998. [Online]. Available: https://doi.org/10.1038/30156

[39] J. R. Petta, A. C. Johnson, J. M. Taylor, E. A. Laird, A. Yacoby, M. D. Lukin, C. M. Marcus, M. P. Hanson, and A. C. Gossard, "Coherent manipulation of coupled electron spins in semiconductor quantum dots," *Science*, vol. 309, no. 5744, pp. 2180–2184, 2005. [Online]. Available: https://www.science.org/doi/abs/10.1126/science.1116955

[40] F. H. L. Koppens, C. Buizert, K. J. Tielrooij, I. T. Vink, K. C. Nowack, T. Meunier, L. P. Kouwenhoven, and L. M. K. Vandersypen, "Driven coherent oscillations of a single electron spin in a quantum dot," *Nature*, vol. 442, pp. 766–771, 2006. [Online]. Available: https://doi.org/10.1038/nature05065

[41] J. J. Pla, K. Y. Tan, J. P. Dehollain, W. H. Lim, J. J. L. Morton, D. N. Jamieson, A. S. Dzurak, and A. Morello, "A single-atom electron spin qubit in silicon," *Nature*, vol. 489, pp. 541–545, 2012. [Online]. Available: https://doi.org/10.1038/nature11449

[42] M. Veldhorst, J. C. C. Hwang, C. H. Yang, A. W. Leenstra, B. de Ronde, J. P. Dehollain, J. T. Muhonen, F. E. Hudson, K. M. Itoh, A. Morello,

and A. S. Dzurak, "An addressable quantum dot qubit with fault-tolerant control-fidelity," *Nature Nanotechnology*, vol. 9, pp. 981–985, 2014. [Online]. Available: https://doi.org/10.1038/nnano.2014.216

[43] T. Tanttu, W. H. Lim, J. Y. Huang, N. D. Stuyck, W. Gilbert, R. Y. Su, M. Feng, J. D. Cifuentes, A. E. Seedhouse, S. K. Seritan, C. I. Ostrove, K. M. Rudinger, R. C. C. Leon, W. Huang, C. C. Escott, K. M. Itoh, N. V. Abrosimov, H.-J. Pohl, M. L. W. Thewalt, F. E. Hudson, R. Blume-Kohout, S. D. Bartlett, A. Morello, A. Laucht, C. H. Yang, A. Saraiva, and A. S. Dzurak, "Assessment of the errors of high-fidelity two-qubit gates in silicon quantum dots," *Nature Physics*, 2024. [Online]. Available: https://doi.org/10.1038/s41567-024-02614-w

[44] P. Becker, H.-J. Pohl, H. Riemann, and N. Abrosimov, "Enrichment of silicon for a better kilogram," *physica status solidi (a)*, vol. 207, no. 1, pp. 49–66, 2010.

[45] R. Acharya, M. Coke, M. Adshead, K. Li, B. Achinuq, R. Cai, A. B. Gholizadeh, J. Jacobs, J. L. Boland, S. J. Haigh *et al.*, "Highly 28si enriched silicon by localised focused ion beam implantation," *Communications Materials*, vol. 5, no. 1, p. 57, 2024.

[46] D. Holmes, B. Johnson, C. Chua, B. Voisin, S. Kocsis, S. Rubanov, S. Robson, J. McCallum, D. McCamey, S. Rogge *et al.*, "Isotopic enrichment of silicon by high fluence 28 si- ion implantation," *Physical Review Materials*, vol. 5, no. 1, p. 014601, 2021.

[47] X. Zhang, E. Morozova, M. Rimbach-Russ, D. Jirovec, T.-K. Hsiao, P. C. Fariña, C.-A. Wang, S. D. Oosterhout, A. Sammak, G. Scappucci *et al.*,

"Universal control of four singlet–triplet qubits," *Nature Nanotechnology*, pp. 1–7, 2024.

[48] A. Elsayed, M. M. K. Shehata, C. Godfrin, S. Kubicek, S. Massar, Y. Canvel, J. Jussot, G. Simion, M. Mongillo, D. Wan, B. Govoreanu, I. P. Radu, R. Li, P. V. Dorpe, and K. D. Greve, "Low charge noise quantum dots with industrial cmos manufacturing," *npj Quantum Information*, vol. 10, p. 70, 2024. [Online]. Available: https://doi.org/10.1038/s41534-024-00864-3

[49] A. M. J. Zwerver, T. Krähenmann, T. F. Watson, L. Lampert, H. C. George, R. Pillarisetty, S. A. Bojarski, P. Amin, S. V. Amitonov, J. M. Boter, R. Caudillo, D. Correas-Serrano, J. P. Dehollain, G. Droulers, E. M. Henry, R. Kotlyar, M. Lodari, F. Lüthi, D. J. Michalak, B. K. Mueller, S. Neyens, J. Roberts, N. Samkharadze, G. Zheng, O. K. Zietz, G. Scappucci, M. Veldhorst, L. M. K. Vandersypen, and J. S. Clarke, "Qubits made by advanced semiconductor manufacturing," *Nature Electronics*, vol. 5, pp. 184–190, 2022. [Online]. Available: https://doi.org/10.1038/s41928-022-00727-9

[50] P. Steinacker, N. D. Stuyck, W. H. Lim, T. Tanttu, M. Feng, A. Nickl, S. Serrano, M. Candido, J. D. Cifuentes, F. E. Hudson, K. W. Chan, S. Kubicek, J. Jussot, Y. Canvel, S. Beyne, Y. Shimura, R. Loo, C. Godfrin, B. Raes, S. Baudot, D. Wan, A. Laucht, C. H. Yang, A. Saraiva, C. C. Escott, K. D. Greve, and A. S. Dzurak, "A 300 mm foundry silicon spin qubit unit cell exceeding 99% fidelity in all operations," 2024. [Online]. Available: https://arxiv.org/abs/2410.15590

[51] T. Koch, C. Godfrin, V. Adam, J. Ferrero, D. Schroller, N. Glaeser, S. Kubicek, R. Li, R. Loo, S. Massar, G. Simion, D. Wan, K. D. Greve, and W. Wernsdorfer, "Industrial 300 mm wafer processed spin qubits in natural silicon/silicon-germanium," 2024. [Online]. Available: https://arxiv.org/abs/2409.12731

[52] W. Lawrie, H. Eenink, N. Hendrickx, J. Boter, L. Petit, S. Amitonov, M. Lodari, B. Paquelet Wuetz, C. Volk, S. Philips *et al.*, "Quantum dot arrays in silicon and germanium," *Applied Physics Letters*, vol. 116, no. 8, 2020.

[53] F. A. Zwanenburg, A. S. Dzurak, A. Morello, M. Y. Simmons, L. C. L. Hollenberg, G. Klimeck, S. Rogge, S. N. Coppersmith, and M. A. Eriksson, "Silicon quantum electronics," *Rev. Mod. Phys.*, vol. 85, pp. 961–1019, Jul 2013. [Online]. Available: https://link.aps.org/doi/10.1103/RevModPhys.85.961

[54] B. P. Wuetz, M. P. Losert, S. Koelling, L. E. A. Stehouwer, A.-M. J. Zwerver, S. G. J. Philips, M. T. Mądzik, X. Xue, G. Zheng, M. Lodari, S. V. Amitonov, N. Samkharadze, A. Sammak, L. M. K. Vandersypen, R. Rahman, S. N. Coppersmith, O. Moutanabbir, M. Friesen, and G. Scappucci, "Atomic fluctuations lifting the energy degeneracy in si/sige quantum dots," *Nature Communications*, vol. 13, p. 7730, 2022. [Online]. Available: https://doi.org/10.1038/s41467-022-35458-0

[55] N. W. Hendrickx, W. I. L. Lawrie, L. Petit, A. Sammak, G. Scappucci, and M. Veldhorst, "A single-hole spin qubit," *Nature Communications*, vol. 11, p. 3478, 2020. [Online]. Available: https://doi.org/10.1038/s41467-020-17211-7

[56] W. I. L. Lawrie, N. W. Hendrickx, F. van Riggelen, M. Russ, L. Petit, A. Sammak, G. Scappucci, and M. Veldhorst, "Spin relaxation benchmarks and individual qubit addressability for holes in quantum dots," *Nano Letters*, vol. 20, pp. 7237–7242, Oct 2020, doi: 10.1021/acs.nanolett.0c02589. [Online]. Available: https://doi.org/10.1021/acs.nanolett.0c02589

[57] S. D. Liles, D. J. Halverson, Z. Wang, A. Shamim, R. S. Eggli, I. K. Jin, J. Hillier, K. Kumar, I. Vorreiter, M. J. Rendell, J. Y. Huang, C. C. Escott, F. E. Hudson, W. H. Lim, D. Culcer, A. S. Dzurak, and A. R. Hamilton, "A singlet-triplet hole-spin qubit in mos silicon," *Nature Communications*, vol. 15, no. 1, Sep 2024. [Online]. Available: http://dx.doi.org/10.1038/s41467-024-51902-9

[58] N. Piot, B. Brun, V. Schmitt, S. Zihlmann, V. Michal, A. Apra, J. Abadillo-Uriel, X. Jehl, B. Bertrand, H. Niebojewski *et al.*, "A single hole spin with enhanced coherence in natural silicon," *Nature Nanotechnology*, vol. 17, no. 10, pp. 1072–1077, 2022.

[59] M. Janík, K. Roux, C. B. Espinosa, O. Sagi, A. Baghdadi, T. Adletzberger, S. Calcaterra, M. Botifoll, A. G. Manjón, J. Arbiol, D. Chrastina, G. Isella, I. M. Pop, and G. Katsaros, "Strong charge-photon coupling in planar germanium enabled by granular aluminium superinductors," 2024. [Online]. Available: https://arxiv.org/abs/2407.03079

[60] N. Hendrickx, L. Massai, M. Mergenthaler, F. Schupp, S. Paredes, S. Bedell, G. Salis, and A. Fuhrer, "Sweet-spot operation of a germanium hole

spin qubit with highly anisotropic noise sensitivity," *Nature Materials*, pp. 1–8, 2024.

[61] Z. Wang, E. Marcellina, A. R. Hamilton, J. H. Cullen, S. Rogge, J. Salfi, and D. Culcer, "Optimal operation points for ultrafast, highly coherent ge hole spin-orbit qubits," *npj Quantum Information*, vol. 7, p. 54, 2021. [Online]. Available: https://doi.org/10.1038/s41534-021-00386-2

[62] S. Bosco, B. Hetényi, and D. Loss, "Hole spin qubits in Si finfets with fully tunable spin-orbit coupling and sweet spots for charge noise," *PRX Quantum*, vol. 2, p. 010348, Mar 2021. [Online]. Available: https://link.aps.org/doi/10.1103/PRXQuantum.2.010348

[63] J. M. Elzerman, R. Hanson, L. H. W. van Beveren, B. Witkamp, L. M. K. Vandersypen, and L. P. Kouwenhoven, "Single-shot read-out of an individual electron spin in a quantum dot," *Nature*, vol. 430, pp. 431–435, 2004. [Online]. Available: https://doi.org/10.1038/nature02693

[64] C. H. Yang, A. Rossi, R. Ruskov, N. S. Lai, F. A. Mohiyaddin, S. Lee, C. Tahan, G. Klimeck, A. Morello, and A. S. Dzurak, "Spin-valley lifetimes in a silicon quantum dot with tunable valley splitting," *Nature Communications*, vol. 4, no. 1, pp. 1–8, 2013.

[65] P. Harvey-Collard, N. T. Jacobson, C. Bureau-Oxton, R. M. Jock, V. Srinivasa, A. M. Mounce, D. R. Ward, J. M. Anderson, R. P. Manginell, J. R. Wendt, T. Pluym, M. P. Lilly, D. R. Luhman, M. Pioro-Ladrière, and M. S. Carroll, "Spin-orbit interactions for singlet-triplet qubits in silicon," *Phys. Rev. Lett.*, vol. 122, p. 217702, May 2019. [Online]. Available: https://link.aps.org/doi/10.1103/PhysRevLett.122.217702

[66] A. D. Greentree, J. H. Cole, A. R. Hamilton, and L. C. L. Hollenberg, "Coherent electronic transfer in quantum dot systems using adiabatic passage," *Physical Review B*, vol. 70, no. 23, p. 235317, 2004.

[67] G. Oakes, V. Ciriano-Tejel, D. Wise, M. Fogarty, T. Lundberg, C. Lainé, S. Schaal, F. Martins, D. Ibberson, L. Hutin *et al.*, "Fast high-fidelity single-shot readout of spins in silicon using a single-electron box," *Physical Review X*, vol. 13, no. 1, p. 011023, 2023.

[68] C. Jones, M. A. Fogarty, A. Morello, M. F. Gyure, A. S. Dzurak, and T. D. Ladd, "Logical qubit in a linear array of semiconductor quantum dots," *Phys. Rev. X*, vol. 8, p. 021058, Jun 2018. [Online]. Available: https://link.aps.org/doi/10.1103/PhysRevX.8.021058

[69] Z. Cai, M. A. Fogarty, S. Schaal, S. Patomäki, S. C. Benjamin, and J. J. Morton, "A silicon surface code architecture resilient against leakage errors," *Quantum*, vol. 3, p. 212, 2019.

[70] A. E. Seedhouse, T. Tanttu, R. C. Leon, R. Zhao, K. Y. Tan, B. Hensen, F. E. Hudson, K. M. Itoh, J. Yoneda, C. H. Yang, A. Morello, A. Laucht, S. N. Coppersmith, A. Saraiva, and A. S. Dzurak, "Pauli blockade in silicon quantum dots with spin-orbit control," *PRX Quantum*, vol. 2, p. 010303, Jan 2021. [Online]. Available: https://link.aps.org/doi/10.1103/PRXQuantum.2.010303

[71] D. V. Averin and K. K. Likharev, "Coulomb blockade of single-electron tunneling, and coherent oscillations in small tunnel junctions," *Journal of Low Temperature Physics*, vol. 62, pp. 345–373, 1986. [Online]. Available: https://doi.org/10.1007/BF00683469

[72] T. A. Fulton and G. J. Dolan, "Observation of single-electron charging effects in small tunnel junctions," *Phys. Rev. Lett.*, vol. 59, pp. 109–112, Jul 1987. [Online]. Available: https://link.aps.org/doi/10.1103/PhysRevLett.59.109

[73] L. Vandersypen, J. Elzerman, R. Schouten, L. Willems van Beveren, R. Hanson, and L. Kouwenhoven, "Real-time detection of single-electron tunneling using a quantum point contact," *Applied Physics Letters*, vol. 85, no. 19, pp. 4394–4396, 2004.

[74] A. Morello, J. J. Pla, F. A. Zwanenburg, K. W. Chan, K. Y. Tan, H. Huebl, M. Möttönen, C. D. Nugroho, C. Yang, J. A. Van Donkelaar *et al.*, "Single-shot readout of an electron spin in silicon," *Nature*, vol. 467, no. 7316, pp. 687–691, 2010.

[75] S. J. Angus, A. J. Ferguson, A. S. Dzurak, and R. G. Clark, "A silicon radio-frequency single electron transistor," *Applied Physics Letters*, vol. 92, no. 11, p. 112103, Mar 2008. [Online]. Available: https://doi.org/10.1063/1.2831664

[76] C. Barthel, D. J. Reilly, C. M. Marcus, M. P. Hanson, and A. C. Gossard, "Rapid single-shot measurement of a singlet-triplet qubit," *Phys. Rev. Lett.*, vol. 103, p. 160503, Oct 2009. [Online]. Available: https://link.aps.org/doi/10.1103/PhysRevLett.103.160503

[77] T. Nakajima, M. R. Delbecq, T. Otsuka, P. Stano, S. Amaha, J. Yoneda, A. Noiri, K. Kawasaki, K. Takeda, G. Allison *et al.*, "Robust single-shot spin measurement with 99.5% fidelity in a quantum dot array," *Physical review letters*, vol. 119, no. 1, p. 017701, 2017.

[78] A. Mills, C. Guinn, M. Feldman, A. Sigillito, M. Gullans, M. Rakher, J. Kerckhoff, C. Jackson, and J. Petta, "High-fidelity state preparation, quantum control, and readout of an isotopically enriched silicon spin qubit," *Phys. Rev. Appl.*, vol. 18, p. 064028, Dec 2022. [Online]. Available: https://link.aps.org/doi/10.1103/PhysRevApplied.18.064028

[79] M. Urdampilleta, D. J. Niegemann, E. Chanrion, B. Jadot, C. Spence, P.-A. Mortemousque, C. Bäuerle, L. Hutin, B. Bertrand, S. Barraud, R. Maurand, M. Sanquer, X. Jehl, S. D. Franceschi, M. Vinet, and T. Meunier, "Gate-based high fidelity spin readout in a cmos device," *Nature Nanotechnology*, vol. 14, pp. 737–741, 2019. [Online]. Available: https://doi.org/10.1038/s41565-019-0443-9

[80] A. West, B. Hensen, A. Jouan, T. Tanttu, C.-H. Yang, A. Rossi, M. F. Gonzalez-Zalba, F. Hudson, A. Morello, D. J. Reilly, and A. S. Dzurak, "Gate-based single-shot readout of spins in silicon," *Nature Nanotechnology*, vol. 14, pp. 437–441, 2019. [Online]. Available: https://doi.org/10.1038/s41565-019-0400-7

[81] P. Pakkiam, A. V. Timofeev, M. G. House, M. R. Hogg, T. Kobayashi, M. Koch, S. Rogge, and M. Y. Simmons, "Single-shot single-gate rf spin readout in silicon," *Phys. Rev. X*, vol. 8, p. 041032, Nov 2018. [Online]. Available: https://link.aps.org/doi/10.1103/PhysRevX.8.041032

[82] G. Zheng, N. Samkharadze, M. L. Noordam, N. Kalhor, D. Brousse, A. Sammak, G. Scappucci, and L. M. K. Vandersypen, "Rapid gate-based spin read-out in silicon using an on-chip resonator," *Nature Nanotechnology*, vol. 14, pp. 742–746, 2019. [Online]. Available: https://doi.org/10.1038/s41565-019-0488-9

[83] J. Yoneda, K. Takeda, A. Noiri, T. Nakajima, S. Li, J. Kamioka, T. Kodera, and S. Tarucha, "Quantum non-demolition readout of an electron spin in silicon," *Nature communications*, vol. 11, no. 1, p. 1144, 2020.

[84] X. Xue, B. D'Anjou, T. F. Watson, D. R. Ward, D. E. Savage, M. G. Lagally, M. Friesen, S. N. Coppersmith, M. A. Eriksson, W. A. Coish, and L. M. K. Vandersypen, "Repetitive quantum nondemolition measurement and soft decoding of a silicon spin qubit," *Phys. Rev. X*, vol. 10, p. 021006, Apr 2020. [Online]. Available: https://link.aps.org/doi/10.1103/PhysRevX.10.021006

[85] I. Hansen, A. E. Seedhouse, S. Serrano, A. Nickl, M. Feng, J. Y. Huang, T. Tanttu, N. D. Stuyck, W. H. Lim, F. E. Hudson, K. M. Itoh, A. Saraiva, A. Laucht, A. S. Dzurak, and C. H. Yang, "Entangling gates on degenerate spin qubits dressed by a global field," *Nature Communications*, vol. 15, p. 7656, 2024. [Online]. Available: https://doi.org/10.1038/s41467-024-52010-4

[86] R. Leon, C. H. Yang, J. Hwang, J. C. Lemyre, T. Tanttu, W. Huang, K. W. Chan, K. Tan, F. Hudson, K. Itoh *et al.*, "Coherent spin control of s-, p-, d-and f-electrons in a silicon quantum dot," *Nature communications*, vol. 11, no. 1, p. 797, 2020.

[87] J. Yoneda, K. Takeda, T. Otsuka, T. Nakajima, M. R. Delbecq, G. Allison, T. Honda, T. Kodera, S. Oda, Y. Hoshi *et al.*, "A quantum-dot spin qubit with coherence limited by charge noise and fidelity higher than 99.9%," *Nature Nanotechnology*, vol. 13, no. 2, pp. 102–106, 2018.

[88] R. Maurand, X. Jehl, D. Kotekar-Patil, A. Corna, H. Bohuslavskyi, R. Laviéville, L. Hutin, S. Barraud, M. Vinet, M. Sanquer *et al.*, "A cmos silicon spin qubit," *Nature communications*, vol. 7, no. 1, p. 13575, 2016.

[89] C.-A. Wang, V. John, H. Tidjani, C. X. Yu, A. S. Ivlev, C. Déprez, F. van Riggelen-Doelman, B. D. Woods, N. W. Hendrickx, W. I. Lawrie *et al.*, "Operating semiconductor quantum processors with hopping spins," *Science*, vol. 385, no. 6707, pp. 447–452, 2024.

[90] B. Undseth, X. Xue, M. Mehmandoost, M. Rimbach-Russ, P. T. Eendebak, N. Samkharadze, A. Sammak, V. V. Dobrovitski, G. Scappucci, and L. M. Vandersypen, "Nonlinear response and crosstalk of electrically driven silicon spin qubits," *Phys. Rev. Appl.*, vol. 19, p. 044078, Apr 2023. [Online]. Available: https://link.aps.org/doi/10.1103/PhysRevApplied.19.044078

[91] S. K. Bartee, W. Gilbert, K. Zuo, K. Das, T. Tanttu, C. H. Yang, N. D. Stuyck, S. J. Pauka, R. Y. Su, W. H. Lim *et al.*, "Spin qubits with scalable milli-kelvin cmos control," *arXiv preprint arXiv:2407.15151*, 2024.

[92] D. M. Zajac, A. J. Sigillito, M. Russ, F. Borjans, J. M. Taylor, G. Burkard, and J. R. Petta, "Resonantly driven cnot gate for electron spins," *Science*, vol. 359, no. 6374, pp. 439–442, 2018. [Online]. Available: https://www.science.org/doi/abs/10.1126/science.aao5965

[93] X. Xue, M. Russ, N. Samkharadze, B. Undseth, A. Sammak, G. Scappucci, and L. M. Vandersypen, "Quantum logic with spin qubits crossing the surface code threshold," *Nature*, vol. 601, no. 7893, pp. 343–347, 2022.

[94] P. K. Day, H. G. LeDuc, B. A. Mazin, A. Vayonakis, and J. Zmuidzinas, "A broadband superconducting detector suitable for use in large arrays," *Nature*, vol. 425, no. 6960, pp. 817–821, 2003.

[95] M. Castellanos-Beltran and K. Lehnert, "Widely tunable parametric amplifier based on a superconducting quantum interference device array resonator," *Applied Physics Letters*, vol. 91, no. 8, 2007.

[96] D. J. Parker, M. Savytskyi, W. Vine, A. Laucht, T. Duty, A. Morello, A. L. Grimsmo, and J. J. Pla, "Degenerate parametric amplification via three-wave mixing using kinetic inductance," *Physical Review Applied*, vol. 17, no. 3, p. 034064, 2022.

[97] A. Blais, R.-S. Huang, and A. Wallraff, "Cavity quantum electrodynamics for superconducting electrical circuits: An architecture for quantum computation," *Physical Review A—Atomic, Molecular, and Optical Physics*, vol. 69, no. 6, p. 062320, 2004.

[98] M. Göppl, A. Fragner, M. Baur, R. Bianchetti, S. Filipp, J. M. Fink, P. J. Leek, G. Puebla, L. Steffen, and A. Wallraff, "Coplanar waveguide resonators for circuit quantum electrodynamics," *Journal of Applied Physics*, vol. 104, no. 11, 2008.

[99] C. Wen, "Coplanar waveguide, a surface strip transmission line suitable for nonreciprocal gyromagnetic device applications," in *1969 G-MTT International Microwave Symposium*, 1969, pp. 110–115.

[100] A. Blais, A. L. Grimsmo, S. M. Girvin, and A. Wallraff, "Circuit quantum electrodynamics," *Rev. Mod. Phys.*, vol. 93, p. 025005, May 2021.

[101] R. Simons, *Coplanar Waveguide Circuits, Components and Systems*. Wiley, Jan 2001.

[102] P. Anderson, "Theory of dirty superconductors," *Journal of Physics and Chemistry of Solids*, vol. 11, no. 1, pp. 26–30, 1959. [Online]. Available: https://www.sciencedirect.com/science/article/pii/0022369759900368

[103] A. Stockklauser, P. Scarlino, J. V. Koski, S. Gasparinetti, C. K. Andersen, C. Reichl, W. Wegscheider, T. Ihn, K. Ensslin, and A. Wallraff, "Strong coupling cavity qed with gate-defined double quantum dots enabled by a high impedance resonator," *Phys. Rev. X*, vol. 7, p. 011030, Mar 2017. [Online]. Available: https://link.aps.org/doi/10.1103/PhysRevX.7.011030

[104] M. Tinkham, *Introduction to Superconductivity*. Dover Publications, 2004.

[105] N. Samkharadze, A. Bruno, P. Scarlino, G. Zheng, D. P. DiVincenzo, L. DiCarlo, and L. M. K. Vandersypen, "High-kinetic-inductance superconducting nanowire resonators for circuit qed in a magnetic field," *Physical Review Applied*, vol. 5, p. 044004, Apr 2016. [Online]. Available: https://link.aps.org/doi/10.1103/PhysRevApplied.5.044004

[106] C. X. Yu, S. Zihlmann, G. T. Fernández-Bada, J.-L. Thomassin, F. Gustavo, Étienne Dumur, and R. Maurand, "Magnetic field resilient high kinetic inductance superconducting niobium nitride coplanar waveguide resonators," *Applied Physics Letters*, vol. 118, p. 054001, Feb 2021. [Online]. Available: https://doi.org/10.1063/5.0039945

[107] P. Harvey-Collard, G. Zheng, J. Dijkema, N. Samkharadze, A. Sammak, G. Scappucci, and L. M. K. Vandersypen, "On-chip microwave filters for high-impedance resonators with gate-defined quantum dots," *Physical Review Applied*, vol. 14, p. 034025, Sep 2020. [Online]. Available: https://link.aps.org/doi/10.1103/PhysRevApplied.14.034025

[108] J. L. O'Brien, H. Nakagawa, A. S. Dzurak, R. G. Clark, B. E. Kane, N. E. Lumpkin, R. P. Starrett, N. Muira, E. E. Mitchell, J. D. Goettee, D. G. Rickel, and J. S. Brooks, "Experimental determination of the $b-t$ phase diagram of $\mathrm{yba_2cu_3o_{7-\delta}}$ to 150 t for B $\perp$ c," *Phys. Rev. B*, vol. 61, pp. 1584–1587, Jan 2000. [Online]. Available: https://link.aps.org/doi/10.1103/PhysRevB.61.1584

[109] K. Borisov, D. Rieger, P. Winkel, F. Henriques, F. Valenti, A. Ionita, M. Wessbecher, M. Spiecker, D. Gusenkova, I. M. Pop, and W. Wernsdorfer, "Superconducting granular aluminum resonators resilient to magnetic fields up to 1 tesla," *Applied Physics Letters*, vol. 117, p. 120502, Sep 2020. [Online]. Available: http://aip.scitation.org/doi/10.1063/5.0018012

[110] A. J. Landig, J. V. Koski, P. Scarlino, U. Mendes, A. Blais, C. Reichl, W. Wegscheider, A. Wallraff, K. Ensslin, and T. Ihn, "Coherent spin–photon coupling using a resonant exchange qubit," *Nature*, vol. 560, no. 7717, pp. 179–184, 2018.

[111] L. Grünhaupt, M. Spiecker, D. Gusenkova, N. Maleeva, S. T. Skacel, I. Takmakov, F. Valenti, P. Winkel, H. Rotzinger, W. Wernsdorfer, A. V. Ustinov, and I. M. Pop, "Granular aluminium as a superconducting material for high-impedance quantum circuits,"

Nature Materials, vol. 18, pp. 816–819, 2019. [Online]. Available: https://doi.org/10.1038/s41563-019-0350-3

[112] N. Maleeva, L. Grünhaupt, T. Klein, F. Levy-Bertrand, O. Dupre, M. Calvo, F. Valenti, P. Winkel, F. Friedrich, W. Wernsdorfer, A. V. Ustinov, H. Rotzinger, A. Monfardini, M. V. Fistul, and I. M. Pop, "Circuit quantum electrodynamics of granular aluminum resonators," *Nature Communications*, vol. 9, p. 3889, 2018. [Online]. Available: https://doi.org/10.1038/s41467-018-06386-9

[113] H. Rotzinger, S. T. Skacel, M. Pfirrmann, J. N. Voss, J. Münzberg, S. Probst, P. Bushev, M. P. Weides, A. V. Ustinov, and J. E. Mooij, "Aluminium-oxide wires for superconducting high kinetic inductance circuits," *Superconductor Science and Technology*, vol. 30, p. 025002, Feb 2017. [Online]. Available: https://iopscience.iop.org/article/10.1088/0953-2048/30/2/025002

[114] V. Singh, B. H. Schneider, S. J. Bosman, E. P. J. Merkx, and G. A. Steele, "Molybdenum-rhenium alloy based high-Q superconducting microwave resonators," *Applied Physics Letters*, vol. 105, no. 22, p. 222601, Dec 2014. [Online]. Available: https://doi.org/10.1063/1.4903042

[115] K. J. G. Götz, S. Blien, P. L. Stiller, O. Vavra, T. Mayer, T. Huber, T. N. G. Meier, M. Kronseder, C. Strunk, and A. K. Hüttel, "Co-sputtered more thin films for carbon nanotube growth-compatible superconducting coplanar resonators," *Nanotechnology*, vol. 27, no. 13, p. 135202, Feb 2016. [Online]. Available: https://dx.doi.org/10.1088/0957-4484/27/13/135202

[116] J. Larson and T. Mavrogordatos, *The Jaynes–Cummings Model and Its Descendants*, ser. 2053-2563. IOP Publishing, 2021.

[117] E. T. Jaynes and F. W. Cummings, "Comparison of quantum and semi-classical radiation theories with application to the beam maser," *Proceedings of the IEEE*, vol. 51, no. 1, pp. 89–109, 1963.

[118] P. Harvey-Collard, J. Dijkema, G. Zheng, A. Sammak, G. Scappucci, and L. M. K. Vandersypen, "Coherent spin-spin coupling mediated by virtual microwave photons," *Physical Review X*, vol. 12, p. 021026, May 2022. [Online]. Available: https://link.aps.org/doi/10.1103/PhysRevX.12.021026

[119] F. Borjans, X. G. Croot, X. Mi, M. J. Gullans, and J. R. Petta, "Resonant microwave-mediated interactions between distant electron spins," *Nature*, vol. 577, no. 7789, pp. 195–198, 2020. [Online]. Available: https://doi.org/10.1038/s41586-019-1867-y

[120] J. Dijkema, X. Xue, P. Harvey-Collard, M. Rimbach-Russ, S. L. de Snoo, G. Zheng, A. Sammak, G. Scappucci, and L. M. K. Vandersypen, "Two-qubit logic between distant spins in silicon," 2023. [Online]. Available: https://arxiv.org/abs/2310.16805

[121] A. Laucht, J. T. Muhonen, F. A. Mohiyaddin, R. Kalra, J. P. Dehollain, S. Freer, F. E. Hudson, M. Veldhorst, R. Rahman, G. Klimeck, K. M. Itoh, D. N. Jamieson, J. C. McCallum, A. S. Dzurak, and A. Morello, "Electrically controlling single-spin qubits in a continuous microwave field," *Science Advances*, vol. 1, no. 3, p. e1500022, 2015. [Online]. Available: https://www.science.org/doi/abs/10.1126/sciadv.1500022

[122] A. Laucht, R. Kalra, S. Simmons, J. P. Dehollain, J. T. Muhonen, F. A. Mohiyaddin, S. Freer, F. E. Hudson, K. M. Itoh, D. N. Jamieson, J. C. McCallum, A. S. Dzurak, and A. Morello, "A dressed spin qubit in silicon," *Nature Nanotechnology*, vol. 12, pp. 61–66, 2017. [Online]. Available: https://doi.org/10.1038/nnano.2016.178

[123] A. E. Seedhouse, I. Hansen, A. Laucht, C. H. Yang, A. S. Dzurak, and A. Saraiva, "Quantum computation protocol for dressed spins in a global field," *Phys. Rev. B*, vol. 104, p. 235411, Dec 2021. [Online]. Available: https://link.aps.org/doi/10.1103/PhysRevB.104.235411

[124] I. Hansen, A. E. Seedhouse, A. Saraiva, A. Laucht, A. S. Dzurak, and C. H. Yang, "Pulse engineering of a global field for robust and universal quantum computation," *Physical Review A*, vol. 104, no. 6, p. 062415, 2021.

[125] I. Hansen, A. E. Seedhouse, A. Saraiva, A. S. Dzurak, and C. H. Yang, "Accessing the full capabilities of filter functions: Tool for detailed noise and quantum control susceptibility analysis," *Phys. Rev. A*, vol. 108, p. 012426, Jul 2023. [Online]. Available: https://link.aps.org/doi/10.1103/PhysRevA.108.012426

[126] F. J. Rosenbaum, "Dielectric cavity resonator for esr experiments," *Review of Scientific Instruments*, vol. 35, no. 11, pp. 1550–1554, Nov 1964. [Online]. Available: https://doi.org/10.1063/1.1719205

[127] A. Blank, E. Stavitski, H. Levanon, and F. Gubaydullin, "Transparent miniature dielectric resonator for electron paramagnetic resonance experiments," *Review of scientific instruments*, vol. 74, no. 5, pp. 2853–2859, 2003.

[128] M. Jaworski, A. Sienkiewicz, and C. P. Scholes, "Double-stacked dielectric resonator for sensitive epr measurements," *Journal of Magnetic Resonance*, vol. 124, no. 1, pp. 87–96, 1997.

[129] R. G. Geyer, B. Riddle, J. Krupka, and L. A. Boatner, "Microwave dielectric properties of single-crystal quantum paraelectrics ktao3 and srtio3 at cryogenic temperatures," *Journal of Applied Physics*, vol. 97, no. 10, 2005.

[130] E. A. J. Marcatili, "Dielectric rectangular waveguide and directional coupler for integrated optics," *The Bell System Technical Journal*, vol. 48, no. 7, pp. 2071–2102, 1969.

[131] R. Kumar Mongia and A. Ittipiboon, "Theoretical and experimental investigations on rectangular dielectric resonator antennas," *IEEE Transactions on Antennas and Propagation*, vol. 45, no. 9, pp. 1348–1356, 1997.

[132] E. Nielsen, J. K. Gamble, K. Rudinger, T. Scholten, K. Young, and R. Blume-Kohout, "Gate Set Tomography," *Quantum*, vol. 5, p. 557, Oct 2021. [Online]. Available: https://doi.org/10.22331/q-2021-10-05-557

[133] R. Blume-Kohout, J. K. Gamble, E. Nielsen, J. Mizrahi, J. D. Sterk, and P. Maunz, "Robust, self-consistent, closed-form tomography of quantum logic gates on a trapped ion qubit," 2013. [Online]. Available: https://arxiv.org/abs/1310.4492

[134] J. P. Dehollain, J. T. Muhonen, R. Blume-Kohout, K. M. Rudinger, J. K. Gamble, E. Nielsen, A. Laucht, S. Simmons, R. Kalra, A. S. Dzurak, and A. Morello, "Optimization of a solid-state electron spin qubit using gate set tomography," *New Journal of*

Physics, vol. 18, no. 10, p. 103018, Oct 2016. [Online]. Available: https://dx.doi.org/10.1088/1367-2630/18/10/103018

[135] H. G. Stemp, S. Asaad, M. R. van Blankenstein, A. Vaartjes, M. A. I. Johnson, M. T. Mądzik, A. J. A. Heskes, H. R. Firgau, R. Y. Su, C. H. Yang, A. Laucht, C. I. Ostrove, K. M. Rudinger, K. Young, R. Blume-Kohout, F. E. Hudson, A. S. Dzurak, K. M. Itoh, A. M. Jakob, B. C. Johnson, D. N. Jamieson, and A. Morello, "Tomography of entangling two-qubit logic operations in exchange-coupled donor electron spin qubits," *Nature Communications*, vol. 15, p. 8415, 2024. [Online]. Available: https://doi.org/10.1038/s41467-024-52795-4

[136] W. Huang, M. Veldhorst, N. M. Zimmerman, A. S. Dzurak, and D. Culcer, "Electrically driven spin qubit based on valley mixing," *Physical Review B*, vol. 95, no. 7, p. 075403, 2017.

[137] T. Tanttu, B. Hensen, K. W. Chan, C. H. Yang, W. W. Huang, M. Fogarty, F. Hudson, K. Itoh, D. Culcer, A. Laucht *et al.*, "Controlling spin-orbit interactions in silicon quantum dots using magnetic field direction," *Physical Review X*, vol. 9, no. 2, p. 021028, 2019.

[138] E. Kawakami, T. Jullien, P. Scarlino, D. R. Ward, D. E. Savage, M. G. Lagally, V. V. Dobrovitski, M. Friesen, S. N. Coppersmith, M. A. Eriksson, and L. M. K. Vandersypen, "Gate fidelity and coherence of an electron spin in an si/sige quantum dot with micromagnet," *Proceedings of the National Academy of Sciences*, vol. 113, no. 42, pp. 11 738–11 743, 2016. [Online]. Available: https://www.pnas.org/doi/abs/10.1073/pnas.1603251113

[139] X. Wu, D. R. Ward, J. R. Prance, D. Kim, J. K. Gamble, R. T. Mohr, Z. Shi, D. E. Savage, M. G. Lagally, M. Friesen, S. N. Coppersmith, and M. A. Eriksson, "Two-axis control of a singlet–triplet qubit with an integrated micromagnet," *Proceedings of the National Academy of Sciences*, vol. 111, no. 33, pp. 11 938–11 942, 2014. [Online]. Available: https://www.pnas.org/doi/abs/10.1073/pnas.1412230111

[140] M. K. Feng, J. Yoneda, W. Huang, Y. Su, T. Tanttu, C. H. Yang, J. D. Cifuentes, K. W. Chan, W. Gilbert, R. C. C. Leon, F. E. Hudson, K. M. Itoh, A. Laucht, A. S. Dzurak, and A. Saraiva, "Control of dephasing in spin qubits during coherent transport in silicon," *Phys. Rev. B*, vol. 107, p. 085427, Feb 2023.

[141] M. Russ, F. Ginzel, and G. Burkard, "Coupling of three-spin qubits to their electric environment," *Phys. Rev. B*, vol. 94, p. 165411, Oct 2016. [Online]. Available: https://link.aps.org/doi/10.1103/PhysRevB.94.165411

[142] A. Saraiva, W. H. Lim, C. H. Yang, C. C. Escott, A. Laucht, and A. S. Dzurak, "Materials for silicon quantum dots and their impact on electron spin qubits," *Advanced Functional Materials*, vol. 32, no. 3, p. 2105488, 2022.

[143] K. W. Chan, W. Huang, C. H. Yang, J. C. C. Hwang, B. Hensen, T. Tanttu, F. E. Hudson, K. M. Itoh, A. Laucht, A. Morello, and A. S. Dzurak, "Assessment of a silicon quantum dot spin qubit environment via noise spectroscopy," *Phys. Rev. Appl.*, vol. 10, p. 044017, Oct 2018.

[144] J. D. Cifuentes, T. Tanttu, P. Steinacker, S. Serrano, I. Hansen, J. P. Slack-Smith, W. Gilbert, J. Y. Huang, E. Vahapoglu, R. C. Leon *et al.*,

"Impact of electrostatic crosstalk on spin qubits in dense cmos quantum dot arrays," *Physical Review B*, vol. 110, no. 12, p. 125414, 2024.

[145] A. Imamoğlu, "Cavity qed based on collective magnetic dipole coupling: Spin ensembles as hybrid two-level systems," *Phys. Rev. Lett.*, vol. 102, p. 083602, Feb 2009. [Online]. Available: https://link.aps.org/doi/10.1103/PhysRevLett.102.083602

[146] J. Corrigan, B. Harpt, N. Holman, R. Ruskov, P. Marciniec, D. Rosenberg, D. Yost, R. Das, W. D. Oliver, R. McDermott, C. Tahan, M. Friesen, and M. A. Eriksson, "Longitudinal coupling between a si/si$_{1-x}$ge$_x$ double quantum dot and an off-chip TiN resonator," *Phys. Rev. Appl.*, vol. 20, p. 064005, Dec 2023. [Online]. Available: https://link.aps.org/doi/10.1103/PhysRevApplied.20.064005

[147] F. Borjans, X. Croot, S. Putz, X. Mi, S. M. Quinn, A. Pan, J. Kerckhoff, E. J. Pritchett, C. A. Jackson, L. F. Edge, R. S. Ross, T. D. Ladd, M. G. Borselli, M. F. Gyure, and J. R. Petta, "Split-gate cavity coupler for silicon circuit quantum electrodynamics," *Applied Physics Letters*, vol. 116, p. 234001, Jun 2020. [Online]. Available: http://aip.scitation.org/doi/10.1063/5.0006442

[148] F. Martins, F. K. Malinowski, P. D. Nissen, E. Barnes, S. Fallahi, G. C. Gardner, M. J. Manfra, C. M. Marcus, and F. Kuemmeth, "Noise suppression using symmetric exchange gates in spin qubits," *Phys. Rev. Lett.*, vol. 116, p. 116801, Mar 2016. [Online]. Available: https://link.aps.org/doi/10.1103/PhysRevLett.116.116801

[149] M. D. Reed, B. M. Maune, R. W. Andrews, M. G. Borselli, K. Eng, M. P. Jura, A. A. Kiselev, T. D. Ladd, S. T. Merkel, I. Milosavljevic,

E. J. Pritchett, M. T. Rakher, R. S. Ross, A. E. Schmitz, A. Smith, J. A. Wright, M. F. Gyure, and A. T. Hunter, "Reduced sensitivity to charge noise in semiconductor spin qubits via symmetric operation," *Phys. Rev. Lett.*, vol. 116, p. 110402, Mar 2016. [Online]. Available: https://link.aps.org/doi/10.1103/PhysRevLett.116.110402

[150] R. Ruskov and C. Tahan, "Modulated longitudinal gates on encoded spin qubits via curvature couplings to a superconducting cavity," *Phys. Rev. B*, vol. 103, p. 035301, Jan 2021. [Online]. Available: https://link.aps.org/doi/10.1103/PhysRevB.103.035301

[151] A. Bienfait, J. J. Pla, Y. Kubo, X. Zhou, M. Stern, C. C. Lo, C. D. Weis, T. Schenkel, D. Vion, D. Esteve, J. J. L. Morton, and P. Bertet, "Controlling spin relaxation with a cavity," *Nature*, vol. 531, pp. 74–77, 2016. [Online]. Available: https://doi.org/10.1038/nature16944

[152] H. Yan, X. Wu, A. Lingenfelter, Y. J. Joshi, G. Andersson, C. R. Conner, M.-H. Chou, J. Grebel, J. M. Miller, R. G. Povey, H. Qiao, A. A. Clerk, and A. N. Cleland, "Broadband bandpass Purcell filter for circuit quantum electrodynamics," *Applied Physics Letters*, vol. 123, no. 13, p. 134001, Sep 2023. [Online]. Available: https://doi.org/10.1063/5.0161893

[153] B. Harpt, J. Corrigan, N. Holman, P. Marciniec, D. Rosenberg, D. Yost, R. Das, R. Ruskov, C. Tahan, W. D. Oliver, R. McDermott, M. Friesen, and M. A. Eriksson, "Ultra-dispersive resonator readout of a quantum-dot qubit using longitudinal coupling," 2024. [Online]. Available: https://arxiv.org/abs/2407.08869

[154] S. Probst, F. B. Song, P. A. Bushev, A. V. Ustinov, and M. Weides, "Efficient and robust analysis of complex scattering data under noise in

microwave resonators," *Review of Scientific Instruments*, vol. 86, no. 2, p. 024706, Feb 2015.

[155] W. Vine, "Spin detection, amplification, and microwave squeezing with kinetic inductance parametric amplifiers," PhD thesis, University of New South Wales, Apr 2023.

[156] X. Mi, J. V. Cady, D. M. Zajac, J. Stehlik, L. F. Edge, and J. R. Petta, "Circuit quantum electrodynamics architecture for gate-defined quantum dots in silicon," *Applied Physics Letters*, vol. 110, no. 4, p. 043502, Jan 2017. [Online]. Available: https://doi.org/10.1063/1.4974536

[157] P. M. Tedrow and R. Meservey, "Critical magnetic field of very thin superconducting aluminum films," *Phys. Rev. B*, vol. 25, pp. 171–178, Jan 1982. [Online]. Available: https://link.aps.org/doi/10.1103/PhysRevB.25.171

[158] C. Reale, "Thickness and temperature dependence of the critical magnetic field of thin superconducting films of the aluminium group metals," *Acta Physica Academiae Scientiarum Hungaricae*, vol. 37, pp. 53–60, 1974. [Online]. Available: https://doi.org/10.1007/BF03157926

[159] R. Meservey and P. M. Tedrow, "Properties of very thin aluminum films," *Journal of Applied Physics*, vol. 42, no. 1, pp. 51–53, Jan 1971.

[160] C.-Y. Lee, Y. Liu, and T. Itoh, "The effects of the coupled slotline mode and air-bridges on cpw and nlc waveguide discontinuities," *IEEE Transactions on Microwave Theory and Techniques*, vol. 43, no. 12, pp. 2759–2765, 1995.

[161] N. Holman, D. Rosenberg, D. Yost, J. L. Yoder, R. Das, W. D. Oliver, R. McDermott, and M. A. Eriksson, "3d integration and measurement of a semiconductor double quantum dot with a high-impedance tin resonator," *npj Quantum Information*, vol. 7, p. 137, 2021. [Online]. Available: https://doi.org/10.1038/s41534-021-00469-0

[162] J. D. Cifuentes, T. Tanttu, W. Gilbert, J. Y. Huang, E. Vahapoglu, R. C. Leon, S. Serrano, D. Otter, D. Dunmore, P. Y. Mai *et al.*, "Bounds to electron spin qubit variability for scalable cmos architectures," *Nature Communications*, vol. 15, no. 1, p. 4299, 2024.

[163] E. J. Connors, J. J. Nelson, H. Qiao, L. F. Edge, and J. M. Nichol, "Low-frequency charge noise in si/sige quantum dots," *Physical Review B*, vol. 100, no. 16, p. 165305, 2019.

[164] W. Huang, C. H. Yang, K. W. Chan, T. Tanttu, B. Hensen, R. C. C. Leon, M. A. Fogarty, J. C. C. Hwang, F. E. Hudson, K. M. Itoh *et al.*, "Fidelity benchmarks for two-qubit gates in silicon," *Nature*, vol. 569, no. 7757, pp. 532–536, 2019.

[165] M. Baur, S. Filipp, R. Bianchetti, J. M. Fink, M. Göppl, L. Steffen, P. J. Leek, A. Blais, and A. Wallraff, "Measurement of autler-townes and mollow transitions in a strongly driven superconducting qubit," *Phys. Rev. Lett.*, vol. 102, p. 243602, Jun 2009. [Online]. Available: https://link.aps.org/doi/10.1103/PhysRevLett.102.243602

[166] I. Hansen, A. E. Seedhouse, K. W. Chan, F. Hudson, K. M. Itoh, A. Laucht, A. Saraiva, C. H. Yang, and A. S. Dzurak, "Implementation of an advanced dressing protocol for global qubit control in silicon," *Applied Physics Reviews*, vol. 9, no. 3, 2022.

[167] A. Laucht, S. Simmons, R. Kalra, G. Tosi, J. P. Dehollain, J. T. Muhonen, S. Freer, F. E. Hudson, K. M. Itoh, D. N. Jamieson, J. C. McCallum, A. S. Dzurak, and A. Morello, "Breaking the rotating wave approximation for a strongly driven dressed single-electron spin," *Phys. Rev. B*, vol. 94, p. 161302, Oct 2016. [Online]. Available: https://link.aps.org/doi/10.1103/PhysRevB.94.161302

[168] J. Zeng, C. H. Yang, A. S. Dzurak, and E. Barnes, "Geometric formalism for constructing arbitrary single-qubit dynamically corrected gates," *Phys. Rev. A*, vol. 99, p. 052321, May 2019. [Online]. Available: https://link.aps.org/doi/10.1103/PhysRevA.99.052321

[169] H. H. Vallabhapurapu, I. Hansen, C. Adambukulam, R. Stöhr, A. Denisenko, C. H. Yang, and A. Laucht, "High-fidelity control of a nitrogen-vacancy-center spin qubit at room temperature using the sinusoidally modulated, always rotating, and tailored protocol," *Phys. Rev. A*, vol. 108, p. 022606, Aug 2023. [Online]. Available: https://link.aps.org/doi/10.1103/PhysRevA.108.022606

[170] E. Nielsen, K. Rudinger, T. Proctor, A. Russo, K. Young, and R. Blume-Kohout, "Probing quantum processor performance with pygsti," *Quantum Science and Technology*, vol. 5, no. 4, p. 044002, Jul 2020. [Online]. Available: http://dx.doi.org/10.1088/2058-9565/ab8aa4

[171] M. T. Mądzik, S. Asaad, A. Youssry, B. Joecker, K. M. Rudinger, E. Nielsen, K. C. Young, T. J. Proctor, A. D. Baczewski, A. Laucht *et al.*, "Precision tomography of a three-qubit donor quantum processor in silicon," *Nature*, vol. 601, no. 7893, pp. 348–353, 2022.

[172] B. Undseth, O. Pietx-Casas, E. Raymenants, M. Mehmandoost, M. T. Mądzik, S. G. J. Philips, S. L. de Snoo, D. J. Michalak, S. V. Amitonov, L. Tryputen, B. P. Wuetz, V. Fezzi, D. D. Esposti, A. Sammak, G. Scappucci, and L. M. K. Vandersypen, "Hotter is easier: Unexpected temperature dependence of spin qubit frequencies," *Phys. Rev. X*, vol. 13, p. 041015, Oct 2023. [Online]. Available: https://link.aps.org/doi/10.1103/PhysRevX.13.041015

[173] S. Meiboom and D. Gill, "Modified Spin-Echo Method for Measuring Nuclear Relaxation Times," *Review of Scientific Instruments*, vol. 29, no. 8, pp. 688–691, Aug 1958. [Online]. Available: https://doi.org/10.1063/1.1716296

[174] H. Y. Carr and E. M. Purcell, "Effects of diffusion on free precession in nuclear magnetic resonance experiments," *Phys. Rev.*, vol. 94, pp. 630–638, May 1954. [Online]. Available: https://link.aps.org/doi/10.1103/PhysRev.94.630

[175] J. Bylander, S. Gustavsson, F. Yan, F. Yoshihara, K. Harrabi, G. Fitch, D. G. Cory, Y. Nakamura, J.-S. Tsai, and W. D. Oliver, "Noise spectroscopy through dynamical decoupling with a superconducting flux qubit," *Nature Physics*, vol. 7, pp. 565–570, 2011. [Online]. Available: https://doi.org/10.1038/nphys1994

[176] L. Cywiński, R. M. Lutchyn, C. P. Nave, and S. Das Sarma, "How to enhance dephasing time in superconducting qubits," *Phys. Rev. B*, vol. 77, p. 174509, May 2008. [Online]. Available: https://link.aps.org/doi/10.1103/PhysRevB.77.174509

[177] F. Yan, S. Gustavsson, J. Bylander, X. Jin, F. Yoshihara, D. G. Cory, Y. Nakamura, T. P. Orlando, and W. D. Oliver, "Rotating-frame relaxation as a noise spectrum analyser of a superconducting qubit undergoing driven evolution," *Nature Communications*, vol. 4, p. 2337, 2013. [Online]. Available: https://doi.org/10.1038/ncomms3337

[178] J. H. Bodey, R. Stockill, E. V. Denning, D. A. Gangloff, G. Éthier Majcher, D. M. Jackson, E. Clarke, M. Hugues, C. L. Gall, and M. Atatüre, "Optical spin locking of a solid-state qubit," *npj Quantum Information*, vol. 5, p. 95, 2019. [Online]. Available: https://doi.org/10.1038/s41534-019-0206-3

[179] T. Nakajima, A. Noiri, K. Kawasaki, J. Yoneda, P. Stano, S. Amaha, T. Otsuka, K. Takeda, M. R. Delbecq, G. Allison, A. Ludwig, A. D. Wieck, D. Loss, and S. Tarucha, "Coherence of a driven electron spin qubit actively decoupled from quasistatic noise," *Phys. Rev. X*, vol. 10, p. 011060, Mar 2020. [Online]. Available: https://link.aps.org/doi/10.1103/PhysRevX.10.011060

[180] S. Liles, D. Miserev, A. Kiselev, I. Thorvaldson, M. Rendell, I. Jin, F. Hudson, K. Itoh *et al.*, "Electrical control of the g tensor of the first hole in a silicon mos quantum dot," *Physical Review B*, vol. 104, no. 23, p. 235303, 2021.

[181] O. Malkoc, P. Stano, and D. Loss, "Charge-noise-induced dephasing in silicon hole-spin qubits," *Phys. Rev. Lett.*, vol. 129, p. 247701, Dec 2022. [Online]. Available: https://link.aps.org/doi/10.1103/PhysRevLett.129.247701

[182] I. K. Jin, J. Hillier, S. D. Liles, Z. Wang, A. Shamim, I. Vorreiter, R. Li, C. Godfrin, S. Kubicek, K. De Greve *et al.*, "Probing g-tensor reproducibility and spin-orbit effects in planar silicon hole quantum dots," *arXiv preprint arXiv:2411.06016*, 2024.

[183] P. Harvey-Collard, J. Dijkema, G. Zheng, A. Sammak, G. Scappucci, and L. M. K. Vandersypen, "Coherent spin-spin coupling mediated by virtual microwave photons," *Physical Review X*, vol. 12, no. 2, p. 021026, 2022.

[184] H. C. George, M. T. Mądzik, E. M. Henry, A. J. Wagner, M. M. Islam, F. Borjans, E. J. Connors, J. Corrigan, M. Curry, M. K. Harper *et al.*, "12-spin-qubit arrays fabricated on a 300 mm semiconductor manufacturing line," *arXiv preprint arXiv:2410.16583*, 2024.

[185] A. J. Weinstein, M. D. Reed, A. M. Jones, R. W. Andrews, D. Barnes, J. Z. Blumoff, L. E. Euliss, K. Eng, B. H. Fong, S. D. Ha *et al.*, "Universal logic with encoded spin qubits in silicon," *Nature*, vol. 615, no. 7954, pp. 817–822, 2023.